An Efficient Method for Computing Excited State Properties of Extended Molecular Aggregates based on an *Ab-Initio* exciton model

DISSERTATION

Presented in Partial Fulfillment of the Requirements for

the Degree Doctor of Philosophy in the Graduate

School of The Ohio State University

By

Adrian F. Morrison, B.A.

Graduate Program In Chemistry

The Ohio State University

2017

Dissertation Committee:

John M. Herbert, Advisor

Sherwin J. Singer

Terry Gustafson

Heather Allen

Abstract

In this work, we outline the development, testing, and application of a novel electronic structure method for computing the properties of excited states of molecular aggregates. The method is an *ab-inito* realization of the molecular exciton model, proposed a long time ago by Frenkel and Davydov to describe excited states of molecular crystals, and is called the Ab-Initio Frenkel Davydov Exciton Model (AIFDEM). The AIFDEM ansätz follows the traditional exciton model by expanding the supersystem excited state wavefunction as a linear combination of excitations that are localized on the component molecules. Our method is a truly *ab-inito* implementation of this model as the requisite fragment excited states and the exciton Hamiltonian matrix are computed rigorously, including exact Coulomb and Hartree-Fock exchange interactions, without any neglect of overlap, nearest neighbor, or other common approximations. We have tested this method and found that it can reproduce excitation energies of water clusters, DNA bases, and organic chromophores within 0.1 eV. A charge embedding scheme is able to reduce the scaling of this method to only quadratic with the number of fragments and provides near perfect parallel performance without reducing the accuracy, significantly outperforming traditional approaches. The method was utilized to investigate the excitation energy transfer dynamics of a napthalene-diimide nanotube where it was found that model

systems beyond the scope of traditional methods are necessary for a fully detailed mechanistic picture, including the role of quantum coherence. Analytic derivatives of the AIFDEM Hamiltonian are derived and implemented and these provide access to non-adiabatic couplings as well as Holstein and Peierls electron-phonon coupling constants. This is applied to the challenging electronic structure of the singlet exciton fission process to identify vibrational modes key to the mechanism. Dynamics simulations, using parameters computed via the AIFDEM, suggest that singlet fission in crystalline tetracene is driven by vibronic coherence despite unfavorable electronic energetics. The AIFDEM approach is shown to be a promising method for excited states due to its excellent parallel scalability, unambiguous yet analytic description of the wavefunction, and ability to treat challenging electronic structure.

Dedicated to Linda Richardson and Jerry Morrison, my parents, whose contributions have been incalculable.

Acknowledgments

I must first acknowledge Professor Dale Brugh at Ohio Wesleyan University for originally introducing me to quantum chemistry and computational science as well as for teaching me approximately half of the skills that have been useful in my graduate career. Then I have to thank The Ohio State University, and specifically the Ohio Supercomputer center, for providing me with an embarrassment of riches in resources and support that enabled me to pursue my education and research. I must thank the members of the Herbert group, Ryan Richard, Ka Un Lao, Marc Coons, and the rest for camaraderie, assistance, insightful discussions, and enjoyable experiences. There is a small army of outstanding people that primarily went to Ohio Wesleyan and are living in Columbus and the surrounding areas that must thank profusley for their constant support and for making my years here unforgettable. Finally, I have to gratefully and humbly acknowledge my advisor John Herbert. I was inspired by John's introduction to quantum mechanics lectures to join his research group and pursue a subject that was unexpected and of which I had little prior experience. His support, guidance, passion, and friendship was, at times unconventional, but always unwavering and invaluable and he is the main reason that this document exists.

Vita

1990	Born, New York, New York
2004-2006	Northern Valley Regional High School
2006-2008	Paul Lawrence Dunbar High School
2008-2012	B.A. Chemistry, Ohio Wesleyan University
2012–2015	Graduate Teaching Associate, The Ohio State University
2015–2017	Graduate Research Associate, The Ohio State University

Publications

(5) A. F. Morrison and J. M. Herbert. **Analytic derivative couplings and first-principles exciton/phonon coupling constants for an *ab initio* Frenkel-Davydov exciton model: Theory, implementation, and application to compute triplet exciton mobility parameters for crystalline tetracene.** *J. Chem. Phys.,* **146**, 224110 (2017).

(4) A. F. Morrison and J. M. Herbert. **Evidence for singlet fission driven by vibronic coherence in crystalline tetracene.** *J. Phys. Chem. Lett.,* **8**, 1442 (2017).

(3) J. M. Herbert, X. Zhang, A. F. Morrison, and J. Liu. **Beyond time-depenent density functional theory using only single excitations: Methods for computational studies of excited states in complex systems.** *Acc. Chem. Res.,* **49**, 931, (2016).

(2) A. F. Morrison and J. M. Herbert. **Low-scaling quantum chemistry approach to excited-state properties via an *ab initio* exciton model: Application to excitation energy transfer in a self- assembled nanotube.** *J. Phys. Chem. Lett.,* **6**, 4390 (2015).

(1) A. F. Morrison, Z-Q. You, and J. M. Herbert. ***Ab Initio* implementation of the Frenkel-Davydov exciton model: A naturally parallelizable approach to computing collective excitations in molecular aggregates.** *J. Chem. Theory. Compute,* **80**, 5366 (2014).

Fields of Study

Major Field: Chemistry
Theoretical Physical Chemistry

Table of Contents

List of Figures

List of Tables

CHAPTER 1

Introduction

1.1 Motivation

Breakthrough innovations in energy storage and conversion technologies that will be required for clean abundant energy for generations to come can be facilitated to a significant degree by quantum chemical simulations. Indeed, quantum chemistry has already become an indispensable tool in elucidating insights into chemical phenomenon, predicting properties of new materials, and complementing experimental results. The remarkable increases in the availability of computational power over the past thirty years has opened the door to previously inaccessible results from quantum chemical calculations however, the challenge remains to design algorithms that can take full advantage of the power of rapidly evolving computer architectures. In this work, a new quantum chemical method for simulating properties and dynamics of electronic excited states, that is designed with modern parallel computer architectures in mind, is introduced and demonstrated. This method is applied to several relevant energy transfer problems that had previously been impractical for traditional approaches.

1.2 Fundamentals

1.2.1 The Schrödinger Equation

The motion of nuclei and electrons in molecules is described by the time dependent Schrödinger Equation (TDSE), which, in Hartree atomic units, is written as,

$$i\frac{\partial \mathbf{\Psi}(\mathbf{r},\mathbf{R},t)}{\partial t} = \hat{H}\mathbf{\Psi}(\mathbf{r},\mathbf{R},t) \tag{1.1}$$

where $\hat{H}$ is the Hamiltonian operator describing the system and $\mathbf{\Psi}$ is the time-dependent wavefunction, depending on nuclear, $\mathbf{R}$, and electronic, $\mathbf{r}$, coordinates. When the Hamiltonian is time independent, or can be approximated as such, the solution to Eq. 1.1 can be separated into a time-dependent and time-independent part and written as,

$$\mathbf{\Psi}(\mathbf{r},\mathbf{R},t) = \sum_I C_I e^{-iE_I t}\mathbf{\Phi}_I(\mathbf{R},\mathbf{r}). \tag{1.2}$$

Here, C_I are the coefficients of $\mathbf{\Psi}(\mathbf{r},\mathbf{R},t)$ in the basis of the eigenfunctions of the Hamiltonian, $\mathbf{\Phi}_I(\mathbf{r},\mathbf{R})$, and their corresponding eigenvalues, E_I such that,

$$\hat{H}\mathbf{\Phi}_I(\mathbf{r},\mathbf{R}) = E_I\mathbf{\Phi}_I(\mathbf{r},\mathbf{R}). \tag{1.3}$$

Noting that Eq. 1.1 is still central, much of the task of quantum chemistry is to solve the eigenvalue problem in Eq. 1.3. It is remarkable that chemical properties can be teased out of such a straightforward equation and it is equally challenging and captivating to know that analytic solutions do not exist for all but the most simple model systems. It is the enterprise of quantum chemists to make Eq. 1.3 useful by finding physically valid and computationally tractable approximate solutions.

1.2.2 The Born Oppenheimer Approximation

The Hamiltonian operator, $\hat{H}$ for a molecular system of N_{nuc} nuclei and N_e electrons can be written, again using Hartree atomic units, as,

$$\begin{aligned}\hat{H} = -\frac{1}{2}\sum_i \hat{\nabla}_i^2 - \sum_i \sum_A \frac{Z_A}{|\mathbf{r}_i - \mathbf{R}_A|} + \frac{1}{2}\sum_i \sum_j \frac{1}{|\mathbf{r}_i - \mathbf{r}_j|} \\ - \sum_A \frac{1}{2M_A}\hat{\nabla}_A^2 + \frac{1}{2}\sum_A \sum_B \frac{Z_A Z_B}{|\mathbf{R}_A - \mathbf{R}_B|}.\end{aligned} \tag{1.4}$$

Here, i, j and A, B index electrons and nuclei, respectively, and Z_A indicates the charge of the Ath nucleus while M_A indicates its mass. The Hamiltonian as written depends on $3 \times N_e + 3 \times N_{nuc}$ coupled degrees of freedom however, one may appeal to the separation of nuclear and electronic energy scales and write its solution as a sum of direct products (the index of the molecular quantum state is suppressed in what follows),

$$\mathbf{\Phi}(\mathbf{r}, \mathbf{R}) = \sum_k \Psi_k(\mathbf{r}; \mathbf{R})\chi_k(\mathbf{R}). \tag{1.5}$$

Here, $\chi_k(\mathbf{R})$ is a nuclear function and $\Psi_k(\mathbf{r}; \mathbf{R})$ is an electronic function, depending parametrically on $\mathbf{R}$, which is solution to the eigenvalue problem,

$$\hat{H}_e \Psi_k(\mathbf{r}; \mathbf{R}) = \mathcal{E}_k(\mathbf{R})\Psi_k(\mathbf{r}; \mathbf{R}). \tag{1.6}$$

We have introduced an electronic partition of the Hamiltonian from Eq. 1.4,

$$\hat{H}_e = -\frac{1}{2}\sum_i \hat{\nabla}_i^2 - \sum_i \sum_A \frac{Z_A}{|\mathbf{r}_i - \mathbf{R}_A|} + \frac{1}{2}\sum_i \sum_j \frac{1}{|\mathbf{r}_i - \mathbf{r}_j|}, \tag{1.7}$$

with eigenvalues, $\mathcal{E}_k(\mathbf{R})$ that represent the energy of the kth electronic state at a given set of nuclear coordinates. The nuclear part of the Hamiltonian is then,

$$\begin{aligned}\hat{H}_{nuc} &= -\sum_A \frac{1}{2M_A}\hat{\nabla}_A^2 + \frac{1}{2}\sum_A \sum_B \frac{Z_A Z_B}{|\mathbf{R}_A - \mathbf{R}_B|} \\ &= \hat{T}_{nuc} + V_{nuc}(\mathbf{R}).\end{aligned} \tag{1.8}$$

We may then rewrite Eq. 1.3 as,

$$\left(\hat{H}_e + \hat{T}_{nuc} + V_{nuc}(\mathbf{R})\right) \sum_k \Psi_k(\mathbf{r};\mathbf{R})\chi_k(\mathbf{R}) = E \sum_k \Psi_k(\mathbf{r};\mathbf{R})\chi_k(\mathbf{R}). \tag{1.9}$$

Now, left multiplying Eq. 1.8 by $\Psi_l^*(\mathbf{r};\mathbf{R})$, integrating over electronic coordinates, and rearranging, yields,

$$\left(\hat{T}_{nuc} + \mathcal{E}_l(\mathbf{R}) + V_{nuc}(\mathbf{R})\right) \chi_l(\mathbf{R}) + \sum_k \left(\boldsymbol{\gamma}_{lk}^{(\mathbf{1})}(\mathbf{R}) + d_{lk}^{(2)}(\mathbf{R})\right) \chi_k(\mathbf{R}) = E\chi_l(\mathbf{R}). \tag{1.10}$$

Here we have defined,

$$\boldsymbol{\gamma}_{lk}^{(\mathbf{1})}(\mathbf{R}) = -\sum_A \frac{1}{M_A} \int d\mathbf{r} \;\; \Psi_l^*(\mathbf{r};\mathbf{R}) \frac{\partial}{\partial \mathbf{R}_A} \Psi_k(\mathbf{r};\mathbf{R}) \cdot \hat{\bigtriangledown}_A \tag{1.11}$$

and

$$d_{lk}^{(2)}(\mathbf{R}) = -\sum_A \frac{1}{2M_A} \int d\mathbf{r} \;\; \Psi_l^*(\mathbf{r};\mathbf{R}) \frac{\partial^2}{\partial \mathbf{R}_A^2} \Psi_k(\mathbf{r};\mathbf{R}), \tag{1.12}$$

where the integrals in Eq. 1.11 and Eq. 1.12 are known as the first and second order derivative couplings, respectively. These quantities codify the degree to which the nuclear and electronic degrees of freedom, which we have chosen to separate, are in actuality coupled. When these quantities are negligible, Eq. 1.8 is reduced to a simple eigenvalue problem for the vibrational motion of the nuclei and its solution, Eq. 1.5 contains only a single term. Physically, this amounts to a description of nuclei that move on a continuous potential energy surface due to Coulombic interaction with electrons that instantaneously rearrange at every nuclear configuration. In this situation the electronic and nuclear degrees of freedom are adiabatically separated, that is they do not exchange energy and the motion of one does induce energetic transitions in the other. The basis of Born-Oppenheimer approximation is treat

the molecular problem as if the derivative couplings are negligible, enforcing these conditions, and allowing us to solve the electronic and nuclear parts of Eq. 1.10 separately.

It can be shown that the derivative couplings can be written in the so called Hellman-Feynman form, using Bra-Ket notation and suppressing dependance on $\mathbf{R}$,

$$\langle \Psi_k | \hat{\nabla}_{\mathbf{R}} | \Psi_l \rangle_{\mathbf{r}} = \frac{\langle \Psi_k | \hat{\nabla}_{\mathbf{R}} \hat{H}_e | \Psi_l \rangle_{\mathbf{r}}}{\mathcal{E}_l - \mathcal{E}_k}. \tag{1.13}$$

Eq. 1.13 indicates that in regions of nuclear coordinate space where the electronic Hamiltonian rapidly changes or where the energies of two different electronic states approach degeneracy, the derivative couplings may be large and the Born-Oppenheimer approximation, and the physical picture it entails, is no longer valid. This is indeed the case for radiationless transitions in photochemistry, another relevant example is explored in this work in Ch. 5.

1.3 Electronic Structure

Now that we are equipped with the fundamental approximations we are ready to approach the heart of quantum chemistry, that is the adiabatic electronic structure problem; finding a solution for Eq. 1.6. Note, that time-dependent and non-adiabatic aspects of quantum chemistry are entirely valid areas of fruitful research, indeed the focus Ch. 3 in this work is in developing an approach for evaluating derivative couplings (Eq. 1.13). It remains that solutions to Eq. 1.6 are the foundation of quantum chemical methods and they can provide access, via operators or energy derivatives, to many chemical properties of interest.

Despite the approximations already introduced, and its apparent simplicity, Eq. 1.6 remains a remarkably challenging problem. The final term on the RHS of Eq. 1.7 describes the Coulomb interactions between electrons and ensures that no analytic solution exists when there is more than one in the system. Therefore, electronic structure methods must solve this problem numerically, typically by expanding the solution in a finite basis set. For molecular electronic structure theory the basis set of choice is gaussian type orbitals (GTOs) centered on atoms, due to the efficient form of their integrals. The workhorse GTO based molecular electronic structure methods generally follow two paths: wavefunction based theories, starting from the Hartree-Fock method; and density functional theory based on the Kohn-Sham theorem. A brief outline of these methods follows

1.3.1 Ground State Methods

Hartree-Fock Theory

The Hartree-Fock (HF) method was essentially the first electronic structure method that was useful, however it remains relevant to this day as the foundation of wavefunction theory and the technologies developed for its evaluation are useful in many aspects of electronic structure. The HF ansätz approximates Ψ_k is as a single determinant of orbitals, which ensures Fermionic antisymmetry,

$$\Psi_{HF} = |\phi_1\phi_2...\phi_{N-1}\phi_N\rangle. \tag{1.14}$$

Here, $|...\rangle$ represents a Slater Determinant and ϕ_i represents the ith molecular orbital (MO). These orbitals are expanded in an atomic orbital (AO) basis of N GTOs as,

$$\phi_i = \sum_{\mu} g_\mu C_{\mu i}, \tag{1.15}$$

where g_μ is a GTO AO basis function, indexed by lowercase Greek letters, and $C_{\mu i}$ is the corresponding expansion coefficient for the MO. Note that, for our purposes, we can limit ourselves to the use of real valued basis functions, resulting in a real valued wavefunction. The electron-electron repulsion in HF theory is approximated as a mean field potential such that the MOs describe single particles moving in the averaged coulomb potential of all the other electrons and the fixed nuclei. The HF energy expression is,

$$E_{HF} = \sum_i \langle \phi_i | \hat{h}(1) | \phi_i \rangle + \frac{1}{2} \sum_{ij} \langle ij || ij \rangle, \tag{1.16}$$

where,

$$\hat{h}(1) = -\frac{1}{2} \sum_i \hat{\nabla}_i^2 - \sum_i \sum_A \frac{Z_A}{|\mathbf{r}_i - \mathbf{R}_A|}, \tag{1.17}$$

is known as the core hamiltonian and,

$$\begin{aligned} \langle ij || ij \rangle &= \langle ii | jj \rangle - \langle ij | ij \rangle \\ &= \int \; d\mathbf{r}_1 \; d\mathbf{r}_2 \; \phi_i(\mathbf{r}_1) \phi_j(\mathbf{r}_2) \frac{1}{|\mathbf{r}_1 - \mathbf{r}_2|} \phi_i(\mathbf{r}_1) \phi_j(\mathbf{r}_2) \\ &- \int \; d\mathbf{r}_1 \; d\mathbf{r}_2 \; \phi_i(\mathbf{r}_1) \phi_j(\mathbf{r}_2) \frac{1}{|\mathbf{r}_1 - \mathbf{r}_2|} - \phi_i(\mathbf{r}_2) \phi_j(\mathbf{r}_1), \end{aligned} \tag{1.18}$$

are electron repulsion integrals. These integrals are antisymmetrized due to the determinantal structure of the wavefunction and the second term on the RHS of Eq. 1.18 describes the Pauli exchange interaction.

The wavefunction in Eq. 1.14 is optimized variationally by minimizing E_{HF} with respect to the MO coefficients. This requires the solution of a set of linear equations,

$$\mathbf{FC} = \epsilon \mathbf{SC}, \tag{1.19}$$

where $\mathbf{C}$ is the matrix of MO coefficients, $\mathbf{S}$ is the overlap matrix of the GTOs, $S_{\mu\nu} = \langle g_\mu | g_\nu \rangle$, and ϵ are single particle energies. The Fock operator, $\mathbf{F}$, for a closed shell molecule has elements,

$$F_{\mu\nu} = \langle g_\mu | \hat{h}(1) | g_\nu \rangle + \sum_{i}^{N_e/2} \sum_{\lambda\sigma} C_{\lambda i} C_{\sigma i} \left[2\langle \mu\lambda | \nu\sigma \rangle - \langle \mu\lambda | \sigma\nu \rangle \right]. \tag{1.20}$$

Eq. 1.19 is solved by diagonalizing $\mathbf{F}$, (interestingly analogous to solving the actual time independent Schrödinger Equation in some basis) yielding a new set of MOs that are used to update the Fock operator in Eq. 1.20. This procedure is repeated until self-consistency is achieved. The HF methods scales formally as the fourth power of system size, due to integral evaluation, however, screening techniques can shift the bottleneck to the diagonalization operation which scales cubically.

Post-Hartree-Fock Theory

HF theory offers a first approximation to the solution of the Schrödinger equation, the difference between the energy of the HF solution and the true energy of the system is known as the correlation energy,

$$E_{correlation} = \mathcal{E} - E_{HF}. \tag{1.21}$$

It represents the energy component due to dynamical response of the electrons that is not described by a mean field potential or single determinant wavefunction. HF theory

provides a jumping off point for finding the exact solution of the Schrödinger equation to arbitrary precision in what is called configuration interaction (CI). The solution of Eq. 1.19 yields a set of N MOs, the N_e of which that have the lowest single particle energies are considered to be 'occupied' by the electrons of the system and are included in the HF mean field potential. The remaining $N - N_e$ orbitals are called 'virtual' and they roughly approximate ionized states. We can form new sets of determinants by replacing one or more occupied orbital in the reference HF determinant with one or more virtual orbitals and this set of all replacement determinants forms a basis in which the exact wavefunction may be expanded,

$$\begin{aligned}\Psi = |\Psi_{HF}\rangle + \sum_{ia} t_{ia}|\phi_1\phi_2\cdots\phi_{i-1}\phi_a...\phi_{N_e-1}\phi_{Ne}\rangle \\ + \frac{1}{4}\sum_{ijab} t_{ijab}|\phi_1\phi_2\cdots\phi_{i-1}\phi_a\cdots\phi_{j-1}\phi_b\cdots\phi_{N_e-1}\phi_{Ne}\rangle + \cdots ,\end{aligned} \tag{1.22}$$

where t are the CI coefficients and the full expansion is made to determinants with N_e substitutions. A full CI expansion is exact to the degree of completeness of the AO basis set, $\Psi_{FCI} = \Psi$ if basis set fully spans the electronic space. This procedure is simple conceptually but unfortunately intractable computationally as the cost scales exponentially with the size of the basis. The majority of electronic structure methods that aim for accuracy beyond HF theory, post HF methods, begin with the HF determinant and then seek to approximate the full CI problem in a more affordable way.

One of the most popular post HF methods is based on a perturbation expansion of the full CI wavefunction. The Moler-Plesset partitioning of the Hamiltonian is,

$$\hat{H}_{MP} = \hat{h}(1) + \hat{v}_{HF} + \hat{W}, \tag{1.23}$$

where $\hat{v}_{HF}$ represents the HF mean field potential and $\hat{W}$ is the Moler-Plesset fluctuation potential expressed as,

$$\hat{W} = \frac{1}{2}\sum_{ij}\frac{1}{|\mathbf{r}_i - \mathbf{r}_j|} - \hat{v}_{HF}. \tag{1.24}$$

This partitioning ensures that the HF determinant is the zeroth order solution in a perturbation expansion and it can be solved to arbitrary order. A second order truncation is commonplace which is known as MP2 and this method scales as the fifth power of the system size.

A second important approximate approach to the solution of the full CI problem is known as coupled-cluster (CC) theory and based on an exponential ansätz for the wavefunction,

$$\Psi_{CC} = e^{\hat{T}_1 + \hat{T}_2 + \cdots}|\Psi_{HF}\rangle. \tag{1.25}$$

The excitation operators, $\hat{T}_i$ introduce i occupied $\rightarrow$ virtual substitutions in the HF determinant, for instance,

$$\hat{T}_1 = \sum_{ia} t_{ia}\hat{\tau}_{ia}, \tag{1.26}$$

where $\hat{\tau}_{ia}$ generates the excitation and t_{ia} is the cluster amplitude (note that these are not necessarily the same as the CI amplitudes introduced above). The CC wavefunction is found by left projecting on the set of excited determinants,

$$\langle\Psi_{ij\cdots}^{ab\cdots}|e^{-(\hat{T}_1+\hat{T}_2+\cdots)}\hat{H}_e e^{\hat{T}_1+\hat{T}_2+\cdots}|\Psi_{HF}\rangle = 0. \tag{1.27}$$

To be practical excitation level in the exponential must be truncated. The generally accepted 'gold standard' electronic structure method for accuracy is coupled cluster

truncated to single and double excitations with triple excitations treated perturbatively (CCSD(t)), which scales as the 7th power of system size.

Density Functional Theory

While wavefunction based methods are important and widely used, the workhorse of practical electronic structure theory in the past twenty years has been density functional theory (DFT). Rather than $\Psi(\mathbf{r})$, DFT focuses on the single particle electron density, $\rho(\mathbf{r})$ as its central quantity of interest,

$$\rho(\mathbf{r}) = \int d(\mathbf{r}_1, \mathbf{r}_2 \ldots \mathbf{r}_{N_e-1}) \;\; \Psi^*(\mathbf{r}_1, \mathbf{r}_2 \ldots \mathbf{r}_{N_e-1}, \mathbf{r}_{N_e}) \Psi(\mathbf{r}_1, \mathbf{r}_2 \ldots \mathbf{r}_{N_e-1}, \mathbf{r}_{N_e}). \quad (1.28)$$

Thanks to the pioneering work of Hohenberg and Kohn whose eponymous theorem tells us that the electronic energy of any system of electrons moving in an external potential is a unique and exact functional of its electron density. That functional can be written as,

$$E[\rho(\mathbf{r})] = T[\rho(\mathbf{r})] - \sum_A \int d\mathbf{r} \frac{\rho(\mathbf{r}) Z_A}{|\mathbf{r} - \mathbf{R}_A|} + \int d\mathbf{r}_1 d\mathbf{r}_2 \frac{\rho(\mathbf{r}) \rho(\mathbf{r}')}{|\mathbf{r} - \mathbf{r}'|} + E_{XC}[\rho(\mathbf{r})]. \quad (1.29)$$

Here, $T[\rho(\mathbf{r})]$ is the kinetic energy functional of the electron density and $E_{XC}[\rho(\mathbf{r})]$ is the so called exchange-correlation functional which contains the correlation and exchange energy components that are not captured by the classical coulomb term. If the kinetic and exchange-correlation functionals are exact, then the minimization of the energy with respect to $\rho(\mathbf{r})$ is equivalent to solving Eq. 1.6 for the ground state of the system. In principal, this is appealing because the dimensionality of the problem is reduced from $3 \times N_e$, the electronic coordinates, to simply 3, the arguments of the

density. Unfortunately, the exact form of $T[\rho(\mathbf{r})]$ and $E_{XC}[\rho(\mathbf{r})]$ are not known for general systems.

In practice, DFT calculations are commonly performed in a way that is a great deal like HF calculations. Kohn and Sham derived another important theorem in the liturgy of DFT that introduces a set of auxiliary single particle MOs, of the same form as those in Eq. 1.14, that themselves are not truly meaningful but together form the true density. This simplifies the expression for $T[\rho(\mathbf{r})]$ and the DFT energy expression reduces to essentially look like Eq. 1.16 with an extra term for the exchange correlation functional,

$$E_{KS} = \sum_i \langle \phi_i | \hat{h}(1) | \phi_i \rangle + \frac{1}{2} \sum_{ij} \left[\langle ij|ij \rangle - c_{hf} \langle ii|jj \rangle \right] + E_{XC}[\rho(\mathbf{r})], \tag{1.30}$$

where c_{hf} is defined by the exchange-correlation functional and allows some portion of HF-derived exchange interactions to enter the DFT energy. This expression is minimized according to a variational principle resulting in a calculation that proceeds in much the same way as the HF method with similar scaling characteristics. It should be noted that the exact form of the exchange correlation functional remains unknown, functionals are continuously being developed and they are the key ingredient for this method's accuracy; certain functionals perform well for certain systems and some don't work well at all.

1.3.2 Excited State Methods

We have focused thus far on the ground state electronic structure problem however nearly as much effort has has been made on methods designed to find the higher lying

eigenstates of $\hat{H}_e$. The excited state problem is slightly more complicated for several reasons: electron correlation tends to be more significant; states are more spatially diffuse so higher quality AO basis sets are required; but the main difficulty is that there is no variational principle to rely on in the search for excited state solutions. The ground state methods described earlier, as well as others, often have excited state counterparts. Again, various operators and gradients allow access to a variety of chemical properties. We will briefly outline several methods here.

Configuration Interaction With Single Substitutions

The solutions of the full CI problem, with a complete basis set, are exact for the excited states as well as the ground state and they are equally computationally intractable for real systems. A particular truncated version the full CI problem that specifically targets excited states expands the wavefunction in a basis of HF determinants where a single occupied orbital is substituted with a virtual orbital. As these singly substituted determinants are representative of ionized states a it is expected that a linear combination of them should qualitatively describe excited states. Furthermore, according to Brillouin's theorem, these excited states do not mix with the HF reference determinant therefore their energies may directly be interpreted as excitation energies. The configuration interaction with single substitutions (CIS) wavefunction for the Ith excited state is written as,

$$\Psi^I_{CIS} = \sum_{ia} t^I_{ia} |\phi_1 \phi_2 \dots \phi_{i-1} \phi_a \dots \phi_{N_e-1} \phi_{N_e}\rangle, \tag{1.31}$$

where t_{ia}^{I} are the CIS amplitudes for the Ith excited state, note that these are again distinct from the CI and CC amplitudes introduced earlier. The amplitudes are found by diagonalizing $\hat{H}_e$ expressed in this basis, the elements of which are,

$$\begin{aligned}\langle\phi_1\phi_2\ldots\phi_{i-1}\phi_a\ldots\phi_{N_e}|\hat{H}_e|\phi_1\phi_2\ldots\phi_{j-1}\phi_b\ldots\phi_{N_e}\rangle &= H_{ia,jb} \\ &= (\epsilon_a-\epsilon_i)\delta_{ij}\delta_{ab}+\langle aj||ib\rangle.\end{aligned} \tag{1.32}$$

The size of this matrix grows approximately as the 4th power of system size therefore it is typically diagonalized iteratively using Davidson's procedure. This requires matrix-vector products of the CIS Hamiltonian with trial amplitude vectors to form the so called sigma vectors,

$$\sigma_{ia}=\sum_{jb}H_{ia,jb}t_{jb}=\sum_{jb}\left[(\epsilon_a-\epsilon_i)\delta_{ij}\delta_{ab}+\langle aj||ib\rangle\right]t_{jb}. \tag{1.33}$$

The bottleneck step in this procedure is the formation of the two-electron contribution to the sigma vectors which can be written in terms of a Fock-like matrix, $\tilde{\mathbf{F}}$,

$$\tilde{F}_{ia}=\sum_{\mu\nu}C_{\mu a}C_{\nu i}\sum_{\lambda\sigma}\langle\mu\lambda||\nu\sigma\rangle\tilde{P}_{\lambda\sigma}, \tag{1.34}$$

where,

$$\tilde{P}_{\lambda\sigma}=\sum_{jb}C_{\lambda j}t_{jb}C_{\sigma b}. \tag{1.35}$$

The contraction in Eq. 1.35 scales as the fourth power of system size making CIS roughly equivalent to HF theory in terms of cost. Like HF theory, CIS is generally considered to be qualitative at best and is lacking the components of the excitation energy due to correlation, also like HF theory this can be added in perturbatively. Nevertheless, CIS remains a useful basic treatment of the excited state electronic structure problem.

Linear Response Time Dependent Density Functional Theory

Linear response time-dependent density functional theory, commonly and confusingly known as time-dependent density functional theory (TDDFT), is the DFT approach to computing excited states and, like its ground state counterpart, the electron density is the central quantity. Runge and Gross have shown that the time dependent wavefunction can be completely determined by the time dependent density, $\rho(\mathbf{r}, t)$. It follows then that the response of the density to an applied electromagnetic field presents a means to access many electron excited states. While a detailed derivation is beyond the scope of this document, the general idea is to expand the linear response of the Kohn-Sham density matrix in terms of occupied $\rightarrow$ virtual excitations and de-excitations of Kohn-Sham orbitals. The density response can then be can be cast as a matrix equation,

$$\begin{pmatrix} \mathbf{A} & \mathbf{B} \\ \mathbf{B}^* & \mathbf{A}^* \end{pmatrix} \begin{pmatrix} \mathbf{X} \\ \mathbf{Y} \end{pmatrix} = \omega \begin{pmatrix} \mathbf{1} & \mathbf{0} \\ \mathbf{0} & \mathbf{-1} \end{pmatrix} \begin{pmatrix} \mathbf{X} \\ \mathbf{Y} \end{pmatrix}. \tag{1.36}$$

Here,

$$A_{ia,jb} = (\epsilon_a - \epsilon_i)\delta_{ij}\delta_{ab} + \langle aj|ib\rangle - c_{HF}\langle aj|bi\rangle + \langle aj|\hat{f}_{XC}|ib\rangle. \tag{1.37}$$

Note that this expression is quite similar to that of CIS Hamiltonian matrix elements with the added quantity,

$$\langle aj|\hat{f}_{XC}|ib\rangle = \int d\mathbf{r}d\mathbf{r}' \;\; \phi_a(\mathbf{r})\phi_j(\mathbf{r})\frac{\partial E_{xc}}{\partial \mathbf{r}\partial \mathbf{r}'}\phi_b(\mathbf{r}')\phi_i(\mathbf{r}'). \tag{1.38}$$

This term is known as the exchange correlation kernel and utilizes the adiabatic approximation (a different adiabatic approximation than introduced previously) which

neglects the past-time dependance of the exchange-correlation part of the response by utilizing ground state exchange-correlation functional derivatives. The elements of the matrix **B** are,

$$B_{ia,jb} = \langle ij|ab\rangle - c_{hf}\langle ia|jb\rangle + \langle ij|\hat{f}_{xc}|ab\rangle. \tag{1.39}$$

Finally, ω represents the excitation energies while **X** and **Y** are the excitation and de-excitation amplitudes of the density response, respectively.

It is also common to employ the Tamm-Dancoff approximation (TDA) which neglects the de-excitation amplitudes reducing Eq. 1.36 to simply,

$$\mathbf{AX} = \omega\mathbf{X}. \tag{1.40}$$

This reduces the TDDFT problem to a diagonalization of the matrix, **A**, quite like the CIS problem and, analogously to the ground state, they are computed following the same general procedure with similar scaling characteristics. TDA-TDDFT suffers from the same shortcomings as its ground state counterpart, also due to inadequate and inappropriate exchange-correlation functionals. However, it remains extremely popular as TDDFT is generally considered to provide acceptable accuracy for its relatively low computational cost.

1.4 Computer architectures, fragment methods, and the future of electronic structure

The most straightforward means of increasing computer performance, increasing the clock speed at which processors execute, came to an end almost 10 years ago, foiled

by the excessive heat that was generated by switching silicon at high frequencies. Other than modest architectural improvements, enterprise level single threaded software performance has quickly approached an asymptotic limit since that point. The strategy to to increase computer performance since then has been to multiply the amount of execution hardware per processing unit; two, four, and these days dozens of general purpose processor cores, or in specialized hardware hundreds of simplified cores, work in parallel on the same silicon die. Modern workloads are executed by supercomputer clusters that are made up of thousands of such cores networked together. Software must be designed specifically to take advantage of the parallel performance of modern architectures, a task that is tricky at best and at worst fundamentally limited by the nature of the problem. The workload of parallel algorithms must be distributed to many execution units, executed concurrently, and accumulated into a final result; algorithms with temporal dependencies or intricate control flow do not conform well to this structure.

Unfortunately, quantum mechanics is formally a non-local problem, that is $\Psi(\mathbf{r})$ at any point in coordinate space depends on the potential at all of the other points. Computationally, this amounts to data elements that are strongly coupled to one another, for instance in Eq. 1.20 and Eq. 1.35 quantities that represent interactions spanning the entire electronic space are globally coupled through contractions, all of that data must be accumulated together to arrive at the final answer. While the arithmetic capabilities of modern computers are truly astounding, moving data from memory to execution units is fundamentally limited by the speed of electrons moving

through metal, ultimately any algorithm is bottlenecked by the time it takes to move data. Indeed, there is a certain irony to the fact that simulating the laws of nature is now fundamentally limited by the laws of nature.

For practical electronic structure methods screening techniques, density fitting, and rational truncation schemes have been productive means of increasing algorithm performance but in this work we pursue the conceptually appealing avenue of fragment methods. As chemists, we have for a long time approached problems by breaking them down into fragments; functional groups that maintain transferable general properties, biomolecules with an active site and a backbone, solutes and solvents. In quantum chemistry we can appeal to the concept of nearsightedness of electronic matter, described by Walter Kohn of DFT fame, where primary electronic structure is non-local but the details of the electronic correlation are short ranged. There are quite a few mainstream electronic structure methods, such as many-body expansions, multilayer methods, and embedding schemes, that start from calculations on portions of a chemical system and then use clever schemes to put them back together. Computationally, this amounts to breaking apart a globally coupled problem to one of localized data domains, which can naturally be executed in parallel, and the information content of which can then be reassembled with a low dimensional reduction. While most fragment methods tend to focus on the ground state, here we introduce one based on an old idea that is a fragment method for excited states.

CHAPTER 2

Ab Initio Implementation of the Frenkel-Davydov Exciton Model: A Naturally Parallelizable Approach to Computing Collective Excitations in Molecular Aggregates

A fragment-based method for computing vertical excitation energies of molecular clusters is introduced based on an *ab initio* implementation of a Frenkel-Davydov exciton model consisting of singly-excited monomer basis states. Our strategy is to construct and diagonalize exact Hartree-Fock Hamiltonian in such a basis. Matrix elements between non-orthogonal determinants are computed via the corresponding orbital transformation and the resulting generalized eigenvalue problem is solved to determine collective excitation energies and wave functions. The basis may be expanded to include higher-lying fragment excited states in order to account for inter-fragment polarization affects. Absolute errors relative to supersystem methods are < 0.1 eV for water clusters and ≈ 0.3 eV for conjugated organic chromophores. Preliminary tests for a nine-chromophore subunit of an organic nanotube suggest that it is possible to target the optically-bright state, even when it is a high-lying excitation, by using carefully-selected basis states. The highly parallel nature of this method provides a

foundation for further developments to treat collective excitations in large molecular assemblies.

2.1 Background

Quantum chemical calculations of excited-state properties have played an important role in numerous fields of modern chemical research, such as solar energy conversion,[4–6] nanomaterials,[7,8] and more. However, the potential of quantum chemistry as a tool that can dramatically benefit the research and development of novel materials is only beginning to be realized. The challenge for excited-state methods, as with much of quantum chemistry, is the highly nonlinear scaling of the computational cost; even the cheapest excited-state methods formally scale as $\mathcal{O}(N^4)$ with system size.[9] Systems such as conjugated polymers or the light harvesting complexes in photosynthetic proteins push the boundaries of conventional quantum chemistry, even when simplified model systems are used. Accurate computations of isolated chromophores in the gas phase are now computationally feasible but most excited state processes of interest take place in the condensed phase and their properties are often profoundly affected by the solution or solid-phase environment. Approximate wave function methods have been introduced that are capable of scaling into these regimes,[10,11] and often these are very successful but they introduce approximations that may not be appropriate in all cases. Time dependent density functional theory[12] (TDDFT) is generally regarded as the method of choice for excited-state properties in large systems, however the proper choice of exchange-correlation functional (including

significant problems with their long-range behavior in large systems[13–19]) introduces system-specific complexity that may significantly impact the success of the method.

On the computational side, it has been the case for some time that single-threaded CPU performance has essentially reached an asymptotic limit. Today, Moore's Law is realized by improvements in concurrent multithreaded performance by the continued addition of processor cores to computer systems. Modern supercomputers include of tens of thousands of CPU cores, and even an average workstation may have dozens, and these numbers are only increasing. To continue to push the boundaries of quantum chemistry research, algorithms must be designed to scale efficiently across these massively parallel, peta-scale architectures. The simplest way to do so is to exploit the "embarrassing parallelizability" of an algorithm whose effort can be sub-divided into a large number of completely independent processes.

Here, we introduce a novel method for computing excitation energies for systems of weakly interacting fragments such as liquids or molecular aggregates. The method is based on the molecular exciton model that was first introduced by Frenkel in 1931,[20] who described the excited states of solids as superpositions of excitation waves. This idea was further expanded by Davydov in 1964,[21] who wrote the Hamiltonian for a molecular crystal as

$$\hat{H} = \sum_n \hat{H}_n + \frac{1}{2} \sum_{m<n} \hat{V}_{mn} \ , \tag{2.1}$$

where $\hat{H}_n$ is the Hamiltonian operator for the molecule located at lattice site n, and $\hat{V}_{mn}$ is the coupling between sites. Energy is variationally minimized and solutions to

the requisite secular equation have the form

$$\Psi_I = \sum_n \sum_i k_n^i \phi_n^i \prod_{m \neq n} \phi_m \ . \tag{2.2}$$

Here, Ψ_I is the Ith excited state of the supersystem and ϕ_n^i is the ith singly-excited eigenstate of the nth monomer unit, whereas ϕ_m is the wave function for monomer m in its ground state.

It is important to make clear the physics that distinguishes excitonic behavior, in no small part because "exciton" is a confusing term in the literature. We take "exciton" to mean an excited state of a collection of chromophores that is delocalized across one or more of them, but which can nevertheless be represented as a linear combination of excited states that are spatially localized on particular subunits. This representation is the fundamental *ansatz* that we make in putting forth an "exciton model". Note that cases where the excitation *is* actually localized on one subunit emerge naturally as a special case. Molecular (as opposed to solid-state) exciton theory has been applied in the past to explain the spectroscopic behavior of oligomeric systems of interest in biology and photosynthesis,[22] and more recently in characterizing the aggregation of light harvesting complexes.[23]

Historically, the coupling matrix elements between direct-product basis states were computed as Coulomb integrals over transition densities,[24] or even more simply within a dipole approximation. Some improvements beyond this have been made, as summarized in Ref. 25, but electronic overlap and exchange effects are still typically neglected. More recently, new approaches have been developed that construct and diagonalize an effective Hamiltonian projected onto an excitonic basis,[26,27] with the

aim of reducing computational cost as compared to construction and diagonalization of the full Hamiltonian for the aggregate.

As an alternative, we present a fully *ab initio* implementation of the original Frenkel-Davydov exciton model. The full Hartree-Fock Hamiltonian is diagonalized in a basis of singly-excited fragments, as in Eq. (2.2), so that the Coulomb and exchange interactions from Hartree-Fock theory are treated exactly, as is the non-trivial overlap of the fragment wave functions. The basis states are constructed by forming direct products of configuration state functions computed from N_{frgm} independent fragment self-consistent field (SCF) calculations and results in a basis whose dimension is at least $N_{\text{frgm}} + 1$, including the direct-product ground state. Fragment states used to construct the basis are adiabatic in the sense that they are determined in the absence of inter-fragment interactions. The basis space can be expanded to include higher-lying fragment excitations, which increases the flexibility of the direct-product *ansatz*, or to include charge-transfer basis states to explore the mixing of neutral and charge-transfer excitons. To the best of our knowledge, our approach is the first to include exact Hartree-Fock exchange interactions in the excitonic coupling. These prove to be crucial for accuracy at short intermolecular distances.

In its current implementation, the aggregate CPU time required for our method scales more steeply, as a function of system size, than does the CPU time required for traditional supersystem methods such as configuration interaction singles (CIS). However, the overwhelming computational bottleneck in our approach is calculation of individual matrix elements of the exciton Hamiltonian, and these concurrent tasks

are embarrassingly parallelizable. As such, the required wall time should be reduced in nearly direct proportion to the number of available CPU cores. We provide examples of several exciton calculations for relevant systems of interest where this combination of parallelism and *a priori* simplification of the problem results based on chemical intuition results in significantly reduced wall times and memory requirements, relative to a traditional supersystem calculation, while maintaining accuracy of $\lesssim 0.3$ eV with respect to supersystem CIS results.

2.2 Theory

2.2.1 Direct-Product Configuration State Function Basis

The strategy of our *ab initio* fragment exciton approach is to construct and diagonalize the Hamiltonian in an excitonic basis made up of direct products of fragment configuration state functions (CSFs). The fragment CSFs are computed from ground and excited-state SCF calculations for the independent fragments. CSFs on different fragments are generally non-orthogonal, and may be comprised of multiple determinants. The notation we use is as follows: for fragment M, Ψ_M indicates a CSF, Φ_M indicates a Slater determinant, ϕ_p^M is a molecular orbital (MO), and n_M indicates the total number of occupied orbitals, including both α and β spin states. The total number of occupied orbitals in the system of N_{frgm} fragments is denoted by N.

Consider a system of two chromophores, A and B, and a direct product state $|\Psi_A^* \Psi_B\rangle$ involving excitation of fragment A. The ground-state CSF for fragment B,

$$|\Psi_B\rangle = |\Phi_B\rangle = \frac{1}{\sqrt{n_B}} \left| \phi_1^B \; \phi_2^B \; \cdots \; \phi_{n_B}^B \right| \; , \tag{2.3}$$

is a single Slater determinant constructed from a set of SCF MOs. The spin-adapted CSF for the excited fragment A,

$$|\Psi_A^*\rangle = \sum_{ia} \sum_{\sigma=\alpha,\beta} C_\sigma^{ia} \, |\Phi_A^{ia}\rangle \, , \tag{2.4}$$

is a linear combination of singly-substituted determinants $|\Phi_A^{ia}\rangle$ weighted by CI coefficients C_σ^{ia} that are computed for the spin-restricted singlet or triplet state of each isolated fragment. We use restricted SCF calculations for the fragments, so the spatial orbitals and CI coefficients are identical, up to a possible sign change, for α and β spin, but we must treat both spin components explicitly in order to account for spin coupling between states. The overall excitonic basis state can then be written

$$|\Psi_A^* \Psi_B\rangle = \frac{1}{\sqrt{N}} \left| \sum_{ia\sigma} C_\sigma^{ia} \phi_a^A \left(\prod_{j \neq i}^{n_A - 1} \phi_j^A \right) \phi_1^B \phi_2^B \cdots \phi_{n_B}^B \right| \, . \tag{2.5}$$

For clarity, the notation in Eq. (2.5) only includes two fragments, A and B. More generally, basis states $|\Psi_A^* \Psi_B \Psi_C \cdots\rangle$ will simply append ground-state (MOs) $\phi_1^C \phi_2^C \cdots \phi_{n_C}^C$, etc., to the Slater determinant in Eq. (2.5). In this way, every basis state includes all of the occupied MOs for the entire system. This stands in contrast to traditional exciton theory that considers only pairwise Coulomb interactions of the excited sites and neglects the overlap of the remaining fragments. In order to include non-pairwise additivity in the exchange interactions, and therefore enforce antisymmetry in the excitonic wave functions, all MOs *must* be included. However, the fragment MOs computed from independent SCF calculations are not orthogonal therefore the excitonic basis states are not orthogonal. Therefore overlap matrices

must be computed, in addition to matrix elements of the Hamiltonian, and a generalized eigenvalue problem must be solved. These matrix elements between CSFs are

$$\langle \Psi_A^* \Psi_B | \Psi_A \Psi_B^* \rangle = \sum_{ia\sigma} \sum_{kb\tau} C_\sigma^{ia} C_\tau^{kb} \langle \Phi_A^{ia} \Phi_B | \Phi_A \Phi_B^{kb} \rangle \tag{2.6a}$$

$$\langle \Psi_A^* \Psi_B | \hat{H} | \Psi_A \Psi_B^* \rangle = \sum_{ia\sigma} \sum_{kb\tau} C_\sigma^{ia} C_\tau^{kb} \langle \Phi_A^{ia} \Phi_B | \hat{H} | \Phi_A \Phi_B^{kb} \rangle \ . \tag{2.6b}$$

In our spin-restricted implementation there are only two distinct spin terms for each pair of transitions. The sign of the coupling term is derived from the spin of the fragment: positive for singlet and negative for triplet. This, in turn, determines the spin of target state.

2.2.2 Natural Transition Orbital Representation

In order to minimize the number of terms in Eq. (2.6), we transform the fragment excited states into the natural transition orbital (NTO) basis.[28–30] The $n_M^{\text{occ}} \times n_M^{\text{virt}}$ single-particle transition density matrix, $\mathbf{T}$, couples occupied and virtual orbitals with coefficients C^{ia} from a CIS or TDDFT calculation, the latter performed within the Tamm-Dancoff approximation (TDA).[31] NTOs are computed from a singular value decomposition of $\mathbf{T}$:[29]

$$\mathbf{\Lambda} = \mathbf{OTN}^\dagger \ . \tag{2.7}$$

Here, $\mathbf{O}$ and $\mathbf{N}$ are separate unitary transformations of the canonical occupied and virtual MOs, respectively, which transform these orbitals into a set of (state-specific) paired hole and particle NTOs. This transformation reduces the dimension of the

CI expansion to no more than n_M^{occ} particle-hole excitations and the diagonal matrix $\mathbf{\Lambda}$ contains the coefficients of these excitations in the NTO basis. This results in no more than n_M terms for a single excited state and no more than $n_A n_B$ terms in Eq. (2.6). Similarly, only $n_A n_B$ appear in the more general expression for $\langle \Psi_A^* \Psi_B \Psi_C \cdots | \hat{H} | \Psi_A \Psi_B^* \Psi_C \cdots \rangle$.

In practice, the number of significant NTOs needed for the CSF expansions depends on the size and complexity of the fragment; for small molecules, we typically find that only one or two Λ_i are significant. The NTO expansions may therefore be truncated at a specified fraction of the excitation amplitude (norm of $\mathbf{T}$) in order to reduce the length of the summations in Eq. (2.6).

2.2.3 Corresponding Orbital Transformation

To compute matrix elements between non-orthogonal Slater determinants, we turn to the corresponding orbital transformation of Amos and Hall.[32] For a given term in Eq. (2.6), the two sets of spin orbitals associated with the bra and ket will be denoted $\mathbf{l}$ and $\mathbf{r}$, respectively. The sets are Schmidt-orthogonalized amongst themselves and expanded in a common atomic orbital (AO) basis, $\{\chi\}$:

$$\begin{aligned} \mathbf{l} &= \chi \mathbf{L} \\ \mathbf{r} &= \chi \mathbf{R} \, . \end{aligned} \tag{2.8}$$

Let $\mathbf{S}^{\text{LR}} = \mathbf{L}^\dagger \mathbf{S} \mathbf{R}$ denote the (non-diagonal) overlap matrix between the left ($\mathbf{L}$) and right ($\mathbf{R}$) sets of orbitals, where $\mathbf{S}$ denotes the AO overlap matrix. We can then apply left and right unitary transformations that diagonalize $\mathbf{S}^{\text{LR}}$ but leave the original Slater determinants unchanged, except possibly for a phase that is equal to

the determinant of $\mathbf{U}^\dagger$ or $\mathbf{V}^\dagger$:

$$\mathbf{U}^\dagger\mathbf{L}^\dagger\mathbf{S}\mathbf{R}\mathbf{V} = \widetilde{\mathbf{L}}^\dagger\mathbf{S}\widetilde{\mathbf{R}} = \tilde{\mathbf{s}}^{\mathrm{LR}} \, . \tag{2.9}$$

Here, $\tilde{\mathbf{s}}^{\mathrm{LR}}$ is diagonal and the matrices $\mathbf{U}$ and $\mathbf{V}$ are computed from the singular value decomposition of $\mathbf{S}^{\mathrm{LR}}$.

The corresponding orbitals transformation leads to a set of generalized Slater-Condon rules[33] that may be used to compute the Hamiltonian and overlap matrix elements in terms of the AO basis. The overlap matrix element is

$$\begin{aligned} \Xi^{\mathrm{LR}} &= \langle \Phi_A^{ia}\Phi_B | \Phi_A \Phi_B^{kb} \rangle \\ &= \det(\mathbf{U}) \det(\mathbf{V}^\dagger) \prod_i^N \tilde{s}_{ii}^{\mathrm{LR}} \, . \end{aligned} \tag{2.10}$$

Note that the transformations $\mathbf{L}$ and $\mathbf{R}$ depend, implicitly, on the MOs ϕ_i^A, ϕ_a^A, ϕ_k^B, and ϕ_b^B that are involved in the excitation, but for brevity the indices in question are subsumed into the "LR" in Ξ^{LR}. The corresponding matrix element of $\hat{H}$ can be written

$$\langle \Phi_A^{ia}\Phi_B | \hat{H} | \Phi_A \Phi_B^{kb} \rangle = \Omega_1^{\mathrm{LR}} + \Omega_2^{\mathrm{LR}} \tag{2.11}$$

where

$$\Omega_1^{\mathrm{LR}} = \sum_i^N \sum_{\lambda\rho} \widetilde{R}_{\rho i} \left(\frac{\Xi^{\mathrm{LR}}}{\tilde{s}_{ii}^{\mathrm{LR}}} \right) \widetilde{L}_{i\lambda}^\dagger \langle \lambda | \hat{h} | \rho \rangle \tag{2.12}$$

and

$$\Omega_2^{\mathrm{LR}} = \frac{1}{2} \sum_{ij} \sum_{\lambda\rho\mu\nu} \widetilde{R}_{\rho i} \widetilde{R}_{\nu j} \left(\frac{\Xi^{\mathrm{LR}}}{\tilde{s}_{ii}^{\mathrm{LR}} \tilde{s}_{jj}^{\mathrm{LR}}} \right) \widetilde{L}_{i\lambda}^\dagger \widetilde{L}_{j\mu}^\dagger \langle \lambda\mu || \rho\nu \rangle \, . \tag{2.13}$$

The interaction terms for α and β electrons are computed explicitly, so

$$\Omega_1^{\mathrm{LR}} = {}^\alpha\Omega_1^{\mathrm{LR}} + {}^\beta\Omega_1^{\mathrm{LR}} \tag{2.14}$$

and

$$\Omega_2^{\mathrm{LR}} = {}^{\alpha\alpha}\Omega_2^{\mathrm{LR}} + {}^{\beta\beta}\Omega_2^{\mathrm{LR}} + {}^{\alpha\beta}\Omega_2^{\mathrm{LR}} + {}^{\beta\alpha}\Omega_2^{\mathrm{LR}} \ , \tag{2.15}$$

where the spin coupling terms in Eq. (2.15) cause the the antisymmetrized AO integrals, $\langle\lambda\mu||\rho\nu\rangle$ in Eq. (2.13), to be replaced with with Coulomb integrals $\langle\lambda\mu|\rho\nu\rangle$. This fundamentally comes from the vanishing of the exchange contributions to the generalized density matrices in the $\alpha\beta$ case, reflecting the lack of exchange interaction between α and β densities.

2.3 Accuracy

A preliminary version of our *ab initio* fragment molecular exciton method has been implemented in a developer's version of the Q-Chem electronic structure program.[34,35] Unless otherwise noted, all fragment and supersystem calculations were carried out at the CIS level of theory, and "error" in excitation energies obtained for the exciton models is defined with respect to a supersystem CIS calculation using the same basis set. (Since our exciton model is based on the Hartree-Fock Hamiltonian, this is the most appropriate comparison.) A few calculations use monomer basis states computed from density functional theory (DFT), but these results will nevertheless be compared to supersystem CIS calculations because matrix elements of the exciton Hamiltonian are evaluated at the Hartree-Fock level. In this sense, DFT serves only as an alternative means to obtain basis states, but does not fundamentally change the exciton model. Unless otherwise noted, the 6-31G basis set was used for all calculations except those for He_n, for which the 6-311G basis set was used.

2.3.1 Linear Helium Chains

Linear chains of He atoms (with each atom separated by the He_2 equilibrium distance of 1.581978 Å) are a potentially difficult test system as their excited states tend to be fully delocalized across the entire chain. Figure 2.1 plots errors in excitation energies for He_n chains ($n = 2$–30) computed using our exciton model. Results are shown for a variety of exciton bases.

There are two primary approximations in our model. First, the isolated fragment excited states are computed in the absence of interactions with the surrounding fragments. The severity of this approximation can be reduced by including higher-lying fragment excited states in the direct-product basis, which add variational flexibility and allow the excitonic wave functions to deform in response to inter-fragment perturbations. For the weakly-polarizable He_n test systems, however, this approximation is not a significant source of error.

The second approximation is fundamental to the exciton model itself: we assume that each supersystem excitation can be described as a linear combination of excitations localized on individual subunits. Helium chains put this assumption to the test, because their excited states qualitatively resemble those of a particle in a one-dimensional box. Our data show that even such highly delocalized states are well described by the model, so long as the fragment size is sufficient to capture the (relatively localized) charge transfer character of the excited state. For triplet and singlet excited states, fragments made up of two and three He atoms, respectively, are adequate to achieve reasonable accuracy (Fig. 2.1). That the description of singlets

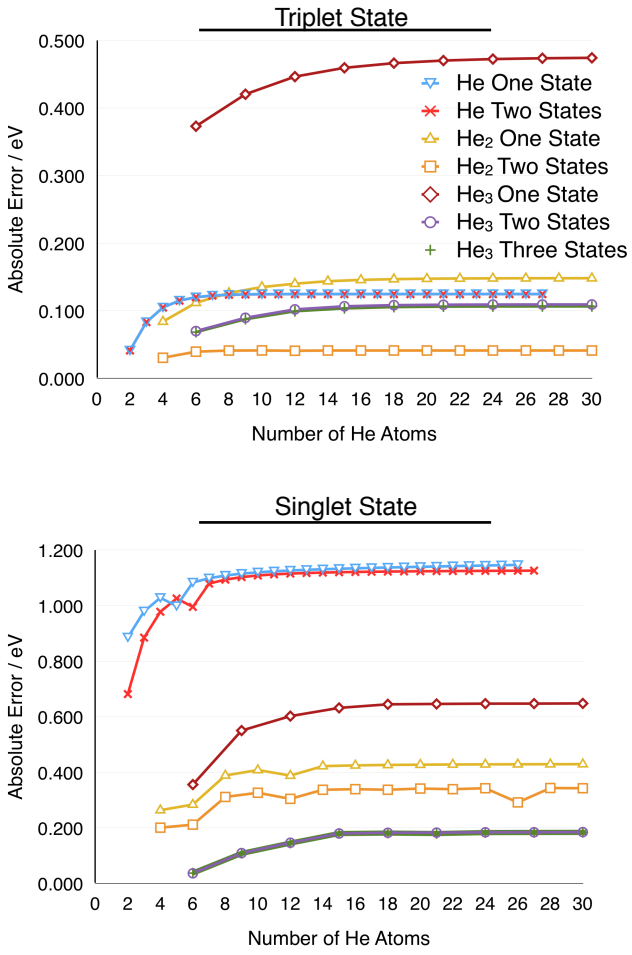

Figure 2.1: Absolute errors (relative to a supersystem CIS/6-311G calculation) in the excitation energy predicted by the exciton model for the lowest triplet and singlet states of He_n chains. Results are shown for several versions of the exciton model, using fragments ranging in size from He to He_3, in conjunction with an excitonic basis consisting of 1–3 excited states per fragment. CIS/6-311G calculations are used also for the fragments. The number of NTOs retained per fragment is equal to the number of He atoms per fragment, as this is sufficient to recover essentially the full norm of the transition density matrix.

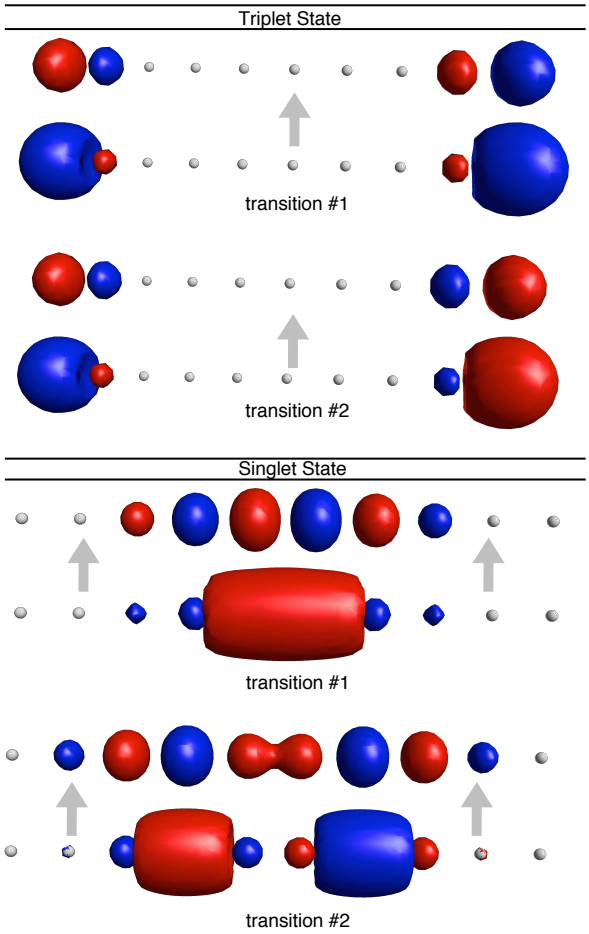

Figure 2.2: Plots of the two dominant NTOs for the lowest singlet and triplet excitations of a He_{10} chain. (An isosurface value of 0.05 a.u. is used in each case.) Each pair of particle/hole NTOs for the triplet state accounts for 38.5% of the norm of the transition density matrix, while in the singlet case the two NTO pairs account for 60.3% (upper pair) and 24.1% (lower pair) of the norm.

requires additional fragment states, relative to the triplet case, makes sense in view of the fact that Pauli repulsion tends to delocalize singlet excitations to a greater extent than triplet excitations. Analysis of the supersystem NTOs for He_{10} (Fig. 2.2) shows that the overall excitation is well represented as a combination of relatively localized excitations, the sizes of which correspond roughly to the two and three He atoms per fragment that afford good results in the triplet and singlet exciton models, respectively.

2.3.2 Water Clusters

The collective nature (or lack thereof) of the excited states of water has been a subject of some debate.[36] We have used our method to compute the excitation energies of water clusters at their equilibrium geometries and the results are given in Fig. 2.3. (Geometries are MP2/cc-pVDZ, from Ref. 2.) Relative to the He_n results, the excited states of $(H_2O)_n$ are *not* well represented by adiabatic fragment states, as reflected in the large errors reported in Fig. 2.3. By including three excitations per H_2O fragment, however, we obtain excellent agreement with supersystem calculations, with errors that are generally less than 0.1 eV. We find that these results are robust with respect to the choice of AO basis set as well, and similar results are obtained in the 6-31+G* basis.

We select an $(H_2O)_7$ cluster from our test set as an illustrative example. As shown by the NTOs in Fig. 2.4, the excitation primarily involves transitions localized on monomers 1 and 3 with minimal intermolecular excitation transfer. Comparing this picture to the coefficients of the exciton eigenvector computed with our method, as

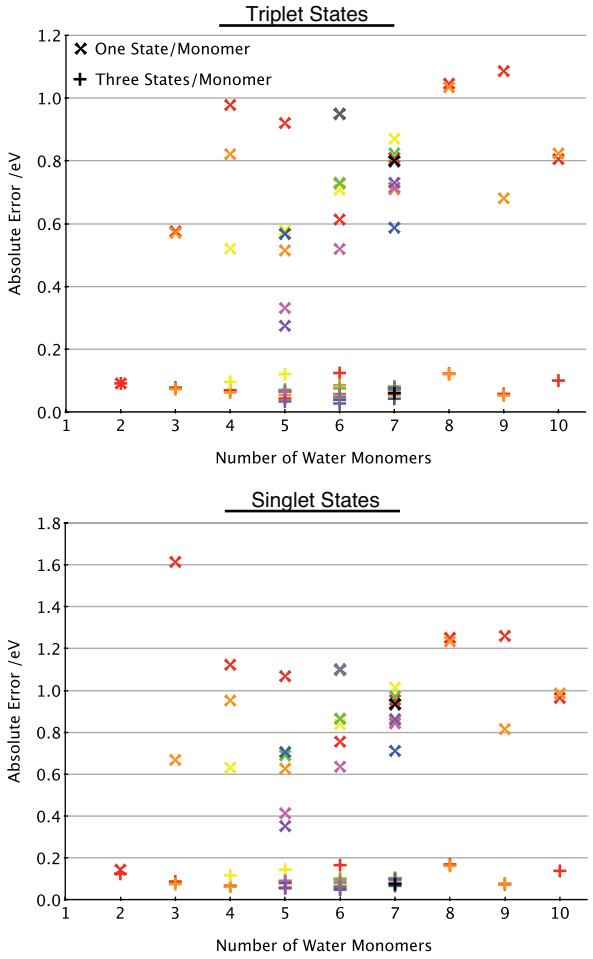

Figure 2.3: Absolute errors[a] for the lowest triplet and singlet excitation energies for various isomers of water clusters, relative to supersystem CIS/6-31G excitation energies. The various colors refer to different cluster isomers.

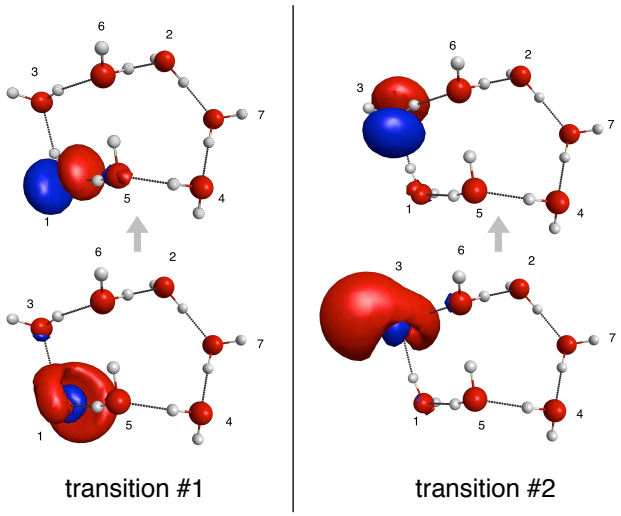

Figure 2.4: Plots of the two dominant NTOs for the first triplet excitation of an $(H_2O)_7$ cluster. The NTO particle/hole pairs account for 76% and 14% of the overall transition respectively. (The isosurface value for all plots is 0.05 a.u.) Numbers indicate the monomer index of the adjacent molecule.

Table 2.1: Amplitudes for the first triplet excitation of the $(H_2O)_7$ cluster shown in Fig. 2.4.

Monomer	1	2	3	4	5	6	7
			One State Per Monomer				
	0.581	−0.000	0.813	−0.001	−0.009	−0.009	0.000
			Three States Per Monomer				
State 1	0.832	−0.000	0.078	−0.001	−0.010	−0.000	0.000
State 2	0.034	0.000	−0.000	−0.000	0.003	0.000	−0.000
State 3	0.421	−0.000	−0.353	−0.000	0.020	−0.000	0.000

provided in Table 2.1, we find that the excitonic wave function is dominated by basis states involving excitation of precisely these two water monomers. This behavior is typical, and shows how the exciton approximation still captures the fundamentals of the supersystem excited state for realistic molecular clusters. Note that the relative magnitude of the dominant states are reversed when compared to the corresponding localized NTO amplitudes. This is due to neglect of intermolecular polarization, and largely disappears when higher-lying monomer excited states are included in the excitonic basis.

2.3.3 Alternative Basis States

An exciton approach is essentially a variational energy minimization in a strategically chosen trial basis. Accordingly, determination of the fragment orbitals for the basis states need not be limited to a particular quantum chemistry method, so long as they accurately represent the excited state(s) of the fragment. Kohn-Sham orbitals and TDA-TDDFT coefficients C^{ia} offer a basis that includes some intra-fragment electron correlation. It is also well known that Kohn-Sham orbitals are more representative of electronic excitations as compared to Hartree-Fock orbitals,[37] which bear more resemblance to ionized states. Indeed, we find that NTO expansions are generally more compact for TDDFT excited states as compared to their CIS counterparts, which proves useful in reducing computational time when the monomer units are large (see Section 2.3.4). Here, we use the B3LYP functional to compute monomer basis states for water clusters. The results, shown in Table 2.2, demonstrate that the B3LYP-based approach is slightly more accurate for water clusters, as compared

to the same exciton model constructed from CIS monomer wave functions. (This conclusion is not true for all of the systems that we have explored, however; see below.)

For systems comprised of polar monomers, another way to augment the adiabatic approximation is to compute monomer wave functions in the presence of some classical representation of the electrostatic environment of the supersystem, *e.g.*, by embedding the monomer calculations in a field of atom-centered point charges on the other monomers. The variational "XPol" (explicit polarization) approach of Xie *et al.*[38] uses a self-consistent charge embedding procedure to accomplish this, and here we use XPol in conjunction with "ChElPG" charges that are fit to reproduce the molecular electrostatic potential outside of the van der Waals region. (See Refs. 39 and 40 for details of the combined XPol + ChElPG algorithm.) The polarized MOs generated by the XPol procedure are then used to perform CIS calculations on the fragments.

Results in Table 2.2 show that the use of XPol wave functions significantly enhances the accuracy of the exciton model for water clusters; in particular, use of a single XPol CIS state per monomer is as accurate as three adiabatic (gas-phase) states per monomer. This combination presents a highly appealing route for economical excited-state calculations in clusters, providing accuracy within 0.2 eV of supersystem calculations with only a minimal basis.

2.3.4 Results for Large Systems

We next consider whether comparable accuracy is maintained in larger systems. Table 2.3 shows errors in the exciton model for several snapshots of a $(H_2O)_{57}$ cluster and

Table 2.2: Mean unsigned errors[a] (MUEs, in eV) for $S_0 \rightarrow S_1$ and $S_0 \rightarrow T_1$ excitation energies for small water clusters computed using various exciton models.

Basis	State	No. of Water Molecules								
		2	3	4	5	6	7	8	9	10
HF/6-31G (1 state)	T_1	0.09	0.57	0.77	0.54	0.77	0.65	1.06	0.88	0.82
	S_1	0.14	1.14	0.90	0.65	0.91	0.79	1.25	1.04	0.98
HF/6-31G (2 states)	T_1	0.09	0.57	0.71	0.53	0.76	0.65	1.04	0.87	0.81
	S_1	0.12	0.08	0.08	0.08	0.07	0.13	0.11	0.07	0.12
HF/6-31G (3 states)	T_1	0.09	0.08	0.08	0.06	0.06	0.13	0.09	0.06	0.10
	S_1	0.12	0.08	0.08	0.09	0.09	0.14	0.12	0.08	0.14
HF/6-31+G* (1 State)	T_1	0.21	0.51	0.65	0.52	0.68	0.66	0.96	0.77	0.75
	S_1	0.27	0.61	0.77	0.65	0.82	0.80	1.15	0.92	0.94
HF/6-31+G* (2 State)	T_1	0.20	0.50	0.63	0.51	0.66	0.65	0.94	0.75	0.74
	S_1	0.15	0.18	0.21	0.21	0.22	0.22	0.38	0.24	0.33
HF/6-31+G* (3 State)	T_1	0.13	0.13	0.15	0.14	0.15	0.15	0.21	0.14	0.21
	S_1	0.16	0.190	0.26	0.28	0.32	0.36	0.52	0.43	0.60
B3LYP/6-31G (1 state)	T_1	0.01	0.48	0.65	0.44	0.64	0.55	1.00	0.52	0.66
	S_1	0.05	1.01	0.74	0.52	0.74	0.63	1.11	0.64	0.78
B3LYP/6-31G (2 states)	T_1	0.01	0.47	0.64	0.44	0.63	0.54	0.98	0.51	0.65
	S_1	0.04	0.47	0.06	0.04	0.06	0.13	0.28	0.27	0.02
B3LYP/6-31G (3 states)	T_1	0.01	0.02	0.06	0.04	0.05	0.12	0.28	0.27	0.03
	S_1	0.04	0.47	0.06	0.04	0.06	0.12	0.28	0.27	0.02
XPol-HF/6-31G (1 state)	T_1	0.06	0.06	0.07	0.07	0.06	0.06	0.14	0.08	0.10
	S_1	0.11	0.06	0.07	0.08	0.07	0.07	0.16	0.08	0.11
XPol-HF/6-31+G* (1 state)	T_1	0.10	0.17	0.65	0.52	0.68	0.66	0.98	0.77	0.75
	S_1	0.13	0.20	0.77	0.65	0.82	0.80	1.19	0.92	0.94
XPol-HF/6-31+G* (2 state)	T_1	0.10	0.17	0.24	0.22	0.27	0.25	0.57	0.29	0.47
	S_1	0.10	0.20	0.25	0.24	0.27	0.28	0.38	0.34	0.32
XPol-HF/6-31+G* (3 state)	T_1	0.07	0.12	0.16	0.14	0.16	0.16	0.27	0.18	0.22
	S_1	0.10	0.17	0.20	0.20	0.23	0.21	0.38	0.23	0.31

[a]With respect to a supersystem CIS calculation using the same AO basis set.

Table 2.3: Absolute errors[a] (in eV) in $S_0 \rightarrow S_1$ and $S_0 \rightarrow T_1$ excitation energies for large water clusters extracted from a simulation.

Snapshot	$(H_2O)_{57}$		$(H_2O)_{117}$	
	T_1	S_1	T_1	S_1
1	0.154	0.232	0.054	0.148
2	0.106	0.177	0.049	0.084
3	0.246	0.323	0.046	0.159
4	0.181	0.261		
5	0.296	0.178		

[a]With respect to a supersystem CIS/ 6-31G calculation, using a one-state Hartree-Fock basis.

a $(H_2O)_{117}$ cluster that were extracted from simulations of liquid water. The errors for these systems tend to be less than similar calculations in Table 2.2 including one excitation per fragment. The water molecules from these simulations are generally further apart than those in equilibrium (*i.e.*, cluster) geometries with fewer hydrogen bonds between adjacent molecules. This results in weaker inter-fragment interactions such that the unperturbed fragment MOs better represent the supersystem than they do in the case of geometry-optimized clusters. Furthermore, increasing the number of fragments effectively increases the variational space and stabilizes the excited states, as can be seen by the decrease in error going from the $(H_2O)_{53}$ to $(H_2O)_{117}$.

Tests for clusters of conjugated organic chromophores are shown in Table 2.4. These include clusters of pentacene, $C_{22}H_{14}$, a material that has been widely discussed

Table 2.4: Absolute errors[a] in the $S_0 \rightarrow T_1$ excitation energy for two systems composed of larger monomers.

Cluster	Exciton Basis	Threshold (%)	Error (eV)
$(NDI)_2$	HF/6-31G	95	0.014
$(NDI)_2$	HF/6-31G	85	0.142
$(NDI)_2$	HF/6-31+G*	85	0.129
$(NDI)_2$	B3LYP/6-31G	90	0.282
$(NDI)_6$	B3LYP/6-31G	90	0.327
$(NDI)_9$	HF/6-31G (Bright State)	85	0.108[b]
$(pentacene)_2$	HF/6-31G	95	0.010
$(pentacene)_2$	HF/6-31G	85	0.110
$(pentacene)_2$	HF/6-31+G*	85	0.114
$(pentacene)_2$	B3LYP/6-31G	85	0.357
$(pentacene)_6$	B3LYP/6-31G	85	0.364

[a]With respect to a supersystem CIS calculation in the same AO basis set, using one state per monomer. [b]Bright state error, relative to supersystem S_{30}.

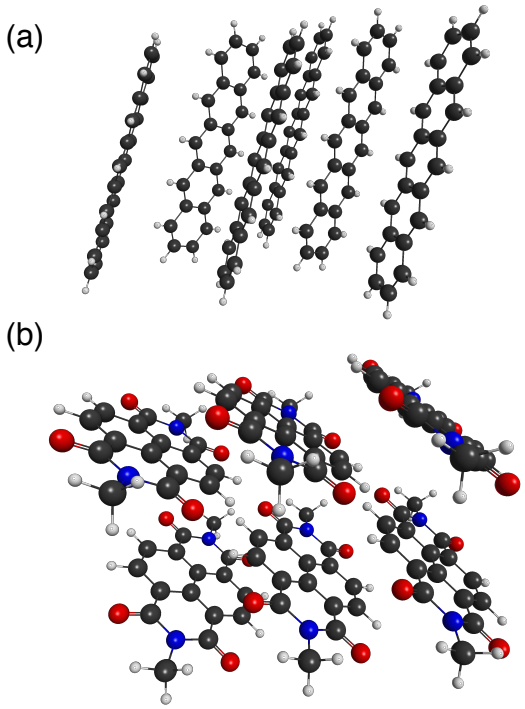

Figure 2.5: Structures of (a) $(\text{pentacene})_6$ and (b) $(\text{NDI})_6$.

in the context of singlet fission,[41] along with clusters of a methylated napthalenediimide (NDI) chromophore that forms the basic building block of a self-assembling nanotube.[7,8] These structures are shown in Fig. 2.5. (The pentacene cluster is obtained from the crystal structure of the "LT" polymorph reported in Ref. 42. Structural parameters for the NDI nanotube were obtained from Ref. 8.) We find that the exciton model affords excellent agreement with supersystem calculations for these systems, with errors as low as 0.01 eV, however the accuracy is highly sensitive to the choice of fragment MOs included in the basis. As compared to previous examples, the NTO expansions for these more complex molecular fragments include a greater number of significant terms that must be included in Eq. (2.6) for the matrix elements. Whereas in previous examples we included a fixed number of NTOs, in these examples it is prudent to truncate the expansions at some fixed fraction of the excitation amplitude. We have found that a threshold of 85% of the norm of $\mathbf{T}$ provides a reasonable balance of performance and accuracy. The use of fragment MOs from DFT calculations, in this case calculated with the B3LYP functional, is another means of reducing the computational cost since their NTO expansions tend to include fewer terms. For the examples in Table 2.4, however, we find that the accuracy of B3LYP MOs in the exciton model is inferior to that of HF MOs. Further testing is required to understand whether this is a deficiency related to the use of B3LYP or, more fundamentally, to the very use of Kohn-Sham MOs.

2.3.5 Comparison to the Renormalized Exciton Model

Recently, Ma and co-workers[26,27] developed a "renormalized" exciton model (REM), in which an effective Hamiltonian is constructed by projecting various n-body Hamiltonians (for $n = 2$ or 3 subunits) onto an excitonic direct-product basis. In Table 2.5, we compare the results of that approach to the present Frenkel-Davydov-type model, in the case that both techniques employ CIS/STO-6G wave functions. As with the linear helium chains, this is an extreme case due to the highly delocalized nature of the excited states, and results using our method are rather poor when the excitonic basis is constructed from H_2 dimers. Adding higher-lying excited states does not improve the situation, because it is delocalization rather than polarization that limits the accuracy in these cases. However, results are improve significantly when larger segments of the chain are used to construct the basis states, and for basis states constructed using half the chain [$(H_2)_{n/2}$ in Table 2.5], errors in the $S_0 \rightarrow T_1$ excitation energy are comparable to those obtained using REM-CIS, although generally larger for the $S_0 \rightarrow S_1$ excitation.

In comparison, the REM-CIS results do an impressive job of capturing these highly delocalized excitations using smaller monomer units. Note, however, that extension of the REM approach to more realistic three-dimensional systems is slightly complicated, given that the number of n-body interactions included in the REM effective Hamiltonian scales as $\binom{N}{n}$ for N fragments. Terms beyond $n = 2$ are often critically important to the accuracy of ground-state many-body approaches,[43] and their importance should presumably increase in the excited state, given the increased size and

Table 2.5: Errors for linear H_2 chains[a] from the REM-CIS method and our Frenkel-Davydov exciton model.

System	Error[b] / mHartree					
	$S_0 \rightarrow T_1$			$S_0 \rightarrow S_1$		
	REM	this work[c]		REM	this work[c]	
	(Ref. 27)	$(H_2)_2$	$(H_2)_{n/2}$	(Ref. 27)	$(H_2)_2$	$(H_2)_{n/2}$
1.5 R_e						
$(H_2)_6$	−8.68	69.78	39.60	−17.73	128.92	77.22
$(H_2)_8$	−13.31	76.52	29.40	−22.27	142.53	60.92
$(H_2)_{10}$	−15.86	79.70	22.14	−23.24	149.15	48.28
$(H_2)_{12}$	−17.39	81.38	17.02	−23.23	152.73	38.76
2.0 R_e						
$(H_2)_6$	−5.58	32.01	16.64	−17.73	81.87	44.79
$(H_2)_8$	−8.53	34.42	11.23	−24.29	87.51	31.63
$(H_2)_{10}$	−10.13	35.49	7.93	−27.55	89.89	23.30
$(H_2)_{12}$	−11.08	36.03	5.83	−29.22	91.05	17.85

[a]Using the equilibrium bond length of $R_e = 0.7414$ Å and an intermolecular separation of either 1.5 or 2.0 times R_e. [b]With respect to a supersystem CIS calculations, STO-6G basis.
[c]With basis states as indicated.

polarizability of the excited-state wave function. Our *ab initio* exciton approach, on the other hand, includes many-body Coulomb and exchange effects and is essentially a "black box" and whose application to any system is straightforward.

2.3.6 Size-Consistency Considerations

Supersystem CIS calculations are rigorously size-consistent,[9] in the customary supermolecular sense of the term. Non-orthogonal CI can be made to satisfy size-consistency of the total energy (meaning that the total energy for a system of well-separated fragments is equal to the sum of the fragment energies), and also size-intensivity of excitation energies (meaning that the excitation energy is unaffected by the addition of a distant and therefore non-interacting fragment).[44] These facts are straightforward to verify since off-diagonal coupling elements of the exciton Hamiltonian vanish in the limit of large inter-fragment separation.

Although often conflated with size-consistency, *size-extensivity* is more properly defined as a non-vanishing correlation energy per particle in the thermodynamic (infinite, periodic) limit. This property has been considered carefully by Hirata,[45] although he calls it *size-consistency*, for reasons explained in Ref. 45, and concludes that CIS is rigorously size-extensive provided that the HF determinant is used as the reference state. In contrast, the reference state for our Frenkel-Davydov exciton model is composed of HF MOs from multiple, independent fragment calculations, hence the formal requirements of size-extensivity are not met. This opens the possibility of increasing, size-dependent errors for interacting systems. This issue was also pointed out by Sundholm and Head-Gordon,[44] who note that in a non-orthogonal

CI calculation, an increasing [but only as $\mathcal{O}(N^2)$] number of determinants may be required to achieve a comparable level of accuracy as system size grows, yet excitation energies remain size-intensive in the sense defined above.

Our model does not satisfy Brillouin's theorem, hence size-inconsistency may manifest as spurious stabilization of the ground-state direct-product wave function via mixing with the excitonic basis functions. This could potentially result in an unbalanced treatment of the excited states relative to the ground state, and errors that might increase as the size of the excitonic basis increases. Since the basis functions are spin eigenstates, for a singlet ground state this stabilization appears only when computing singlet excited states. We may therefore quantify the extent of this stabilization by comparing the ground-state eigenvalue of the exciton Hamiltonian in the singlet ($S_0 \rightarrow S_n$) and triplet ($S_0 \rightarrow T_n$) excitation cases.

For linear He chains, using single He atoms as monomer units, the aforementioned stabilization is found to increase linearly with system size at the rate of 0.005 mHartree/monomer. However, errors in singlet excitation energies mirror those for triplet excitation, and are essentially constant for $N > 10$ He atoms (see Fig. 2.1). Despite the linear growth in the ground-state stabilization per monomer, in actuality this effect is dictated not so much by system size but rather by the size of the direct-product basis. This is particularly evident in our data for water clusters computed using the 6-31+G* basis (Table 2.2), where the inclusion of three excited states per monomer slightly increases the errors in excitation energy of the singlet case, relative to errors obtained using two excited states per monomer. No corresponding

effect is observed for triplet excitations, and we attribute this effect to ground-state stabilization in the singlet case.

This effect can be ameliorated using XPol monomer wave functions, as is evident in the water cluster data in Table 2.2. XPol allows the primary orbital relaxation effects in the ground state to be included explicitly in the monomer wave functions, so that there is less of a driving force for mixing excited-state direct-product wave functions into the ground state. In general, we find that errors stemming from size-inconsistency are quite small and our exciton method performs well when compared to rigorously size-consistent supersystem CIS calculations, even for the sizable systems that we have explored.

2.4 Performance

2.4.1 Bottlenecks

The SVD step of the corresponding orbitals transformation in Eq. (2.8) formally scales as $\mathcal{O}(N^3)$ but with a very small prefactor. In practice, the overall computational cost is dominated by contraction of two-electron integrals with a density matrix to form a Fock-like matrix:

$$F_{\lambda\rho} = \sum_{\mu\nu} \langle \lambda\mu || \rho\nu \rangle P_{\mu\nu} \; . \tag{2.16}$$

For the exciton model, $P_{\mu\nu}$ is a generalized density matrix whose form is suggested by Eq. (2.13):

$$P_{\mu\nu} = \sum_{j} \widetilde{R}_{\nu j} \left(\frac{\Xi^{LR}}{\tilde{s}^{\mathrm{LR}}_{jj}} \right) \widetilde{L}^{\dagger}_{j\mu} \; . \tag{2.17}$$

The cost of the contraction in Eq. (2.16) scales as $\mathcal{O}(N_{\text{basis}}^{x})$ where $2 \leq x \leq 4$, depending on system size and integral thresholds.

Construction of each exciton matrix element [Eq. (2.6b)] requires $\mathcal{O}(N_{\text{NTO}}^{2})$ contraction steps, where N_{NTO} is the number of NTO pairs retained in the CI expansion of the individual fragment excited states. We note that the primary bottleneck is not generation of the AO integrals $\langle \lambda\mu || \rho\nu \rangle$, but rather their digestion [Eq. (2.16)] with numerous generalized density matrices. We are currently pursuing ways to accelerate this step.

In total there are $N_{\text{frgm}}(N_{\text{frgm}}+1)/2$ matrix elements of the exciton Hamiltonian to compute so total CPU time scales as $\mathcal{O}(N_{\text{frgm}}^{2} N_{\text{basis}}^{x})$. Memory usage is favorable; each matrix element requires several $N \times n_{\text{basis}}$ arrays, where n_{basis} is the number of basis functions per monomer, although our implementation will happily exploit additional memory for efficient integral evaluation. The same is true for disk storage, requiring only the occupied and a few virtual NTOs from each fragment to be stored in the fragment basis sets.

Traditional supersystem CIS and TDDFT calculations employ Davidson iteration to diagonalize the singly-excited block of the CI Hamiltonian. The number of iterations required to reach convergence varies with the system and number of desired eigenvalues but is typically 10–30 iterations when several (but $\ll 30$) eigenvalues are requested. For each Davidson iteration, the rate-determining step is the contraction of the AO two-electron integrals with subspace trial vectors. This is directly related to the contraction step written in Eq. (2.16), in that $P_{\mu\nu}$ is the pseudo-density matrix

of Maurice and Head-Gordon.[46] Memory requirements are the same as above but all occupied and virtual orbitals in the supersystem basis set must be stored.

In view of these considerations, one can straightforwardly conclude that total CPU time is minimized by the method that requires the fewest instances of the digestion step in Eq. (2.16). In general, supersystem methods are highly efficient at minimizing this step as well as the overall single-threaded CPU time. However, the scaling of this performance is limited for modern computer architectures, and below we discuss the performance of an implementation in which calculation of the exciton matrix elements is distributed across cores.

2.4.2 Parallelization

The serial efficiency of traditional supersystem methods is highly optimized but the potential for parallelization is fundamentally limited by their iterative nature; each step requires the results of the previous iteration before it can proceed. The work done in each iteration can be parallelized, *e.g.*, the integrals in Eq. (2.16) can be batched into different tasks. This approach scales fairly well across the cores of a single node but efficiency is reduced, often significantly, by latencies in communication when scaling across nodes is required.

Our method is designed to overcome both of these limitations. Iterations are limited to fragments only, and the matrix element calculations are entirely independent of one another and thus trivial to distribute across any arrangement of processors. In fact, inter-node parallelism could further be augmented by shared memory intra-node parallelism. We have a implemented a parallel version of our method (based on

Table 2.6: Wall clock times for parallel computation of the lowest triplet excitation of GC base pair clusters.

N_{frgm}	No. cores	Wall Time / sec		
		Exciton Model[a]		Full CIS
		75%[b]	85%[c]	
2	3	43	158	2961
4	10	347	1130	9553
6	21	908	3175	14178
8	36	1760	6253	9886
12	75	4605	15578	24096

[a]Estimated wall time for parallel calculation on $N(N+1)/2$ processers. [b]Absolute errors are $\sim$0.2 eV for this threshold. [c]Absolute errors are $\sim$0.1 eV for this threshold.

the Message Passing Interface, MPI) that parallelizes matrix element computations across cores within a distributed memory model. Given $N_{\text{frgm}}(N_{\text{frgm}}+1)/2$ cores, the total wall time is essentially reduced to the time to compute a single matrix element. Given this degree of parallelism, the wall time required for our exciton model will be less than that of a traditional supersystem CIS calculation if the number of terms in Eq. (2.6), each of which requires one instance of a contraction such as that shown in Eq. (2.16), is fewer than the number Davidson iterations necessary to converge the supersystem calculation. Due to the efficient scaling of our method across processors this can still be true when considering parallel performance of supersystem methods on equivalent hardware, as shown below.

Chemical insight into the nature of the electronic states of the system of interest

can be applied to the fragment partitioning in order to minimize cost while maintaining accuracy. For example, the lowest triplet excitation of a gas-phase guanine–cytosine (GC) base pair is highly localized on the the cytosine moiety but is significantly stabilized by hydrogen bonding to the other base. This suggests using base pairs, rather than individual nucleobases, to generate basis states for clusters or π stacks. Timing data for various clusters of GC base pairs are given in Table 2.6 (The GC dimer structure was taken from Ref. 47 and stacked to form larger systems.)

The timing data for the exciton models presented in Table 2.6 are estimated from the time required for the computation of a single matrix element, as the fragment SCF and CIS calculations represent negligible overhead, as does diagonalization of the exciton Hamiltonian matrix, therefore the wall time is essentially limited by the computation of a single matrix element. The NWChem program[48] was used fas a benchmark for the parallel supersystem calculations, which is somewhat incongruous because the exciton model is implemented in Q-Chem, which exhibits far better serial performance as compared to NWChem. However, NWChem is generally recognized as a state-of-the-art for scalability (and Q-Chem's implementation of TDDFT does not scale to the number of cores indicated in Table 2.6), thus the comparison presented in Table 2.6 is at least interesting. By taking advantage of nearly perfect parallel scaling, the exciton method can indeed outperform a traditional supersystem calculation on equivalent hardware by up to a factor of 15, with errors in excitation energies of ≈ 0.2 eV. Of course, for systems composed of very large monomer units, the embarrassing parallelism of the exciton model could be combined with a parallel

implementation of CIS to compute the fragment excited states, and (more importantly) a parallel version of the digestion step in Eq. (2.16), in order to parallelize calculation of the individual matrix elements.

2.5 Possible Improvements and Extensions

Results presented above suggest that our *ab initio* exciton model is indeed a useful starting point for efficient calculation of collective excitations in multi-chromophore systems. Several ways in which this basic model might be improved or extended are sketched in this section.

2.5.1 Targeted States

Thus far we have only discussed application of our *ab initio* exciton method to the lowest-lying excited state of a given spin symmetry. Due to the physically-based nature of the model, however, we can use it to target specific higher-lying states of molecular aggregates, with potentially dramatic savings in computational cost. For example, in the $(NDI)_9$ calculations reported in Ref. 8, the lowest optically-bright state was S_{28}, with spacings of ~ 0.05 eV between lower-lying, optically-dark states. TDDFT Calculations reported in Ref. 8 used the 3-21G* basis set, but for a larger number of NDI chromophores or a higher-quality basis set, the position of the bright state would inevitably move further up the manifold of singlet excited states. The need to calculate so many eigenvalues manifests as very large storage (memory and/or disk) requirements.

Application of chemical insight into the properties of the aggregate state of interest can dictate the proper choice of fragment states to include in the exciton basis, such that the specific supersystem excitation of interest is targeted. An example is the calculation of the lowest optically-bright state of $(NDI)_9$. The bright state of the NDI aggregate involves a linear combination of the monomers in their spectroscopically active excited states. Supersystem methods that utilize the traditional Davidson algorithm simply solve for the requested number of lowest-lying eigenstates, and the state of interest is determined *a posteriori* by the user.

In a supersystem CIS or TDDFT calculation, the contraction in Eq. (2.16) must be computed for each unconverged root at each Davidson iteration, and the resulting matrices [$F_{\lambda\rho}$ in Eq. (2.16)] of dimension $N_{\text{basis}} \times N_{\text{basis}}$ must be stored. (Recall that N_{basis} refers to the supersystem.) For large systems composed of large monomers, this is a significant burden and parallel scaling suffers from the same limitations outlined earlier. The exciton model effectively sidesteps this increase. In order to target the bright state of the cluster, basis states are chosen to be the spectroscopically active excited states of the monomers, determined by the orientation and magnitude of the monomer transition dipole moments.

For NDI at the CIS/6-31G level of theory, the fourth CIS root corresponds to the spectroscopically-bright monomer excitation. Using these fragment states as an excitonic basis will then target the bright state of the cluster. Unlike supersystem methods, computing higher-lying excited states for the exciton model has essentially

has the same computational cost as computing low-lying states because diagonalization of the exciton Hamiltonian matrix is trivial. Any increase in cost for higher-lying states arises from computing a few extra excited states for the fragments. The CPU and memory requirements for the exciton calculation are effectively unchanged. The results for this exciton calculation, reported in Table 2.4, agree well with supersystem methods while finishing 30% faster when both calculations were run on 12 cores.

2.5.2 Correlation Corrections

As a final demonstration of the value of the distinct physical partitioning used in our method, we present (albeit without rigorous derivation in this work) an approximate means of including electron correlation effects in the excitation energies without increasing the cost of the calculation. Due to the locality of electron correlation effects, it is not unreasonable to make the approximation that their contribution to excitation energies in an aggregate are primarily due to electron correlation within fragment units and thus to neglect inter-fragment electron correlation. If we then consider correlation to be a weak perturbation that only minimally deforms each fragment wave function, correlation effects can also be neglected in excitonic couplings. With these two approximations we can then treat the correlation for an exciton calculation as straightforward perturb-then-diagonalize correction.

In practice, we compute the correlation energies of the ground and excited states of each fragment at the MP2 and CIS(D) levels,[49] respectively, then add this correlation correction to the diagonal elements of the exciton Hamiltonian, weighted by the corresponding overlap elements. Even given this seemingly crude set of approximations,

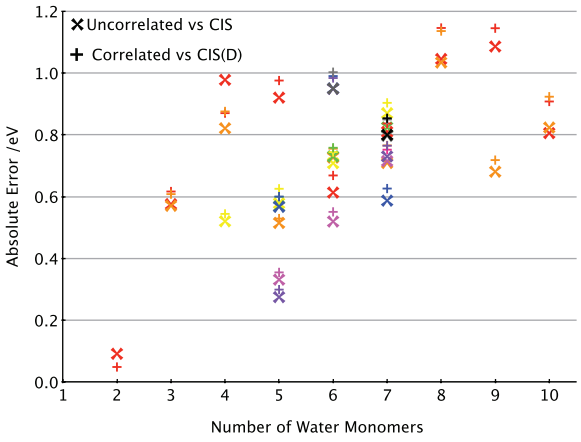

Figure 2.6: Absolute errors for water clusters with and without correlation corrections to the exciton model. Different colors at a given cluster size refer to different isomers, and the basis consists of a single CIS/6-31G state per monomer.

we have found that the resulting errors for excitation energies, relative to correlated CIS(D) supersystem calculations, is not significantly worse than the agreement documented above when the uncorrelated exciton model is compared to supersystem CIS calculations.

Both sets of errors [versus CIS and versus CIS(D)] for water clusters are presented in Fig. 2.6, and we have similar accuracy for organic chromophores as well. A correlation corrected calculation on the GC dimer had the same 0.1 eV absolute error relative to a supersystem CIS(D) as an equivalent uncorrected exciton calculation relative to supersystem CIS. Errors approach or exceed 1 eV for the larger systems in Fig. 2.6, probably because only a single excited state per monomer is included in the excitonic basis. [The formalism to include more than one state per monomer at

a correlated level of theory is under development in our group.] Although the correlated supersystem calculations scale as $\mathcal{O}(N^5)$, this correction is effectively free for the exciton calculation, since the computational effort in computing excited states of any one monomer, even including correlation effects, is small in comparison to the cost of computing the matrix elements of the exciton Hamiltonian.

2.6 Conclusions

We have introduced a novel method for computing excited states of aggregates based on an *ab initio* implementation of an exciton model. An excitonic basis is constructed from direct products of fragment configuration state functions and exact matrix elements of the Hartree-Fock Hamiltonian are computed using the corresponding orbitals transformation. This approximation has been shown to maintain accuracy, even for highly delocalized excitations, so long as basis states are chosen appropriately. Errors < 0.1 eV for water clusters and $\sim$0.3 eV for organic chromophores are reported. Furthermore, the excitonic basis can be expanded with higher-lying fragment excitations in order to capture polarization effects and thereby increase the accuracy. Kohn-Sham orbitals and especially explicitly polarized (XPol) fragment orbitals perform well as an excitonic basis. A straightforward application of chemical insight can help specify the choice of the excitonic basis to increase accuracy and reduce cost. Notably, it is possible to target a specific aggregate excitation based on the choice monomer states included in the basis.

Due to its near-perfect scaling with parallel hardware, our method can outperform supersystem methods for certain systems despite the fact that, as of now, total CPU time scales unfavorably relative to supersystem methods. We believe that our approach presents a strong theoretical and computational foundation for the design of excited-state algorithms that are capable of scaling to massively-parallel computer architectures while maintaining an unambiguous physically motivated strategy. Future work will focus on reducing the scaling of this method, most likely by reducing the dimension of the orbitals included in the exact Hamiltonian via distance-based charge-embedding approximations. Accurate correlation effects, hinted at in Section 2.5.2, will be rigorously derived, along with a formal derivation of a perturbative approach applicable to an exciton Hamiltonian. Finally, we note that this method is potentially well-suited to be implemented on GPUs and other massively-parallel vector accelerators. We intend to report on these developments in future publications.

CHAPTER 3

Low-Scaling Quantum Chemistry Approach to Excited-State Properties, via an *ab Initio* Exciton Model: Application to Excitation Energy Transfer in a Self-Assembled Nanotube

We introduce a charge-embedding scheme for an excited-state quantum chemistry method aimed at weakly-interacting molecular aggregates. The Hamiltonian matrix for the aggregate is constructed in a basis of direct products of configuration-state functions for the monomers, and diagonalization of this matrix affords excitation energies within ∼0.2 eV of the corresponding supersystem calculation. Both the basis states and the coupling matrix elements can be computed in a distributed way, resulting in an algorithm whose time-to-solution is independent of the number of chromophores, and we report calculations on systems with almost 55,000 basis functions using fewer than 450 processors. In a semiconducting organic nanotube, we find evidence of ultrafast, coherent dynamics followed by energy localization driven by static disorder. Truncation of the model system has a qualitative effect on the energy-transfer dynamics, demonstrating the importance of simulating an extended portion of the nanotube, which is not feasible using traditional quantum chemistry.

3.1 Introduction

Excitation energy transfer is a fundamental step in both natural and artificial light harvesting systems and quantum chemical approaches can provide crucial mechanistic insight into these processes. A well-studied example is the Fenna-Matthews-Olson (FMO) complex, where the suggestion that quantum coherence enhances the energy transfer rate has received significant attention.[50–52] The FMO complex is a trimer in which each monomer is composed of eight bacteriochlorophyll chromophores, hence *ab initio* description of the chromophores within a single monomer is already fairly ambitious using traditional excited-state electronic structure methods, yet semi-empirical studies have shown that consideration of the full trimer has a significant impact on the energy transfer dynamics, even within a single monomer of the FMO trimer.[53] In simulations, the role of quantum coherence in FMO is highly sensitive to how the chromophore energies and couplings between them are described,[54,55] and recent model studies of the full light harvesting complex (involving thousands of bacteriochlorophylls) have demonstrated efficient long-range energy transfer in these nanoscale systems.[56] Large-scale, atomistic *ab initio* studies may provide valuable insight into energy transfer in light harvesting systems, organic photovoltaics, and other interesting optical materials, yet these calculations are prohibitively expensive using traditional *ab initio* quantum chemistry.

The challenge stems from the steep computational scaling of quantum chemistry with respect to system size combined with the sizable model systems necessary to describe solar light harvesting. The cost of even the most affordable *ab initio* methods

for excited states grows as the fourth power of system size. Moreover, traditional quantum chemistry methods (at least when they are optimized for efficiency on one or a few processors) tend to scale poorly on modern, massively-parallel platforms, and are thus fundamentally ill-suited to scale to peta- or exa-scale computer architectures. Conversely, software that is highly scalable is often comparatively slow for small- or medium-size jobs run on a modest number of processors. To take highly efficient codes and scale them to large numbers of processors, new paradigms are needed.

Our approach to this challenge is based on the idea of a molecular exciton model.[1,20,21] Within such a model, collective excited states of an aggregate are represented as superpositions of excitations localized on molecular sites. The wavefunction for such a state can be expressed as

$$|\Xi_I\rangle = \sum_{n}^{\text{sites}} \sum_{i}^{\text{states}} K_n^{Ii} |\Psi_n^i\rangle \prod_{m \neq |n} |\Psi_m\rangle \tag{3.1}$$

where $|\Psi_n^i\rangle$ represents an excited state of monomer n and $|\Psi_m\rangle$ is the ground-state wave function for monomer m. This *ansatz* is quite flexible: additional excited states i can be included to increase the variational flexibility of the basis,[1] and the basis can be further expanded to include charge-transfer excitons (in which an electron is transferred between monomers) or multi-exciton states in which several molecular sites are excited simultaneously. The coefficients K_n^{Ii} are determined by diagonalizing the Hamiltonian in the exciton-site basis.

Historically, matrix elements within the exciton framework are often approximated by taking the diagonal elements to be some estimates of the site energies and off-diagonal elements that are computed within a transition-dipole approximation. More

recently, off-diagonal elements have been computed by numerical evaluation of the Coulomb integral between transition densities on different sites,[24,25,57] although this neglects exchange coupling. Our approach[1] is based on a fully *ab initio* realization of the *ansatz* in Eq. (3.1), in which basis states are constructed from independent configuration interaction-singles (CIS) calculations on individual monomers. The method is embarrassingly parallelizable, since calculation of monomer basis states and coupling matrix elements can be distributed with near-unit parallel efficiency. As such, this model significantly outperforms parallel implementations of traditional single-excitation methods on equivalent hardware, yet remains faithful to CIS excitation energies within $\sim$0.1 eV.[1]

Despite this favorable performance and parallel scalability, the cost to evaluate each individual matrix element scales as the fourth power of the overall size of the aggregate, as a result of the "corresponding orbitals" transformation[32] that is necessary to cope with the fact that orbitals on different monomers are not orthogonal.[1] In this work, we introduce a charge embedding scheme that dramatically reduces the formal scaling and drastically increases performance, while maintaining the accuracy and simplicity of the original approach. The efficiency of the new implementation enables us to treat system sizes well beyond the reach of traditional methods, with only modest hardware requirements.

3.2 Theory

3.2.1 Exciton Model

Basis states in our model are constructed in the form of Eq. (3.1) from direct products of configuration state functions (CSFs) computed for each isolated monomer. The ground states of fragments $A, B, C, \ldots, F$ are described by a single Hartree-Fock (HF) determinant, Φ_A. Excited states are described at the CIS level, as linear combinations of singly-excited determinants Φ_A^{ia}:

$$|\Psi_A^*\rangle = \sum_{ia} C^{ia} |\Phi_A^{ia}\rangle \ . \tag{3.2}$$

We use $i, j, k, \ldots$ and $a, b, c, \ldots$ to index occupied and virtual molecular spin-orbitals, respectively. To construct the exciton Hamiltonian, we need to evaluate matrix elements such as

$$\langle \Psi_A^* \Psi_B | \hat{H} | \Psi_A \Psi_B^* \rangle = \sum_{ia\sigma} \sum_{kb\tau} C_\sigma^{ia} C_\tau^{kb} \langle \Phi_A^{ia} \Phi_B | \hat{H} | \Phi_A \Phi_B^{kb} \rangle \ . \tag{3.3}$$

Orbitals on different sites are not orthogonal, hence Schrödinger's equation has the form of a generalized eigenvalue equation and we must also compute overlap integrals such as

$$\langle \Psi_A^* \Psi_B | \Psi_A \Psi_B^* \rangle = \sum_{ia\sigma} \sum_{kb\tau} C_\sigma^{ia} C_\tau^{kb} \langle \Phi_A^{ia} \Phi_B | \Phi_A \Phi_B^{kb} \rangle \ . \tag{3.4}$$

In these equations, we have introduced spin indices σ and τ in constructing CSFs from the monomer CIS calculations, as described in Ref. 1

Matrix elements in Eqs. (3.3) and (3.4) are computed exactly, including full Coulomb and exchange coupling, using the generalized Slater-Condon rules[33] that

can be derived following application of the corresponding orbitals transformation.[32] To reduce the number of terms in Eqs. (3.3) and (3.4), we transform the individual monomer excited states into the basis of natural transition orbitals[29] (NTOs, which are equivalent to CIS natural orbitals[58]). Coefficients can then be discarded based on a controllable, occupation-number threshold, and this procedure generally results in no more than a few significant coefficients per monomer. For systems comprised of polar monomers, the accuracy can be improved if the individual monomer ground-state orbitals are computed using the "explicit polarization" (XPol) procedure,[38] a variational, self-consistent charge embedding scheme. Our group has previously reported an implementation of XPol using "ChElPG" atomic charges derived from the electrostatic potential,[39,40] which are stable in large basis sets.

3.2.2 Charge Embedding Scheme

For brevity, the matrix elements in Eqs. (3.3) and (3.4) are given for the dimer AB, but in fact the basis states are direct products over all monomers, *e.g.*, $|\Psi_A^* \Psi_B \Psi_C \cdots \Psi_F\rangle$. Such a treatment is, in principle, required for *exact* Coulomb and exchange coupling. As a result of the corresponding orbitals transformation, the rate-limiting step in the calculation of any individual matrix element is the calculation of two-electron integrals for the entire system and their digestion with generalized density matrices for a particular monomer.[1] However, because the exchange interaction is short-ranged and the Coulomb interaction can be approximated via charge embedding, we propose here to retain the direct product *ansatz* but to simplify the evaluation of the matrix elements by partitioning the electronic coordinates in such a way as to distinguish

significant and insignificant inter-fragment interactions:

$$\begin{aligned}
&\left\langle \Psi_A^* \Psi_B \Psi_C \Psi_D \middle| \hat{H} \middle| \Psi_A \Psi_B^* \Psi_C \Psi_D \right\rangle \\
&\quad \approx \left\langle \Psi_A^* \Psi_B \middle| \left\langle \Psi_C \middle| \left\langle \Psi_D \middle| \hat{H}_{AB} + \hat{V}_{\mathrm{QM}} \right. \right. \right. \\
&\qquad + \hat{H}_C + \hat{H}_D + \hat{V}'_{\mathrm{MM}} \middle| \Psi_A \Psi_B^* \right\rangle \middle| \Psi_C \right\rangle \middle| \Psi_D \right\rangle .
\end{aligned} \tag{3.5}$$

Such partition divides the system into two regions, for which we adopt the terminology of "QM" and "MM". Coulomb and exchange interactions for all electrons in the significant (QM) region are treated exactly and inter-fragment interactions with electrons in the insignificant (MM) region are approximated as point charges. All *intra*-fragment interactions are described at the Hartree-Fock level.

Neglecting inter-fragment orbital overlap within the MM region, we can evaluate Eq. (3.5) as

$$\begin{aligned}
&\left\langle \Psi_A^* \Psi_B \Psi_C \Psi_D \middle| \hat{H} \middle| \Psi_A \Psi_B^* \Psi_C \Psi_D \right\rangle \\
&\quad \approx \left\langle \Psi_A^* \Psi_B \middle| \hat{H}_{AB} + \hat{V}_{QM} \middle| \Psi_A \Psi_B^* \right\rangle \\
&\qquad + (E_C + E_D + V'_{MM}) \left\langle \Psi_A^* \Psi_B \middle| \Psi_A \Psi_B^* \right\rangle ,
\end{aligned} \tag{3.6}$$

where E_C and E_D are the ground-state Hartree-Fock energies for the isolated fragments C and D. The operator

$$\hat{V}_{\mathrm{QM}} = \sum_{I \in \mathrm{MM}} \sum_{i \in \mathrm{QM}} \frac{q_I}{|\mathbf{R}_I - \mathbf{r}_i|} \tag{3.7}$$

describes the interaction between the QM and MM regions. Matrix elements of $\hat{V}_{\mathrm{QM}}$ are evaluated analogously to those for the core (one-electron) Hamiltonian; see

Eq. (12) of Ref. 1. The quantity

$$V'_{\mathrm{MM}} = \frac{1}{2} \sum_{I \in \mathrm{MM}} \sum_{J \in \mathrm{MM}}{}' \frac{q_I q_J}{|\mathbf{R}_I - \mathbf{R}_J|} + \sum_{I \in \mathrm{QM}} \sum_{J \in \mathrm{MM}} \frac{Z_I q_J}{|\mathbf{R}_I - \mathbf{R}_J|} + \sum_{I \in \mathrm{QM}} \sum_{J \in \mathrm{QM}} \frac{Z_I Z_J}{|\mathbf{R}_I - \mathbf{R}_J|} \,. \tag{3.8}$$

describes the self-interaction of the point charges in the MM region, with the primed summation restricted to fragments $J \neq I$.

There is some flexibility in how the system is partitioned. It is natural to include in the QM region those monomers that are excited in either the bra or the ket, as we have done with monomers A and B in Eqs. (3.5) and (3.6), but other nearby monomers might need to be included in the QM region in order to capture exchange effects. have implemented the charge-embedding scheme in a dynamic way so that fragments within a user-definable distance threshold from any excited fragments are automatically included in the QM region. We will investigate the accuracy of the method as a function of this threshold.

3.3 Results

Results for the lowest singlet and triplet excited states of small water clusters are presented in Fig. 3.1, and for several geometries of a $(H_2O)_{117}$ cluster in Fig. 3.2. Both sets of calculations use XPol self-consistent embedding for the monomer calculations, which adds minimal extra cost but was shown to be important in previous work, specifically in the case of water clusters where strong hydrogen-bonding interactions

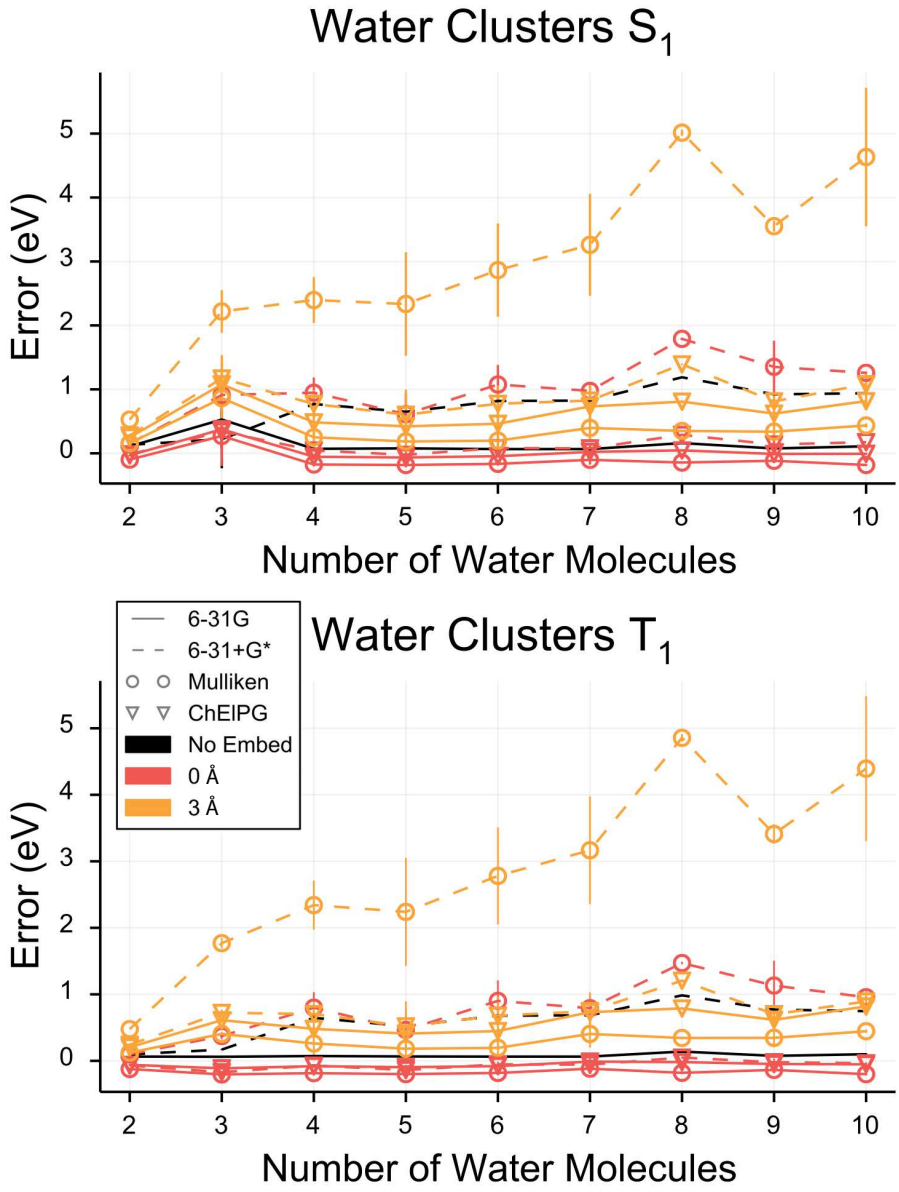

Figure 3.1: Mean unsigned errors in excitation energies, relative to supersystem CIS results, for various water cluster isomers. (Vertical lines represent the standard deviation.) Results without embedding correspond to the original *ab initio* exciton model of Ref. 1, and the "0 Å" threshold means that only the excited monomers are included in the QM region. All of the exciton calculations use XPol monomer wave functions and one CIS excited state per monomer. Cluster geometries are taken from Ref. 2.

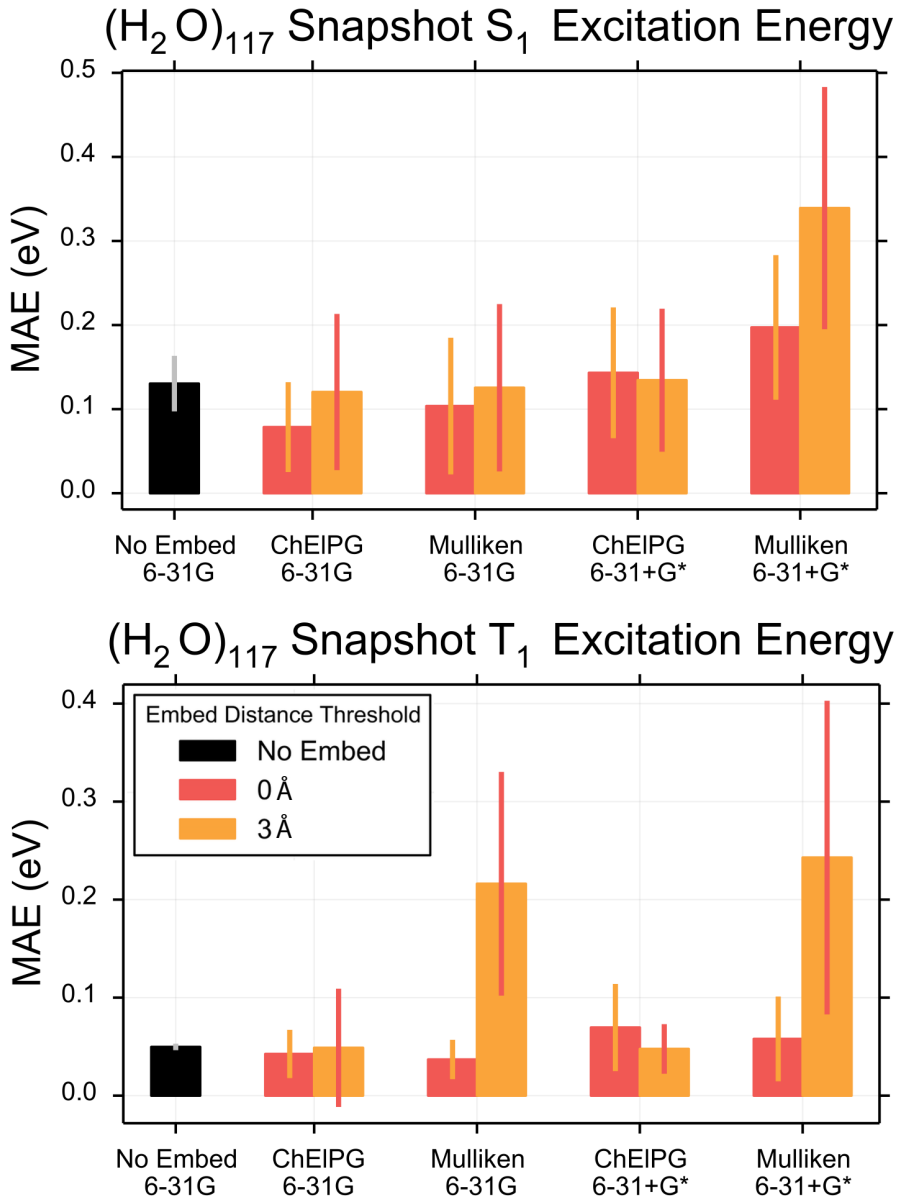

Figure 3.2: Mean unsigned errors in excitation energies, relative to supersystem CIS results, for five snapshots extracted from a liquid water simulation. (Vertical lines represent the standard deviation.) Results without embedding correspond to the original *ab initio* exciton model of Ref. 1, and the "0 Å" threshold means that only the excited monomers are included in the QM region. All of the exciton calculations use XPol monomer wave functions and one CIS excited state per monomer.

may significantly deform the H_2O molecular orbitals.[1] We examine the use of both Mulliken and ChElPG embedding charges. It is immediately clear from these results that the use of Mulliken charges in the 6-31+G* basis set leads to significantly larger errors as compared to other approaches, which is not surprising given the generally unreliable behavior of Mulliken charges in the presence of diffuse functions. Apart from this anticipated outlier, however, all of the errors are much smaller, and results using a "0 Å" embedding threshold (meaning that only those monomers that are excited in the bra or the ket are included in the QM region) generally lie within a few tenths of an eV from supersystem CIS excitation energies. Results for $(H_2O)_{117}$ (Fig. 3.2) are even better, with errors $\lesssim 0.1$ eV when ChElPG embedding charges are used.

Results using a 3 Å embedding threshold are reasonably close to the 0 Å results, and also close to results from the original model in which all monomers are described at the QM level. Note that a non-zero distance threshold does introduce a degree of inconsistency, however, especially for water clusters, because the number of QM monomers varies from one calculation to the next. In matrix elements of the form $\langle \Psi_A^* \Psi_B \Psi_C \cdots | \hat{H} | \Psi_A \Psi_B^* \Psi_C \cdots \; rangle$, the two excited monomers A and B may not be spatially proximal, thus in the case of $(H_2O)_{117}$ a 3 Å cutoff around each of A and B results in anywhere from 20 H_2O molecules in the QM partition (when A and B are nearby) up to 50 QM H_2O molecules (when they are not). This added expense and inconsistency seems unjustified based on the accuracy of the 0 Å results. The latter calculations run up to 6 times faster than full supersystem CIS calculations,

when both calculations are parallelized over a single, 20-core node using Q-Chem v. 4.3.1.[34] We will use the 0 Å threshold exclusively in what follows.

We next consider results for various organic chromophores, which are perhaps more realistic target systems for the exciton model. Systems examined here include tetracene, which has been widely studied in the context of singlet fission;[59–61] naphthalene diimide (NDI), which self-assembles into a nanotube with potentially interesting excited-state dynamics;[7,8] and guanine-cytosine (G-C) base pairs, since exciton models have long been employed to understand DNA photophysics.[62–65] In the latter system, we find that a judicious definition of the fragments is paramount for accurate description of the delocalized states. Watson-Crick base pairs provide a better description of the T_1 state while π-stacked G-C pairs along the same strand prove to be a better choice for the S_1 state. Results in Table 3.1 show that the charge embedding scheme performs quite well, with errors relative to supersystem calculations of 0.1–0.2 eV for all systems. This level of error is consistent with that obtained in our previous version of the model, in which all monomers were described at a QM level.

3.4 Parallel Computational Performance of the Charge Embedding Scheme

Regarding computational performance, even without charge embedding the *ab initio* exciton model exhibits better parallel scalability and outperforms traditional CIS calculations.[1] This is in spite of the fact that the cost of calculating each matrix element scales as $\mathcal{O}(N^x)$ with respect to the size of the entire supersystem, N, where

Table 3.1: Absolute errors[a] (in eV) in excitation energies for organic chromophores, using the *ab initio* exciton model.[b]

		6-31G		6-31+G*	
	F	None	ChElPG	None	ChElPG
			$(\mathrm{NDI})_F$		
T_1	2	0.14	0.14	0.14	0.13
	4	0.14	0.15	0.14	0.13
S_1	2	0.12	0.12	0.12	0.12
	4	0.17	0.17	0.16	0.11
			$(\mathrm{Tetracene})_F$		
T_1	2	0.16	0.16	0.16	0.16
	4	0.15	0.15	0.15	0.16
S_1	2	0.15	0.10	0.15	0.16
	4	0.19	0.18	0.19	0.20
			$(\mathrm{Guanine\text{-}Cytosine})_F$[c]		
T_1[d]	2	0.18	0.14	0.07	0.09
	4	0.13	0.18	0.08	0.13
S_1[e]	2	0.11	0.00	0.03	0.10
	4	0.18	0.08	0.24	0.07

[a]Relative to supersystem CIS with the same basis set. [b]Using an 85% NTO threshold. [c]Using XPol monomer wave functions. [d]Watson-Crick base pairs used as exciton sites. [e]π-stacked base pairs used as exciton sites.

the exponent x reflects the cost of computing electron repulsion integrals. (The oft-quoted value[66] $x = 4$ is correct for small molecules, but trivial integral screening will reduce this to $x = 2$ even for medium-size systems.) Charge embedding reduces the scaling of exciton calculations to $\mathcal{O}(F^2 \times n_{\text{pair}}^x)$ where n_{pair} represents the size of a pair of monomers. Parallel efficiency remains excellent, as the matrix elements can be computed entirely independently of one another and are thus distributable without communication or cache coherency overhead. We have implemented the method in Q-Chem using distributed-memory MPI parallelization that allows scaling across multiple nodes, and with enough cores the time-to-solution can be made to scale as $\mathcal{O}(n_{pair}^x)$ regardless of the size of the supersystem.

In Fig. 3.3 we compare the parallel scaling performance to that of a multi-threaded implementation of CIS, for G-C base stacks. (The speedup is defined as the ratio of the wall time required for a supersystem CIS calculation to that required for the exciton calculation, when both calculations are run on the same number of processors.) In previous work,[1] we compared parallel efficiency versus NWChem,[48] due to the good scalability of that code. However, Q-Chem's multi-threaded CIS code is much faster than NWChem's on a small numbers of processors, so the performance of the exciton model is evaluated here versus Q-Chem. The comparison is limited to a single node (20 processors), since Q-Chem's CIS implementation does not scale well across multiple nodes. This means that even greater speedups are possible for the largest systems in Fig. 3.3, since the exciton model does not suffer any performance degradation when extended beyond a single node. Nevertheless, we still observe speedups

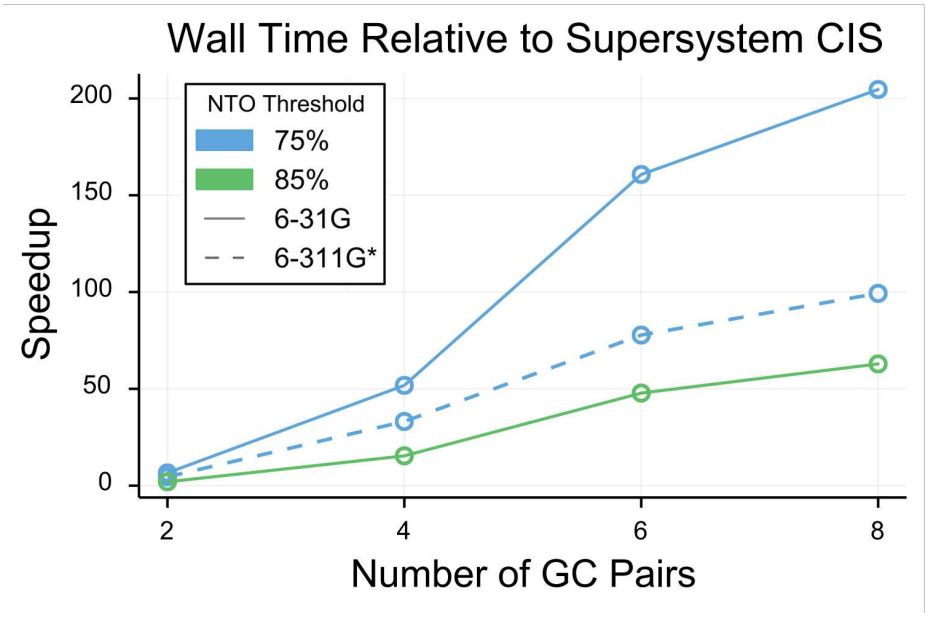

Figure 3.3: Parallel performance of the exciton model relative to a multi-threaded (OpenMP) version of supersystem CIS, as implemented in Q-Chem v. 4.3.1. Calculations were run on $F(F-1)/2$ cores up to $F = 20$, which is the number of cores on a node.

Table 3.2: Resources required for an exciton calculation[a] on different $(\mathrm{NDI})_F$ nanotube substructures.

$F =$	2	4	9	42	156
No. basis functions	876	1,752	3,942	14,700	54,600
No. processors	3	10	20	150	440

[a]In less than one week of wall time.

of up to 200×, using an NTO threshold of 75% that was sufficient to achieve ∼0.2 eV accuracy in previous calculations.[1] Note that the both NTO threshold and the size of the atomic orbital basis set contribute only prefactors to the $\mathcal{O}(F^2 \times n_{\mathrm{pair}}^x)$ scaling, independent of the overall size of the system.

This scalability allows us to treat systems that would otherwise be intractable on commodity hardware and would instead require running a code like NWChem on thousands of processors (or more). As a demonstration, we have performed calculations on $(\mathrm{NDI})_F$ substructures of varying sizes taken from the nanotube structural model in Ref. 8. Table 3.2 shows the size of each system (in terms of the number of basis functions) and the number of processors on which it was run; in each case, the calculation was complete in under one week. As shown in the table, our method can be applied to nanoscale systems with upwards of 50,000 basis functions on hardware that might readily be available in a laboratory cluster.

3.5 Excitation Energy Transfer in a Napthalene Diimide Nanotube

A uniquely valuable aspect of an exciton model is the unambiguous diabatic representation of localized excited states that is inherent in the exciton-site basis. Using operators in this basis, it is very straightforward to use a density matrix formalism to study excitation energy transfer in extended systems, and we have used the Redfield master equation[67–70] to investigate exciton dynamics in substructures of the NDI nanotube. In this approach, system-bath interactions are entirely described by a spectral density function $S(\omega)$, for which we use a temperature bath spectral density with an Ohmic form and a Lorentzian cutoff:

$$S(\omega) = \left(\frac{2\omega\lambda\Omega}{\omega^2 + \Omega^2} \right) n_{\mathrm{BE}}(\omega) \; . \tag{3.9}$$

The parameters λ and Ω are the reorganization energy and the characteristic bath cutoff frequency, respectively, and $n_{\mathrm{BE}}(\omega)$ is the Bose-Einstein distribution. The parameters were computed from excited-state geometry optimization and frequency calculations on a NDI monomer at the same level of theory that is used in the exciton calculations, CIS/6-31G*. (The values are $\lambda = 0.013$ a.u. and $\hbar\Omega = 0.015$ a.u.) Although the spectral density in Eq. (3.9) can sometimes average out potentially important details of the vibrational structure,[71] and Redfield theory itself has known shortcomings,[72] in the regime of weak electron-nuclear coupling this approach is a simple and computationally tractable way to probe ultrafast electronic processes and has provided insight in various contexts.[73–75]

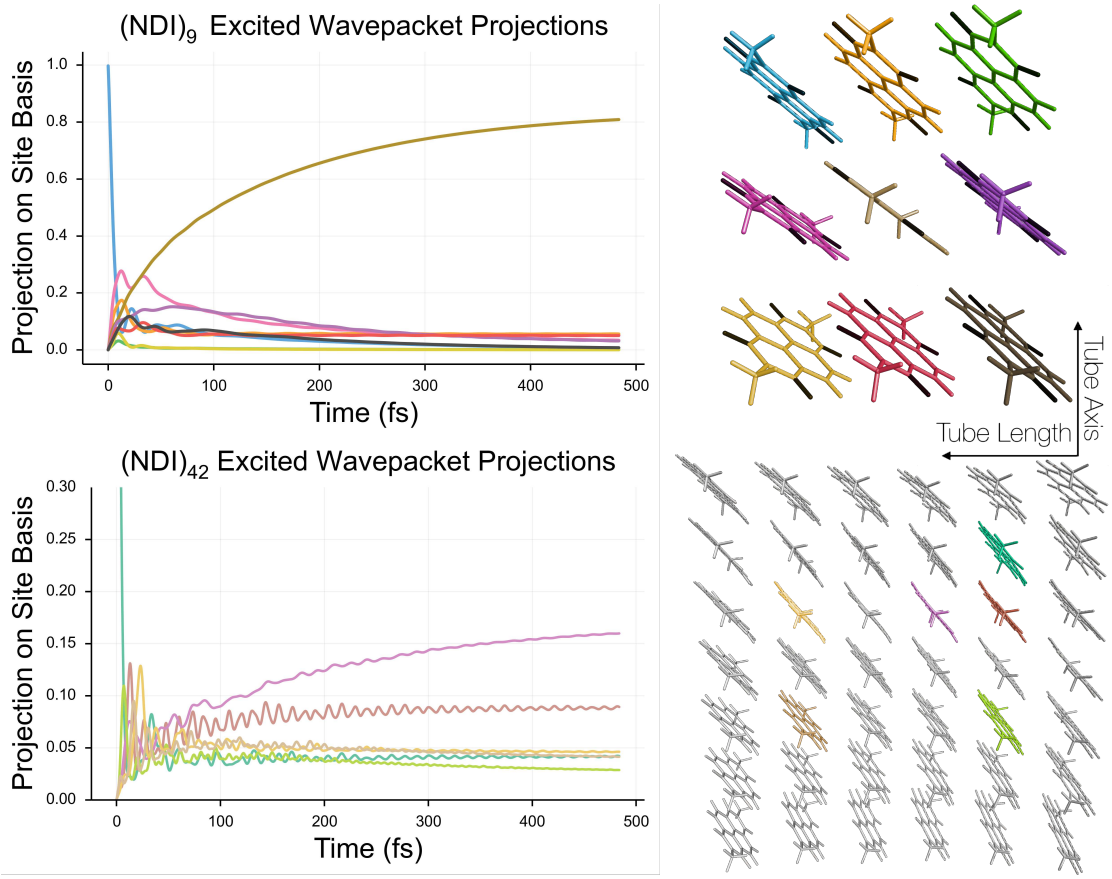

Figure 3.4: Redfield dynamics of 9- and 42-monomer substructures of an organic semiconductor nanotube. The initial wavepacket is localized on a single exciton-site basis state, and the plots on the left show the projections of the wavepacket onto various other basis states, which are color-coded according to the figures on the right.

Quantum dynamics calculations were performed on $(NDI)_9$ and $(NDI)_{42}$, starting from an initial wave packet corresponding to populating an excited state on a single NDI monomer. The density matrix was propagated in time (using the QuTip software[76]), and projections onto the significant exciton-site basis states are plotted in Fig. 3.4. Following a period of < 50 fs in which the initial state delocalizes over multiple monomers, the dynamics in both NDI substructures are dominated by a 100–500 fs time period during which the excitation re-localizes on a different monomer. This is primarily the result of static disorder; excitation energy flows downhill to a monomer that is lower in energy. (Heterogeneity in the site energies is easily confirmed by examining the diagonal elements of the exciton Hamiltonian.) These observations are generally in agreement with results presented in Ref. 8 where an incoherent hopping model based on pairwise couplings and Fermi's Golden Rule predicts energy-transfer time scales ranging from 0.2–1.0 ps. One point that is specifically raised in Ref. 8 is the importance of atomistic resolution in the electronic structure studies, since even small variations in the site energies of an otherwise homogenous system are enough to significantly modulate the flow of energy.

We selected $(NDI)_9$ for this comparison because it was the model system used in time-dependent density functional theory (TDDFT) calculations in Ref. 8, where the primary limitation to the system size is a serious memory bottleneck due to the large density of states. Those calculations were performed at the TDDFT/3-21G* level, and to locate the lowest-energy bright state of $(NDI)_9$ at the TDDFT/6-31+G* level we estimate that ≈ 30 Gb would be required to store the subspace vectors for the

Davidson iterations. No such bottleneck exists in the exciton model.

In view of this, another crucial message from these calculations is the significant, qualitative difference between the exciton dynamics in $(NDI)_9$ versus $(NDI)_{42}$. The former exhibits rapid dephasing, with coherent oscillations in the site populations only within the first 100 fs, whereas in the larger model, the population transfer is coherent for nearly 500 fs. This is understandable, as the greater number and range of couplings in the larger system provides more instances of accidental degeneracies in the site energies, whereas the 9-unit model is much more susceptible to "edge effects" in the distribution of energies and couplings. The distinct differences between these two simulations highlights the benefit of large-scale simulations, as coherence can significantly alter to the energy-transfer timescale. The results suggest that this nanotube, and similar systems, undergoes ultrafast coherent excitation energy transfer that can potentially be guided through strategic functionalization of the monomers. Our *ab initio* exciton model, in its more efficient formulation presented here, is well suited to investigate such processes.

3.6 Conclusions

In summary, we have significantly improved the performance of our *ab initio* exciton model, without sacrificing its accuracy or physically-motivated simplicity. Tests on water clusters as large as $(H_2O)_{117}$ indicate that only a minimum number of monomers need be treated quantum-mechanically in computing matrix elements of the exciton Hamiltonian, eliminating a key bottleneck in our original implementation

of the method. Accuracy of ∼0.1–0.2 eV with respect to supersystem CIS calculations is obtained, for these systems as well as for coupled organic chromophores such as tetracene and DNA nucleobases. The embarrassingly-parallelizable nature of the method, combined with the fact that the cost of each matrix element does not increase with (super)system size in our new formulation, allows us to treat systems that would be completely intractable with conventional approaches, using only commodity hardware. Preliminary studies of excitation energy transfer in substructures of an organic semiconductor nanotube demonstrate that large-scale simulations may suggest qualitatively different energy flow as compared to the smaller models that are the only tractable choices when applying conventional approaches.

Further extensions of the model are possible, and become more feasible due to the reduced cost of the implementation reported here. Inclusion of electron correlation effects in the monomer excited-state calculations will be crucial for obtaining accurate values for the on-site energies, for example, but should be feasible within a perturbative framework.[49,77] Because the model comes with a well-defined wave function for the collective excitation, molecular properties (such as transition moments) are straightforward to calculate. Such developments are currently underway in our group.

CHAPTER 4

Accelerating Integral Digestion with Graphics Processing Units

4.1 Introduction

The working equation for the ab-initio Frenkel Davydov Exciton Model (AIFDEM) is,

$$H_{AB} = \sum_{i \in A} \sum_{j \in B} t^i \, t^j \, \xi_\alpha^{ij} \, \xi_\beta^{ij} \, \Gamma^{ij} \; . \tag{4.1}$$

where,

$$\begin{aligned} \Gamma^{ij} = \left(\mathbf{G}_\alpha^{ij} + \mathbf{G}_\beta^{ij}\right) \cdot \mathbf{h} + \tfrac{1}{2}\mathbf{G}_\alpha^{ij} \cdot \mathbf{\Pi} \cdot \mathbf{G}_\alpha^{ij} \\ + \mathbf{G}_\beta^{ij} \cdot \mathbf{\Pi} \cdot \mathbf{G}_\beta^{ij} + \mathbf{G}_\alpha^{ij} \cdot \mathbf{\Pi}^\circ \cdot \mathbf{G}_\beta^{ij} \; . \end{aligned} \tag{4.2}$$

Here, $\mathbf{A} \cdot \mathbf{B} = \sum_{ij} A_{ij} \times B_{ij}$, where the matrices $\mathbf{A}$ and or $\mathbf{B}$ is assumed to be symmetric. The letters i and j index terms of the natural transition orbital (NTO) expansion of the fragments which contribute to the generalized density matrices, $\mathbf{G}$ and α, β index their spin. The matrix $\mathbf{h}$ is the core Hamiltonian, t are the fragment configuration interaction coefficients, and ζ ensure consistent normalization and phase; these are all explained in more detail along with a full a derivation of the method in Chapter 5. Our concern, at this point, is with the two electron part. Above, the

Figure 4.1: Call graph diagrams for an a) AIFDEM and b) CIS calculation, both within Q-Chem. The diagrams outline all the major routines called by the program during the course of the calculation. The size of the boxes in the diagrams indicates the relative amount of wall time spent in the indicated routine. The routines that perform integral digestion are labeled.

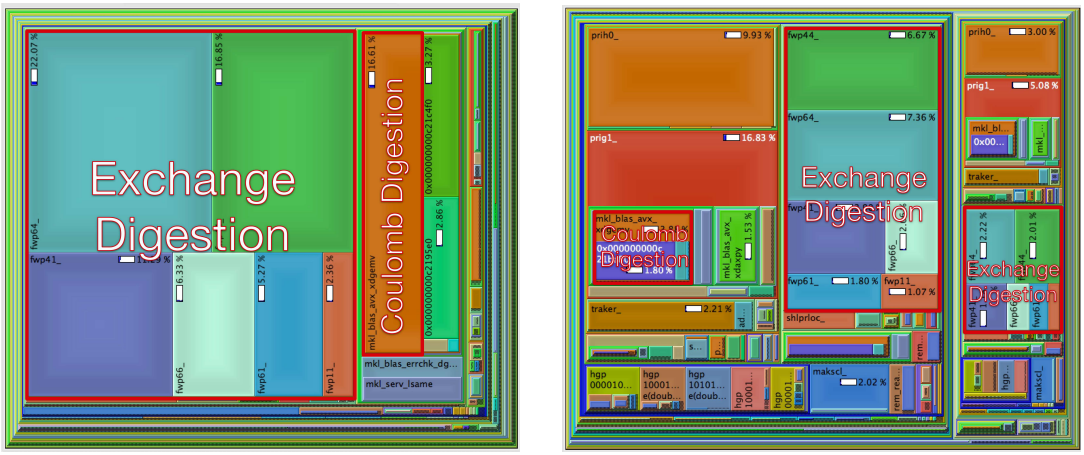

a) AIFDEM b) CIS

four-index tensor of antisymmetrized electron repulsion integrals is indicated by $\mathbf{\Pi}$ where a superscripted circle indicates Coulomb integrals only. Generally, the dimension of the ij subspace is on the order of dozens to several hundred densities and it is the contraction of the integrals with the many densities that is the overwhelming computational bottleneck of the AIFDEM. This is also the case with other methods, such as CIS and TDA-TD-DFT, in certain situations. A call graph diagram, shown in Fig. 4.1 demonstrates graphically the proportion of an AIFDEM calculation taken up by the digestion step; this is on the order of 80% compared to approximately 30% for traditional a CIS job.

The digestion procedure in question can be written as the contraction of a 4-index

tensor, the two-electron integrals, with a three-index tensor, the set of generalized densities, to form another three-index tensor of Fock-like matrices,

$$\tilde{F}^I_{\mu\nu} = \sum_{\lambda\sigma} (\mu\nu||\lambda\sigma)\, G^I_{\lambda\sigma}. \tag{4.3}$$

Here, the ij indices of the generalized density matrices have been replaced with the compound index, I and $\mu\nu\lambda\sigma$ index atomic orbital (AO) basis functions. Essentially the same digestion procedure is undertaken in traditional CIS and TDDFT calculations as well where the generalized density matrices are replaced with trial transition density matrices in the AO basis and the I subspace are the excited roots sought. In CIS/TDDFT The contraction is performed at every Davidson iteration and the dimension of the I subspace is the number of unconverged roots.

An analogous digestion step is performed during SCF calculations as well, with the simplifications due to the symmetry of the SCF density matrix. However, in the SCF case only a single density needs to be digested per SCF cycle, making the digestion far less demanding and a task for which typical integral libraries are well optimized. Typically, integrals are generated and immediately digested in batches that are small enough to fit in CPU caches. When the dimension of the density subspace exceeds a certain point, these quantities can no longer fit in cache and the requisite trips to main memory severely impact the performance. The bright side is that a large degree of data parallelism becomes apparent when many densities are present, essentially the same operation is performed for each density and the integrals can be reused. This general concept is the foundation of vector processing operations, often

termed single instruction multiple data (SIMD), for which specialized instructions and execution units are present in modern processor architectures. These types of operations are abundantly common in 3D graphics rendering therefore, graphics processing units (GPUs) are designed around this type of work; although typical GPUs are designed such that parallel operations execute in their own register spaces so a better label for these instructions is single instruction multiple thread (SIMT). With these considerations in mind, it is expected that a GPU implementation of Eq. 4.3 should potentially accelerate AIFDEM calculations by a significant degree.

4.2 Algorithm Design

4.2.1 Double Buffered Heterogenous Algorithm

Our GPU implementation of Eq. 4.3 is actually a heterogenous CPU+GPU implementation, integral generation is executed on the CPU and they are digested by the GPU. In some ways, this approach plays to the strengths of each machine: integral generation requires branching recursion relations and generates many shared intermediate quantities; digestion entails straightforward, if copious, fused-multiply-add operations. However, this strategy runs directly up against what is perhaps the biggest challenge in GPU algorithm design, that is the transfer of data from CPU memory to GPU memory via the high-latency PCIE bus, potentially incurring significant performance penalties. Recent versions of NVIDIA's CUDA platform have introduced capabilities for concurrent data transfer and compute on GPU devices as

well as APIs that allow for asynchronous calls from the perspective of the CPU. Utilizing these capabilities, our algorithm is implemented using a double buffer strategy that hides the PCIE transfer latency by executing digestion on the GPU, data transfer over the bus, and integral generation on the CPU concurrently, avoiding stalls while one part of the machine waits for data. The approach is outlined schematically in Fig. 4.2 and compared to a traditional CPU digestion algorithm.

Figure 4.2: Schematic of the double buffer scheme used in our heterogenous CPU+GPU approach compared to a traditional CPU digestion implementation

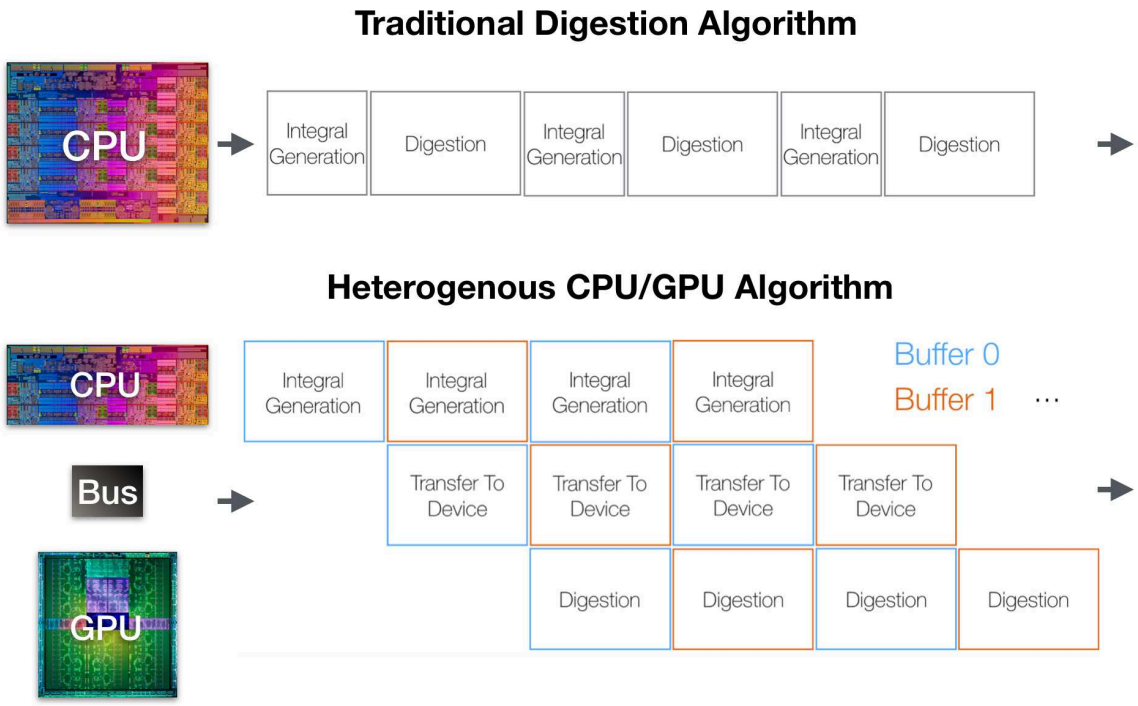

The scheme involves pre-organizing integrals into batches that fit in available

device memory and makes use of two instances of a buffer data structure with host and device components. At step N, the CPU generates the Nth batch batch of integrals and stores them in host buffer 0, a synchronization call here will block the CPU until device buffer 0 is available and then the integrals are transferred asynchronously to the device so the CPU can immediately begin to generate batch $N+1$ in host buffer 1. Meanwhile, the GPU had been digesting batch $N-2$ while batch $N-1$ had been transferring to device buffer 1 so these integrals are now available for the GPU to digest when batch $N-2$ is complete. By the time batch $N-1$ is digested, the integrals for batch N are available on the GPU and the cycle continues until all batches are digested. While we have found that, in practice there are occasionally bubbles in this pipeline, typically delays due to high angular momentum integral generation cause the GPU to stall, the majority of the work overlaps nicely on our testbed system and the scheme is quite performant.

4.2.2 Kernel Design

The heart of any GPU algorithm is the computational kernels that run on the device and the challenge is to map the particular problem to its hardware layout. Due to the symmetry of the two-electron integrals, we can avoid computing all of the integrals by transposing the tensor during digestion to include all of the contributions to the coulomb and exchange matrices. The necessary transpositions are,

$$J^I_{\mu\nu} = \sum_{\lambda\sigma} (\mu\nu|\lambda\sigma)\, P^I_{\lambda\sigma} \tag{4.4a}$$

$$J^I_{\mu\nu} = \sum_{\lambda\sigma} (\lambda\sigma|\mu\nu)\, P^I_{\lambda\sigma} \tag{4.4b}$$

$$K^I_{\mu\nu} = \sum_{\lambda\sigma} (\mu\lambda|\nu\sigma)\, P^I_{\lambda\sigma} \tag{4.4c}$$

$$K^I_{\mu\nu} = \sum_{\lambda\sigma} (\lambda\mu|\nu\sigma)\, P^I_{\lambda\sigma} \tag{4.4d}$$

$$K^I_{\mu\nu} = \sum_{\lambda\sigma} (\mu\lambda|\sigma\nu)\, P^I_{\lambda\sigma} \tag{4.4e}$$

$$K^I_{\mu\nu} = \sum_{\lambda\sigma} (\lambda\mu|\sigma\nu)\, P^I_{\lambda\sigma}. \tag{4.4f}$$

When asymmetric densities are utilized, as is the case for the AIFDEM and CIS/TDDFT, the following terms are also required.

$$K^I_{\nu\mu} = \sum_{\lambda\sigma} (\mu\lambda|\nu\sigma)\, P^I_{\sigma\lambda} \tag{4.5a}$$

$$K^I_{\nu\mu} = \sum_{\lambda\sigma} (\lambda\mu|\nu\sigma)\, P^I_{\sigma\lambda} \tag{4.5b}$$

$$K^I_{\nu\mu} = \sum_{\lambda\sigma} (\mu\lambda|\sigma\nu)\, P^I_{\sigma\lambda} \tag{4.5c}$$

$$K^I_{\nu\mu} = \sum_{\lambda\sigma} (\lambda\mu|\sigma\nu)\, P^I_{\sigma\lambda}. \tag{4.5d}$$

As is fairly common, the integrals are generated in blocks corresponding to shell quartets with the dimension of each block determined by the number of functions on each center, typically the angular momentum components. Rather than accumulate the entire tensor it is sensible to digest the integrals blockwise by quartet, leading to contraction operations with a finite number of possible dimensions. Our strategy was to write a single kernel and utilize C++ templates to generate specialized code for each quartet dimension and integral transposition, this can maximize opportunities for the compiler to make optimizations and simplifies the implementation as a new kernel can be implemented in single line of code. Tuning kernels by hand for every quartet and contraction could potentially result in better performance, but the sheer number of different parameters ensures each individual kernel only runs for a fraction of the total job time making specialized optimizations impractical.

The basic contraction kernel assigns a group of GPU threads to compute a J/K matrix contribution from a given integral quartet for a portion of the I subspace, each thread accumulates a single J/K matrix element. Integral quartets are presorted by dimension so all contractions for a given quartet class are launched simultaneously, these will run concurrently on the device. The kernel will initially load the current block of integrals and densities into fast level 2 cache, called shared memory in CUDA parlance. After contraction, the matrix elements are summed into the global J/K matrices in device memory using atomic add operations, provided by the CUDA API. We have found, in our case, the atomic operations are not a major bottleneck in our implementation, furthermore, they eliminate the need for temporary buffers

significantly reducing memory requirements.

4.3 Results

All of our benchmarks were run on a single node with 2× Intel Xeon E5-2680 v4 CPUs (28 total cores), 128 GB of main memory, and a NVIDIA Tesla P100 GPU with 16 GB of memory. We have tested our algorithm in a set of synthetic benchmarks against the equivalent CPU only integral routine in Q-Chem 5.0. For this test, densities are generated randomly in the AO basis set of the given test systems, the densities are asymmetric and restricted to a single spin. The results, shown in Fig. 4.3 demonstrate impressive speedups. The He_{100} test case demonstrates a 3 to 12.5 × speedup improvement over CPU only Q-Chem when going from 8 to 256 densities. This case represents an upper bound on performance because the dimension of the single quartet class that is present in this basis, $6 \times 6 \times 6 \times 6$, provides an optimal balance of memory and arithmetic operations for the kernel. For real systems, the GPU algorithm is already slightly faster than CPU-only Q-Chem at 8 densities and approximately twice as fast at 32 densities. For a pentacene molecule in the CC-PVDZ basis, the CPU+GPU algorithm is able to achieve up to a 4× speedup over Q-Chem when digesting 256 densities, note that this is not an uncommon number of densities to be digested in a typical AIFDEM calculation. A pentacene dimer in the same basis achieves approximately a 6× speedup, indicating that relative performance improves as the system size increases.

We have also tested real AIFDEM calculations with our CPU+GPU algorithm on

Figure 4.3: Synthetic benchmarks of the speedup offered by our CPU+GPU implementation relative to a CPU only digestion implementation. A set of n randomly generated density matrices are digested to build n Coulomb and n exchange matrices and n is plotted on the x-axis.

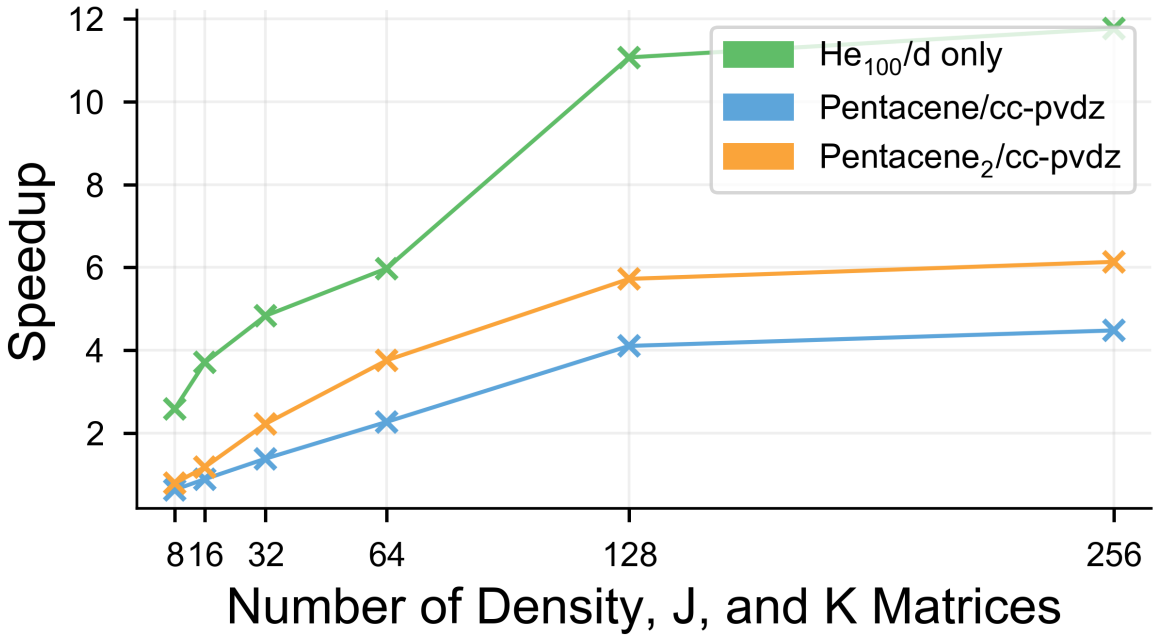

a pentacene dimer using multiple AO basis sets and NTO thresholds, their timings compared to CPU-only Q-Chem are given in Table 4.1. The NTO threshold represents an accuracy knob, of sorts, for the AIFDEM by setting the percentage of the norm of the fragment transition density matrices that is retained when truncating their excited wavefunctions in the NTO basis. The greater this percentage, the closer the AIFDEM excitation energy is to that of a supersystem calculation, however, the number of densities that are required for digestion in Eq. 4.1 grows approximately quadraticly, thus determining the cost of the calculation. We have found previously in

Chapter 2 that an 80% threshold is sufficient for acceptable accuracy. The number of densities for digestion that correspond to the given basis and threshold are also given, and at first glance, the timings might not seem to correlate with those in Fig. 4.3. For instance, a calculation with pentacene dimer in the CC-PVDZ basis set yields a 2.3× speedup relative to CPU-only Q-Chem, which while impressive, is not a 6× speedup one might expect for this system with 162 densities based on 4.3. This is because the AIFDEM requires integrals over spin-unrestricted densities, that is one for α and β spin (although the J matrix may be formed from the total density). Therefore, the effective number of densities digested is approximately twice the value given in Table 4.1 and CPU-only Q-Chem calculations, perhaps due to being dominated by overhead, does not increase in wall time to the same degree as the GPU algorithm when moving from a restricted to unrestricted case. Regardless, the GPU algorithm is still quite performant, yielding speedups near than 4× for the aug-CC-PVDZ test case, again indicating the value of this algorithm for larger systems.

4.4 Conclusions

Here, we have appealed to the data parallel nature of the operation and implemented an efficient heterogenous CPU+GPU algorithm for the digestion of 2-electron integrals with many density matrices. This is specifically targeted at speeding up AIFDEM calculations but there are other cases where this algorithm may be useful as well, specifically TDA-TDDFT/CIS calculations where high lying roots are sought. The GPU+CPU algorithm demonstrated a speedup of over 6×, relative to CPU-only

Table 4.1: Wall time for AIFDEM calculations of the singlet excited states for a pentacene dimer, CPU only Q-Chem is compared to the CPU+GPU digestion algorithm for several basis sets and NTO thresholds.

Basis Set	CC-PVD		aug-CC-PVDZ	
NTO Threshold[a]	75%	85%	75%	85%
No. of Densities[b]	162	648	200	648
	AIFDEM Time[c] (s)			
CPU-only	3462.05	13679.09	114865.81	365567.12
CPU + GPU	1533.38	5265.49	31659.87	97149.45
Speedup	2.26	2.60	3.63	3.76

[a] Percentage of the norm of the transition density matrix retained in the fragment state NTO truncations
[b] Representative; for a single diagonal matrix element
[c] Excluding fragment calculation time

Q-Chem in synthetic benchmarks on real systems. AIFDEM calculations demonstrate speedups on the order of 2-4 $\times$ due to the spin unrestricted densities; greater speedups are expected for larger systems and basis sets. We intend to take advantage of the speedups provided by this algorithm in our research group.

CHAPTER 5

Analytic derivative couplings and first-principles exciton/phonon coupling constants for an *ab initio* Frenkel-Davydov exciton model: Theory, implementation, and application to compute triplet exciton mobility parameters for crystalline tetracene

In chapter 2, an *ab initio* version of the Frenkel-Davydov exciton model for computing excited-state properties of molecular crystals and aggregates was introduced. Within this model, supersystem excited states are approximated as linear combinations of excitations localized on molecular sites and the electronic Hamiltonian is constructed and diagonalized in a direct-product basis of non-orthogonal configuration state functions computed for isolated fragments. In this chapter, analytic derivative couplings for this model are derived and implemented, including nuclear derivatives of the natural transition orbital and symmetric orthogonalization transformations that are part of the approximation. Nuclear derivatives of the exciton Hamiltonian's matrix elements, required in order to compute the nonadiabatic couplings, are equivalent to the "Holstein" and "Peierls" exciton/phonon couplings that are widely discussed in

the context of model Hamiltonians for energy and charge transport in organic photovoltaics. As an example, the couplings that modulate triplet exciton transport in crystalline tetracene are computed, these couplings are relevant in the context of carrier diffusion following singlet exciton fission.

5.1 Introduction

In a variety of important chemical systems the motion of nuclei can induce electronic transitions, which represents a breakdown of the Born-Oppenheimer approximation. This is well known in molecular photophysics and photochemistry,[78–81] including the photochemistry of biologically-important molecules,[82,83] leading to vibronic effects in molecular spectroscopy,[81,84] including the Jahn-Teller effect.[85] Nonadiabatic effects are also important in nanoscale systems where they influence charge transport in organic photovoltaics,[86] charge recombination in photo-excited nanoparticles,[87] and singlet fission in crystalline organic materials,[88] processes that are challenging to model using quantum chemistry due to the size of the systems involved.

For molecular crystals and aggregates, a promising approach is an *ab initio* version of the Frenkel-Davydov exciton model that we have recently introduced.[1,89,90] In keeping with the original ideas of Frenkel[20] and of Davydov,[21] the wave function for a (potentially) collective excitation is expanded in a basis consisting of direct products of monomer wave functions, one or more of which may be excited. However, unlike the early models (and even many recent ones, *e.g.*, Refs. 62–64,91), we do not make any sort of dipole-coupling, nearest-neighbor, frontier orbital, neglect-of-exchange,

or other approximations to the Hamiltonian for the full system. Exact Hartree-Fock Coulomb and exchange interactions are included, although a charge-embedding scheme for distant monomer units has been successfully employed to significantly reduce the cost.[89] Our *ab initio* Frenkel-Davydov exciton model (AIFDEM) reproduces supersystem excitation energies to within 0.1–0.2 eV for systems including DNA base pairs, crystalline acenes, aggregates of organic chromophores, and water clusters,[1,89] and we have demonstrated that supersystems containing the equivalent of more than 50,000 basis functions can be treated with modest hardware requirements.[1] The ability of this method to include a large number of monomers in the calculation allowed us to demonstrate that the signatures of a quantum coherence in excitation energy transfer may persist to longer time scales as compared to those in smaller models that are accessible to traditional quantum chemistry calculations.[90]

Here, we report the derivation and implementation of analytic derivative couplings for this *ab initio* Frenkel-Davydov exciton model (AIFDEM). Namely, this means the first-order derivative couplings

$$\mathbf{d}^{JK} = \langle \Psi_J | \hat{\boldsymbol{\nabla}} | \Psi_K \rangle \tag{5.1}$$

where Ψ_J and Ψ_K are adiabatic electronic states and $\hat{\boldsymbol{\nabla}}$ represents derivatives with respect to Cartesian coordinates of the nuclei. These quantities codify the coupling of electronic states due to nuclear motion and can be said to drive nonadiabatic transitions. If the states Ψ_I and Ψ_J are exact eigenstates of the electronic Hamiltonian,

$\hat{H}$, then it can be shown that

$$\mathbf{h}^{JK} = \left\langle \Psi_J \middle| \frac{\partial \hat{H}}{\partial \mathbf{x}} \middle| \Psi_K \right\rangle = (E_J - E_K)\, \mathbf{d}^{JK} \ . \tag{5.2}$$

The quantities $\mathbf{h}^{JK}$ are known as the nonadiabatic couplings, and they describe the topology around the conical intersections between adiabatic potential energy surfaces. Knowledge of $\mathbf{h}^{JK}$ facilitates the use of more efficient algorithms for locating minimum-energy crossing points along conical seems between adiabatic electronic states.[92–94] Although the nonadiabatic couplings could be computed numerically,[95] an analytic implementation will be both more efficient and more accurate. For example, our group's implementation of $\mathbf{h}^{IJ}$ at the level of configuration-interaction singles (CIS) and time-dependent density functional theory (TD-DFT) requires very little overhead on top of a CIS or TD-DFT gradient calculation.[94]

Some of the first derivations and computer implementations of first-order derivative couplings were done by Lengsfield, Yarkony and co-workers for multi-reference CI and multi-reference self-consistent field models,[96–99] with new implementations as recently as 2016.[100] These quantities have also been derived at the level of equation-of-motion coupled-cluster theory.[101,102] Each of the aforementioned methods is potentially accurate yet expensive, so for extension to larger systems the quantities $\mathbf{h}^{JK}$ have also been implemented for CIS wave functions,[94,103–105] spin-flip CIS wave functions,[94] and their TD-DFT analogues.[94,105–108] Nevertheless, the scaling of these methods remains $\mathcal{O}(N^4)$ with respect to system size. Moreover, the two-electron integral contraction required at each Davidson iteration, as well as iterative solution of the coupled-perturbed equations,[109] are challenging to implement efficiently on modern,

massively-parallel computer architectures. Furthermore, the single-excitation *ansatz* is incapable of treating highly-correlated and multi-reference excited states, including the key multi-exciton intermediate in the singlet fission process,[110] which will be considered here.

By exploiting localized basis states and charge embedding, the AIFEM can, in principle, substantially reduce the cost of supersystem CIS or TD-DFT calculations in molecular crystals and aggregates, and can qualitatively describe the *inter*molecular electron correlation that defines the aforementioned multi-exciton state. Here, we derive and implement computational expressions for the quantities $\mathbf{H}^{[x]}_{JK} = \langle \Psi_J | \partial \hat{H} / \partial x | \Psi_K \rangle$, for wave functions Ψ_J and Ψ_K obtained from the AIFDEM. The derivation requires expressions for the derivative of the transformation from canonical molecular orbitals (MOs) to natural transition orbitals (NTOs),[29,30,111] as well as the derivative of Löwdin's symmetric orthogonalization procedure. Notably, the resulting expressions for the derivative couplings $\mathbf{H}^{[x]}_{JK}$ involve intermediate quantities that are equivalent to the so-called "Holstein" and "Peierls" coupling constants that are routinely discussed in the literature on organic photovoltaics. Indeed, we have recently used the AIFDEM formalism to compute these exciton/phonon couplings from first principles for the process of singlet fission in crystalline tetracene,[3] but the details of the implementation are provided here for the first time. Finally, we use this formalism to compute the exciton/phonon coupling constants that modulate triplet exciton mobility in crystalline tetracene, quantities that are also relevant in the context of singlet fission.

5.2 Theory

5.2.1 Notation

In what follows we adopt the matrix formalism of Maurice and Head-Gordon,[46] where boldface symbols represent vector-, matrix-, or tensor-valued quantities, and manipulations of these objects then refer to linear algebra operations: **AB** indicates matrix multiplication and

$$\mathbf{A} \cdot \mathbf{B} = \sum_{mn} A_{mn} B_{mn} \ . \tag{5.3}$$

If **A** and/or **B** is symmetric, which will be the case here, then $\mathbf{A} \cdot \mathbf{B} = \mathrm{tr}(\mathbf{AB})$.

Molecular monomer units, whose total number we shall denote as F, are indexed as $A, B, \ldots$. Indices $i, j, \ldots$ and $a, b, \ldots$ refer to occupied and virtual MOs, respectively; μ, ν refer to AOs; and τ is a spin index equal to α or β. The superscript $[x]$ will denote a partial derivative with respect to nuclear coordinate x. Atomic units are used throughout.

5.2.2 Model

An exciton model describes a collective excitation of the supersystem as a linear combination of excitations that are localized on molecular sites. Formally, the excited states are linear combinations of "exciton-site" basis states, each consisting of a direct product of monomer wave functions wherein one fragment is excited. The collective wave function for the Ith excited state is thus

$$\left|\Xi^I\right\rangle = \sum_n K_{In} \left|\Psi_A \Psi_B \cdots \Psi_n^* \cdots \Psi_F\right\rangle \ . \tag{5.4}$$

The exciton-site basis also includes a ground-state configuration and can be expanded with more states to fit the problem at hand, *e.g.*, by inclusion of charge-separated states $|\Psi_A^+\Psi_B^-\cdots\Psi_F\rangle$.[3] Coefficients K_{In} specify the contribution to eigenstate I of the supersystem that arises from the excitation on monomer n. These coefficients are determined by solving the generalized eigenvalue problem

$$\mathbf{HK}_I = \epsilon_I \mathbf{SK}_I \ . \tag{5.5}$$

The quantities **H** and **S** are the AIFDEM electronic Hamiltonian and overlap matrices, respectively. The latter arises because the exciton-site basis states are not generally orthogonal, although the supersystem eigenstates are, hence

$$\mathbf{K}_I^\dagger \mathbf{SK}_J = \delta_{IJ} \ . \tag{5.6}$$

We construct an exciton-site basis as direct products of configuration state functions (CSFs) computed for the isolated fragments. The ground-state basis function,

$$\big|\Psi_A\Psi_B\cdots\Psi_F\big\rangle = \big|\Phi_A\Phi_B\cdots\Phi_F\big\rangle \tag{5.7}$$

is a direct product of determinants Φ_M for each monomer. Excited states are described at the CIS or TDDFT level (for the latter, within the Tamm-Dancoff approximation[31]) as linear combinations of singly-substituted determinants:

$$\big|\Psi_M^*\big\rangle = \sum_{ia} T^{ia} \big|\Phi_M^{ia}\big\rangle \ . \tag{5.8}$$

The CI amplitude T^{ia} codifies an occupied $\rightarrow$ virtual ($i \rightarrow a$) transition.

A crucial aspect of our algorithm involves the transformation of the monomer MOs and amplitude matrix **T** into the basis of NTOs,[29,30,111] the latter of which are

equivalent to CIS or TDDFT natural orbitals.[58] (This equivalence is a unique feature of single-substitution wave functions, whose natural orbitals do not mix occupied and virtual orbitals; see Ref. 58.) This transformation reduces the number of terms in Eq. (5.8) to no more than the number of electrons on monomer M. Typically only a few of the transformed amplitudes are significant, and this number can be further truncated, in a controlled fashion, in order to preserve a certain threshold of the norm of the transition density. The NTOs comprise corresponding occupied/virtual pairs, hence the dual indices ia are redundant upon transformation and we can safely denote the CI amplitudes in the NTO bases as t^i rather than T^{ia}. A singly-excited, direct-product basis function can then be expressed as, *e.g.*,

$$\left|\Psi_A^* \Psi_B \cdots \Psi_F\right\rangle = \sum_{i \in A} t^i \left|\Phi_A^i \Phi_B \cdots \Phi_F\right\rangle , \tag{5.9}$$

bearing in mind that $|\Phi_A^i\rangle$ might need to be a CSF rather than a single Slater determinant, in order to obtain correct spin symmetry.[3]

5.2.3 Matrix elements

We require matrix elements of $\hat{H}$ in the basis of Eq. (5.9),

$$\begin{aligned} H_{AB} &= \left\langle \Psi_A^* \Psi_B \cdots \Psi_F \middle| \hat{H} \middle| \Psi_A \Psi_B^* \cdots \Psi_F \right\rangle \\ &= \sum_{i \in A} \sum_{j \in B} t^i \, t^j \left\langle \Phi_A^i \Phi_B \cdots \Phi_F \middle| \hat{H} \middle| \Phi_A \Phi_B^j \cdots \Phi_F \right\rangle , \end{aligned} \tag{5.10}$$

as well as the corresponding overlap matrix elements

$$\begin{aligned} S_{AB} &= \left\langle \Psi_A^* \Psi_B \cdots \Psi_F \middle| \Psi_A \Psi_B^* \cdots \Psi_F \right\rangle \\ &= \sum_{i \in A} \sum_{j \in B} t^i \, t^j \left\langle \Phi_A^i \Phi_B \cdots \Phi_F \middle| \Phi_A \Phi_B^j \cdots \Phi_F \right\rangle . \end{aligned} \tag{5.11}$$

For each of the terms in Eqs. (5.10) and (5.11), the bra and ket sets of orbitals are symmetrically orthogonalized among themselves and expanded in a common AO basis. The orbitals can then be represented as a matrix, for instance, the columns of $\mathbf{C}^i$ contain the coefficients for the orthogonalized orbitals of $|\Phi_A^i \Phi_B \cdots \Phi_F\rangle$. To compute the matrix elements between the two sets of orbitals, which are not orthogonal, we use the corresponding orbitals transformation and generalized Slater-Condon Rules.[32,33] Note that, the corresponding orbitals transformation requires the sets of orbitals of different spin to be treated individually. For simplicity, we will suppress spin indices on expressions treating a single spin and include a spin index when quantities involving both spin cases are needed.

We proceed by defining an AO overlap matrix $\mathbf{s}$,

$$s_{\mu\nu} = \langle \mu | \nu \rangle \ , \tag{5.12}$$

and then form the MO overlap matrix

$$\mathbf{S}^{ij} = (\mathbf{C}^i)^\dagger \, \mathbf{s} \, \mathbf{C}^j \tag{5.13}$$

using the bra and ket orbitals (of a single spin) from a given term in Eqs. (5.10) or (5.11). We then compute the singular value decomposition (SVD) of $\mathbf{S}^{ij}$,

$$\mathbf{S}^{ij} = \mathbf{U}^{ij} \boldsymbol{\lambda}^{ij} (\mathbf{V}^{ij})^\dagger \ , \tag{5.14}$$

which is defined by the diagonal matrix $\boldsymbol{\lambda}^{ij}$ of singular values and by the unitary matrices $\mathbf{U}^{ij}$ and $\mathbf{V}^{ij}$. A generalized density matrix

$$\mathbf{G}^{ij} = \mathbf{C}^j \mathbf{V}^{ij} \left(\boldsymbol{\lambda}^{ij} \right)^{-1} (\mathbf{U}^{ij})^\dagger (\mathbf{C}^i)^\dagger \tag{5.15}$$

can then be formed from the transformed MOs, and we introduce the quantity

$$\begin{aligned} \xi^{ij} &= \det[\mathbf{U}^{ij}(\mathbf{V}^{ij})^\dagger]\ \det(\boldsymbol{\lambda}^{ij}) \\ &= \Upsilon^{ij}\ \det(\boldsymbol{\lambda}^{ij})\ , \end{aligned} \tag{5.16}$$

which is a scalar that will ensure consistent norm and phase. [Note that since $\boldsymbol{\lambda}^{ij}$ is diagonal, $\det(\boldsymbol{\lambda}^{ij})$ is simply the product of the singular values.] This equation also serves to define $\Upsilon^{ij} = \det[\mathbf{U}^{ij}(\mathbf{V}^{ij})^\dagger]$.

Finally, we can write simple expressions for the overlap matrix elements,

$$S_{AB} = \sum_{i\in A}\sum_{j\in B} t^i\, t^j\, \xi^{ij}_\alpha\, \xi^{ij}_\beta\ , \tag{5.17}$$

and for the matrix elements of the Hamiltonian.

$$H_{AB} = \sum_{i\in A}\sum_{j\in B} t^i\, t^j\, \xi^{ij}_\alpha\, \xi^{ij}_\beta\, \Gamma^{ij}\ . \tag{5.18}$$

In the latter equation,

$$\begin{aligned} \Gamma^{ij} = \left(\mathbf{G}^{ij}_\alpha + \mathbf{G}^{ij}_\beta\right)\cdot\mathbf{h} + \tfrac{1}{2}\mathbf{G}^{ij}_\alpha\cdot\boldsymbol{\Pi}\cdot\mathbf{G}^{ij}_\alpha \\ + \mathbf{G}^{ij}_\beta\cdot\boldsymbol{\Pi}\cdot\mathbf{G}^{ij}_\beta + \mathbf{G}^{ij}_\alpha\cdot\boldsymbol{\Pi}^\circ\cdot\mathbf{G}^{ij}_\beta\ . \end{aligned} \tag{5.19}$$

The quantities ξ^{ij}_τ in Eqs. (5.17) and (5.18), and $\mathbf{G}^{ij}_\tau$ in Eq. (5.19), and are built from orbitals and transformation matrices having a spin index $\tau \in \{\alpha, \beta\}$. The quantity $\mathbf{h}$ in Eq. (5.19) is the core Hamiltonian, the four-index tensor $\boldsymbol{\Pi}$ contains antisymmetrized electron repulsion integrals

$$\Pi_{\mu\nu\lambda\sigma} = \langle\mu\nu||\lambda\sigma\rangle \tag{5.20}$$

and $\boldsymbol{\Pi}^\circ$ contains Coulomb integrals,

$$\Pi^\circ_{\mu\nu\lambda\sigma} = \langle\mu\nu|\lambda\sigma\rangle\ . \tag{5.21}$$

The latter arise in Eq. (5.19) because the exchange integrals vanish for the mixed-spin term.

In some cases, one or more of the singular values in $\boldsymbol{\lambda}^{ij}$ might approach zero, potentially leading to singularities in $\mathbf{G}^{ij}$. The algorithm is then modified to use special case co-density matrices such that the generalized Slater-Condon rules are recovered. Such a procedure is described in Ref. 112.

5.2.4 Derivative couplings

We seek to compute the first-order derivative couplings $\mathbf{d}^{JK}$ for the AIFDEM. As our model is essentially a form of non-orthogonal CI, we can adopt the general procedure that was derived by Lengsfield, Yarkony, and co-workers in the context of CI wave functions built upon a MCSCF reference state.[98] (The same approach has also been adapted to compute derivative couplings for CIS, TD-DFT, and their spin-flip analogues.[94,103]) Applying the chain rule to Eq. (5.4) and acting from the left with $\langle \Xi_J |$, we obtain

$$\langle \Xi_J | (\partial / \partial x) | \Xi_I \rangle = \mathbf{K}_J^\dagger \mathbf{S} \mathbf{K}_I^{[x]} + \mathbf{K}_J^\dagger \mathbf{S}^{R[x]} \mathbf{K}_I \; . \tag{5.22}$$

The quantity $\mathbf{S}^{R[x]}$ is the right overlap derivative matrix in the exciton-site basis,

$$S_{AB}^{R[x]} = \left\langle \Psi_A^* \Psi_B \cdots \Psi_F \middle| (\Psi_A \Psi_B^* \cdots \Psi_F)^{[x]} \right\rangle \; . \tag{5.23}$$

In order to eliminate the coefficient derivatives, $\mathbf{K}_I^{[x]}$, we differentiate the eigenvalue problem in Eq. (5.5) and left-multiply by $\mathbf{K}_J^\dagger$,

$$\begin{aligned} &\mathbf{K}_J^\dagger \mathbf{H}^{[x]} \mathbf{K}_I + \mathbf{K}_J^\dagger \mathbf{H} \mathbf{K}_I^{[x]} \\ &\qquad = \epsilon_I^{[x]} \mathbf{K}_J^\dagger \mathbf{S} \mathbf{K}_I + \epsilon_I \mathbf{K}_J^\dagger \mathbf{S}^{[x]} \mathbf{K}_I + \epsilon_I \mathbf{K}_J^\dagger \mathbf{S} \mathbf{K}_I^{[x]} \; . \end{aligned} \tag{5.24}$$

Here, $\mathbf{S}^{[x]}$ is the symmetric overlap matrix derivative in the exciton-site basis,

$$\begin{aligned} S_{AB}^{[x]} = &\left\langle (\Psi_A^* \Psi_B \cdots \Psi_F)^{[x]} \middle| \Psi_A \Psi_B^* \cdots \Psi_F \right\rangle \\ &+ \left\langle \Psi_A^* \Psi_B \cdots \Psi_F \middle| (\Psi_A \Psi_B^* \cdots \Psi_F)^{[x]} \right\rangle . \end{aligned} \tag{5.25}$$

By acting to the left with $\mathbf{H}$ in the second term on the left side of Eq. (5.24), and using the orthogonality of the eigenstates to eliminate the first term on the right, we obtain after some rearrangement

$$\mathbf{K}_J^\dagger \mathbf{S} \mathbf{K}_I^{[x]} = \frac{\mathbf{K}_J^\dagger \mathbf{H}^{[x]} \mathbf{K}_I - \epsilon_I \mathbf{K}_J^\dagger \mathbf{S}^{[x]} \mathbf{K}_I}{(\epsilon_I - \epsilon_J)} . \tag{5.26}$$

Finally, Eq. (5.26) can then be inserted into Eq. (5.22) to afford

$$\langle \Xi_J | (\partial/\partial x) | \Xi_I \rangle = \frac{\mathbf{K}_J^\dagger \mathbf{H}^{[x]} \mathbf{K}_I - \epsilon_I \mathbf{K}_J^\dagger \mathbf{S}^{[x]} \mathbf{K}_I}{(\epsilon_I - \epsilon_J)} + \mathbf{K}_J^\dagger \mathbf{S}^{R[x]} \mathbf{K}_I . \tag{5.27}$$

The term involving $\mathbf{K}_J^\dagger \mathbf{H}^{[x]} \mathbf{K}_I$ is the familiar Hellman-Feynman expression for derivative couplings and the other two terms are analogous to the Pulay terms that arise in SCF gradient theory using non-orthogonal basis functions. We identify the term $\mathbf{K}_J^\dagger \mathbf{H}^{[x]} \mathbf{K}_I$ in Eq. (5.27) as the nonadiabatic coupling, as established in the context of multireference CI and adopted by others.[94]

5.2.5 Derivatives of the matrix elements

To evaluate either the nonadiabatic coupling, the derivative coupling, or the energy gradient, we need $\mathbf{H}^{[x]}$, the derivative of the Hamiltonian in the exciton-site basis. Derivatives of the matrix elements are given by

$$H_{AB}^{[x]} = \sum_{i \in A} \sum_{j \in B} (t^i t^j \xi_\alpha^{ij} \xi_\beta^{ij})^{[x]} \Gamma^{ij} + t^i t^j \xi_\alpha^{ij} \xi_\beta^{ij} \Gamma^{ij[x]} \tag{5.28}$$

where

$$\begin{aligned}\Gamma^{ij[x]} = &\left(\mathbf{G}_\alpha^{ij} + \mathbf{G}_\beta^{ij}\right)^{[x]} \cdot \mathbf{h} + \left(\mathbf{G}_\alpha^{ij} + \mathbf{G}_\beta^{ij}\right) \cdot \mathbf{h}^{[x]} \\ &+ \mathbf{G}_\alpha^{ij[x]} \cdot \mathbf{\Pi} \cdot \mathbf{G}_\alpha^{ij} + \mathbf{G}_\beta^{ij[x]} \cdot \mathbf{\Pi} \cdot \mathbf{G}_\beta^{ij} \\ &+ \mathbf{G}_\alpha^{ij[x]} \cdot \mathbf{\Pi}^\circ \cdot \mathbf{G}_\beta^{ij} + \mathbf{G}_\alpha^{ij} \cdot \mathbf{\Pi}^\circ \cdot \mathbf{G}_\beta^{ij[x]} \\ &+ \tfrac{1}{2}\mathbf{G}_\alpha^{ij} \cdot \mathbf{\Pi}^{[x]} \cdot \mathbf{G}_\alpha^{ij} + \tfrac{1}{2}\mathbf{G}_\beta^{ij} \cdot \mathbf{\Pi}^{[x]} \cdot \mathbf{G}_\beta^{ij} \\ &+ \mathbf{G}_\alpha^{ij} \cdot \mathbf{\Pi}^{[x]\circ} \cdot \mathbf{G}_\beta^{ij} \; .\end{aligned} \tag{5.29}$$

The quantities $\mathbf{h}^{[x]}$ and $\mathbf{\Pi}^{[x]}$ are one- and two-electron integral derivatives, as required also to evaluate the SCF gradient, and $\mathbf{\Pi}^{[x]\circ}$ again indicates Coulomb integrals only. The expression in Eq. (5.29) takes advantage of symmetries such as

$$\mathbf{G}^{ij[x]} \cdot \mathbf{\Pi} \cdot \mathbf{G}^{ij} = \mathbf{G}^{ij} \cdot \mathbf{\Pi} \cdot \mathbf{G}^{ij[x]} \; . \tag{5.30}$$

However, when non-coincidences occur in the corresponding orbitals, necessitating the use of co-densities,[112] Eq. (5.30) is no longer valid and the terms on the left and the right must be computed explicitly.

The required derivatives of the generalized density matrices $\mathbf{G}^{ij[x]}$ can be obtained by direct differentiation of Eq. (5.15) with the result

$$\begin{aligned}\mathbf{G}^{ij[x]} = &\mathbf{C}^{j[x]}\mathbf{V}^{ij}\left(\boldsymbol{\lambda}^{ij}\right)^{-1}(\mathbf{U}^{ij})^\dagger(\mathbf{C}^i)^\dagger \\ &+ \mathbf{C}^j\mathbf{V}^{ij[x]}(\boldsymbol{\lambda}^{ij})^{-1}(\mathbf{U}^{ij})^\dagger(\mathbf{C}^i)^\dagger \\ &+ \mathbf{C}^j\mathbf{V}^{ij}[(\boldsymbol{\lambda}^{ij})^{-1}]^{[x]}(\mathbf{U}^{ij})^\dagger(\mathbf{C}^i)^\dagger \\ &+ \mathbf{C}^j\mathbf{V}^{ij}(\boldsymbol{\lambda}^{ij})^{-1}(\mathbf{U}^{ij[x]})^\dagger(\mathbf{C}^i)^\dagger \\ &+ \mathbf{C}^j\mathbf{V}^{ij}(\boldsymbol{\lambda}^{ij})^{-1}(\mathbf{U}^{ij})^\dagger(\mathbf{C}^{i[x]})^\dagger \; .\end{aligned} \tag{5.31}$$

Derivatives $\mathbf{U}^{ij[x]}$, $\mathbf{V}^{ij[x]}$, and $\boldsymbol{\lambda}^{ij[x]}$ of the matrices that define the SVD are required in Eq. (5.31), expressions for which can be found in the mathematics literature.[113,114]

(For completeness, the algorithm used to computed the SVD derivative is provided in Appendix A.) These expressions depend on the derivative of the MO overlap matrix as defined in Eq. (5.14), which is

$$\mathbf{S}^{ij[x]} = \mathbf{C}^{i[x]}\mathbf{s}\mathbf{C}^{j} + \mathbf{C}^{i}\mathbf{s}^{[x]}\mathbf{C}^{j} + \mathbf{C}^{i}\mathbf{s}\mathbf{C}^{j[x]} \,, \tag{5.32}$$

in which $\mathbf{s}^{[x]}$ is the derivative of the AO overlap matrix. Along with $\mathbf{h}^{[x]}$ and $\mathbf{\Pi}^{[x]}$, $\mathbf{s}^{[x]}$ is a standard quantity in SCF gradient theory.

Using these quantities, the derivative of the phase and normalization constants $\xi^{ij[x]}$ defined in Eq. (5.28) can be evaluated by differentiating Eq. (5.16). Using the definition of the derivative of a determinant, and taking advantage of the fact that $\mathbf{U}^{ij}$ and $\mathbf{V}^{ij}$ are unitary, one obtains

$$\begin{aligned}\xi^{ij[x]} = \Upsilon^{ij}\mathbf{U}^{ij\dagger}\mathbf{V}^{ij}\big(\mathbf{U}^{ij[x]}\mathbf{V}^{ij\dagger} + \mathbf{U}^{ij}\mathbf{V}^{ij[x]\dagger}\big)(\det\boldsymbol{\lambda}^{ij}) \\ + \Upsilon^{ij}(\det\boldsymbol{\lambda}^{ij})^{[x]} \,.\end{aligned} \tag{5.33}$$

The final derivative in this equation, $(\det\boldsymbol{\lambda}^{ij})^{[x]}$, is equal to the derivative of the product of the singular values. Expressions for derivatives of singular values are given in Refs. 113 and 114, and in Appendix A.

We now turn to the MO coefficient derivatives, $\mathbf{C}^{i[x]}$. Since the MOs are computed for isolated fragments their canonical derivatives are also computed at the fragment level by solving coupled-perturbed (CP)-SCF equations,[115] much like computing a SCF Hessian. Note that only fragment-level coupled-perturbed equations are ever required, and a the coefficient derivatives for a particular fragment vanish if the nuclear coordinate x does not belong to that fragment. It is possible that the Handy-Schaefer Z-vector technique[116] could be used to avoid solving CP-SCF equations

for each perturbation x, though this is potentially complicated by the fact that the orbital coefficients that appear in Eqs. (5.15) and (5.31) are not in the canonical basis, but rather have been transformed into the NTO basis and then symmetrically orthogonalized. (Derivatives of these transformations are derived below.) Moreover, the main bottleneck in AIFDEM derivative coupling calculations is contraction of integral derivatives with densities, so that the Z-vector technique would likely afford a modest reduction in the overall cost.

5.2.6 Derivatives of the NTO transformation

Derivatives of the matrices that define the transformation from canonical MOs to NTOs have not been reported previously but are fairly straightforward. NTOs are formed from separate unitary transformations of the occupied and the virtual MOs,

$$\bar{\mathbf{C}}_{\mathrm{O}} = \widetilde{\mathbf{C}}_{\mathrm{O}}\mathbf{O} \tag{5.34a}$$

$$\bar{\mathbf{C}}_{\mathrm{V}} = \widetilde{\mathbf{C}}_{\mathrm{V}}\mathbf{N}. \tag{5.34b}$$

Tildes indicate canonical MO coefficients and overbars denote NTO coefficients. For the AIFDEM, the NTO transformation is performed separately on each fragment. The unitary matrices $\mathbf{O}$ and $\mathbf{V}$ arise from an SVD of the matrix $\mathbf{T}$ of single-particle transition amplitudes,

$$\mathbf{t} = \mathbf{O}\mathbf{T}\mathbf{N}^{\dagger}\ , \tag{5.35}$$

where $\mathbf{t}$ is diagonal.

Differentiating Eq. (5.34) affords

$$\bar{\mathbf{C}}_{\mathrm{O}}^{[x]} = \widetilde{\mathbf{C}}_{\mathrm{O}}\mathbf{O}^{[x]} + \widetilde{\mathbf{C}}_{\mathrm{O}}^{[x]}\mathbf{O} \tag{5.36a}$$

$$\bar{\mathbf{C}}_{\mathrm{V}}^{[x]} = \widetilde{\mathbf{C}}_{\mathrm{V}}\mathbf{N}^{[x]} + \widetilde{\mathbf{C}}_{\mathrm{V}}^{[x]}\mathbf{N} \, . \tag{5.36b}$$

Derivatives $\mathbf{O}^{[x]}$ and $\mathbf{N}^{[x]}$ of the transformation matrices requires again the application of the SVD differentiation algorithm, albeit in an entirely different context as compared to Eq. (5.31). This will also return the CI amplitude derivatives $\mathbf{t}^{[x]}$ expressed in the NTO basis. As an input, the SVD differentiation requires $\mathbf{T}$ and the canonical amplitude derivatives, $\mathbf{T}^{[x]}$, which are found by solving coupled-perturbed CIS equations on the isolated fragments.[109] Like the MO coefficient derivatives, only fragment level coupled-perturbed equations are required and the amplitude derivative is zero if the coordinate x is outside of the fragment in question.

5.2.7 Derivatives of the symmetric orthogonalization transformation

To yield the final form of the orbital coefficient derivatives needed in Eq. (5.31) we require the derivative of the symmetric (Löwdin) orthogonalization transformation, which to the best of our knowledge has not been previously reported. The transformation in question is

$$\mathbf{C}^i = \bar{\mathbf{C}}^i(\mathbf{S}^i)^{-1/2} \tag{5.37}$$

where

$$\mathbf{S}^i = \bar{\mathbf{C}}^i\mathbf{s}\bar{\mathbf{C}}^i. \tag{5.38}$$

is the overlap among the set of orbitals. The required derivative is simply

$$\mathbf{C}^{i[x]} = \bar{\mathbf{C}}^{i[x]}(\mathbf{S}^i)^{-1/2} + \bar{\mathbf{C}}^i\big[(\mathbf{S}^i)^{-1/2}\big]^{[x]} \tag{5.39}$$

where the overbars represent non-orthogonal orbitals and their derivatives. Differentiating the condition

$$(\mathbf{S}^i)^{-1/2}(\mathbf{S}^i)^{1/2} = \mathbf{1} \tag{5.40}$$

and rearranging, we obtain

$$\big[(\mathbf{S}^i)^{-1/2}\big]^{[x]} = -(\mathbf{S}^i)^{-1/2}\big[(\mathbf{S}^i)^{1/2}\big]^{[x]}(\mathbf{S}^i)^{-1/2} \; . \tag{5.41}$$

In order to determine $[(\mathbf{S}^i)^{1/2}]^{[x]}$ we differentiate the identity $\mathbf{S}^i = (\mathbf{S}^i)^{1/2}(\mathbf{S}^i)^{1/2}$ to obtain

$$\mathbf{S}^{i[x]} = [(\mathbf{S}^i)^{1/2}]^{[x]}(\mathbf{S}^i)^{1/2} + (\mathbf{S}^i)^{1/2}[(\mathbf{S}^i)^{1/2}]^{[x]} \tag{5.42}$$

where

$$\mathbf{S}^{i[x]} = \bar{\mathbf{C}}^{i[x]}\mathbf{s}\bar{\mathbf{C}}^i + \bar{\mathbf{C}}^i\mathbf{s}^{[x]}\bar{\mathbf{C}}^i + \bar{\mathbf{C}}^i\mathbf{s}\bar{\mathbf{C}}^{i[x]} \; . \tag{5.43}$$

Equation (5.42) takes the common form of a Sylvester, or more specifically a Lyapunov equation, solvers for which are available in many linear algebra packages. By solving Eq. (5.42) for $[(\mathbf{S}^i)^{1/2}]^{[x]}$ and using the result from Eq. (5.41) the desired derivative is obtained.

5.2.8 Method validation via the derivation and evaluation of the direct expression for the CIS derivative coupling in the NTO basis

At this point it is prudent to digress momentarily and check the validity of our approach by evaluating some intermediate quantity. The previous derivations rely on

the fact that that properties of determinantal wavefunctions are invariant to unitary orbital rotations within occupied and virtual subspaces. Crucial to our approach, the derivatives of the wavefunction are one such property. It is useful to verify this condition numerically as a sanity check and, at the same time, verify the correctness of the SVD derivative algorithm (appendix A). To that end, we assert that the derivative couplings computed for CIS states in the canonical HF basis must be equal to the derivative couplings computed for CIS states in the NTO basis,

$$\langle \tilde{\Psi}_K | \tilde{\Psi}_L^{[x]} \rangle = \langle \bar{\Psi}_K | \bar{\Psi}_L^{[x]} \rangle. \tag{5.44}$$

For this exercise, we are only concerned with supersystem states, computed for a single fragment, therefore in this section we will suppress the fragment indices, instead the subscripts K, and L index CIS states for this single fragment system; overbars and tildes indicate states in a canonical MO and NTO basis, respectively. Eq. 5.44 states that the derivative couplings should remain constant following the unitary transformation to the NTO basis, which includes an SVD derivative. Therefore, numerical evaluation of these quantities for some example systems will serve as an ideal test case for our general approach.

By utilizing derivatives of second quantized operators, Fatehi and coworkers[103] derived the following expression for 'direct' CIS derivative couplings,

$$\langle \Psi_K | \Psi_L^{[x]} \rangle = \sum_{ia} T_K^{ia} T_L^{ia[x]} - \sum_{iab} T_K^{ia} T_L^{ib} \langle b | a^{[x]} \rangle - \sum_{ija} T_K^{ia} T_L^{ja} \langle j | i^{[x]} \rangle, \tag{5.45}$$

where $\langle r|s^{[x]}\rangle$ represents the overlap of r with the derivative of orbital s, also known as the right overlap derivative. This expression is completely valid for the quantity on the LHS of Eq. 5.44 however, it assumes orthogonality among the CIS states which is indeed the case for the canonical basis. On the other hand, the NTO transformation is specific to a particular CIS state meaning that different orbital rotations are performed on different states and they are not guaranteed to be orthogonal among one another, $\langle\bar{\Psi}_K|\bar{\Psi}_L\rangle \neq \delta_{KL}$. Therefore, we need one final ancillary derivation before we can evaluate Eq. 5.44 and test our approach.

We can follow the procedure set forth by Fatehi et al and write the second quantized form of the direct expression for the derivative coupling,

$$\langle\bar{\Psi}_K|\bar{\Psi}_L^{[x]}\rangle = \sum_{ia}^{K}\sum_{jb}^{L} t_K^{ia[x]} t_L^{jb} \langle\bar{\Phi}_K|\hat{K}_i^\dagger \hat{K}_a \hat{L}_b^\dagger \hat{L}_j|\bar{\Phi}_L\rangle + t_K^{ia} t_L^{jb} \langle\bar{\Phi}_K|\hat{K}_i^\dagger \hat{K}_a \left(\hat{L}_b^\dagger \hat{L}_j|\bar{\Phi}_L\rangle\right)^{[x]}. \tag{5.46}$$

This version of the expression assumes two different sets of MOs associated with the NTO bases of the different states. The operators $\hat{K}_r$ ($\hat{K}_r^\dagger$) and $\hat{L}_s$ ($\hat{L}_s^\dagger$) create (annihilate) orbitals and $|\bar{\Phi}_K\rangle$ and $|\bar{\Phi}_L\rangle$ represent the associated ground state determinants in the K and L NTO bases, respectively. The two sets of orbitals are not assumed to be orthogonal so the behavior of their non-orthogonal second quantized operators must be established and this has been has been derived previously,

$$\langle\text{vac}|\hat{K}_i\hat{L}_j^\dagger|\text{vac}\rangle = S_{KL}^{ij} \tag{5.47a}$$

$$\langle\text{vac}|\hat{K}_a\hat{L}_b^\dagger|\text{vac}\rangle = S_{KL}^{ab} \tag{5.47b}$$

$$\langle \text{vac}|\hat{K}_i \hat{L}_a^\dagger|\text{vac}\rangle = 0. \tag{5.47c}$$

Here, S_{KL}^{ij} represents the overlap of the orbitals i and j belonging to the NTO basis for states K and L, respectively, and the final expression is true because the occupied and virtual subspaces remain orthogonal. The following anti-commutators are also required,

$$\{\hat{K}_p, \hat{K}_q\} = 0 \tag{5.48a}$$

$$\{\hat{K}_p^\dagger, \hat{K}_q\} = \delta_{pq} \tag{5.48b}$$

$$\{\hat{K}_p, \hat{L}_q\} = 0 \tag{5.48c}$$

$$\{\hat{K}_p^\dagger, \hat{L}_q\} = S_{KL}^{pq}. \tag{5.48d}$$

Now, Eq. 5.46 can be expanded and the second quantized operators can be contracted following the conditions outlined in Eq. 5.47 and Eq. 5.48 and the resulting expression is reassuringly similar to the canonical case,

$$\begin{aligned}\langle \bar{\Psi}_K|\bar{\Psi}_J^{[x]}\rangle = \sum_{ia}^{K}\sum_{jb}^{L} t_K^{ia} t_L^{jb} S_{KL}^{ij} S_{KL}^{ab} - \sum_{ia}^{K}\sum_{jbc}^{L} t_K^{ia} t_L^{jb} S_{KL}^{ij} S_{KL}^{ac} \langle b_K|c_L^{[x]}\rangle \\ - \sum_{ia}^{K}\sum_{jkb}^{L} t_K^{ia} t_L^{jb} S_{KL}^{ik} S_{KL}^{ab} \langle j_K|k_L^{[x]}\rangle,\end{aligned} \tag{5.49}$$

where $\langle r_K|s_L^{[x]}\rangle$ is equivalent to the right overlap derivative of orbitals belonging to the different NTO basis sets.

Now, we can evaluate Eq. 5.44 using MO coefficient and amplitude derivatives as well as the SVD differentiation algorithm. Results are presented in Table 5.2.8.

System	He_2/6-311G	LiH/CC-PVDZ	LiH/CC-PVDZ
States	S_1-S_4	S_1-S_4	S_1-S_4
Coordinate	$He:_1$ z	Li: z	Li: y
Basis		Derivative Coupling	
Canonical	$1.826657089459 \times 10^{-1}$	$1.774421212528 \times 10^{-2}$	$9.318777557964 \times 10^{-16}$
NTO	$1.826657089459 \times 10^{-1}$	$1.774421212528 \times 10^{-2}$	$7.811558751539 \times 10^{-16}$

System	H_2O/6-31G	Ethene/CC-PVDZ	Cytosine/6-31G
States	S_1-S_2	S_1-S_4	S_1-S_2
Coordinate	O: x	C_1: y	C_1: x
Basis		Derivative Coupling	
Canonical	-2.355290357313	$8.194371196657 \times 10^{-1}$	-1.424450524868
NTO	-2.355290355453	$8.19437119666 \times 10^{-1}$	-1.424450524868

Table 5.1: Comparison of direct calculation of the CIS derivative coupling in the canonical and NTO basis sets for a variety of systems. All coefficient and amplitude derivatives were computed by solving the requisite coupled-perturbed equations in Q-Chem.

As is readily apparent, derivative couplings evaluated directly in the canonical and NTO basis agree with each other quite well and validate our overall approach to the AIFDEM derivatives.

5.2.9 Vibronic Hamiltonian and exciton/phonon couplings

Derivative couplings are of course useful for describing crossings of adiabatic potential surfaces, and in the case of organic (molecular) semiconductors they also describe the influence of phonons and intramolecular vibrational modes on exciton or charge carrier mobility, a crucial aspect of energy transfer.[86] This requires a somewhat different approach as compared to methods designed to simulate nonadiabatic dynamics in finite molecular systems.

The Holstein-Peierls vibronic Hamiltonian is a popular way to understand energy transfer organic photovoltaic materials, which successfully reproduces experimental carrier mobilities in a variety of systems.[117–120] The model consists of molecular sites $A, B, \ldots$ with site energies $E_A, E_B, \ldots$ and electronic couplings ("transfer integrals"[86]) V_{AB}, all of which are modulated by a collection of harmonic vibrations, as would seem appropriate for a crystalline environment. The vibronic Hamiltonian is

$$\begin{aligned}\hat{\mathcal{H}} = \sum_A \left[E_A + \sum_\theta \tfrac{1}{2}\left(\dot{q}_\theta^2 + \omega_\theta^2\, q_\theta^2\right) + g_{AA\theta}\, q_\theta \right] \hat{a}_A^\dagger \hat{a}_A \\ + \sum_{AB} \left(V_{AB} + \sum_\theta g_{AB\theta}\, q_\theta \right) \hat{a}_A^\dagger \hat{a}_B \ ,\end{aligned} \tag{5.50}$$

where operators $\hat{a}_A^\dagger$ and $\hat{a}_A$ create and annihilate an excitation on site A, and the parameters $g_{AA\theta}$ and $g_{AB\theta}$ are exciton/phonon coupling constants. Couplings $g_{AA\theta}$ are said to be of "Holstein" or "local" type, and quantify how the site energy E_A changes along the dimensionless normal mode coordinate q_θ, whereas "Peierls" or "non-local" couplings $g_{AB\theta}$ quantify the changes in the intersite couplings. (Vibrations could be treated quantum mechanically by replacing q_θ and $\dot{q}_\theta$ with the appropriate operators, as we did in a recent quantum dynamics simulation of singlet fission in crystalline tetracene that demonstrated the importance of vibronic coupling in driving the process.[3])

In practice, the site energies E_A are often approximated as the HOMO energies of the monomers and the transfer integrals V_{AB} as HOMO/LUMO couplings.[86] Exciton/phonon couplings have always been computed numerically through finite difference of the site energies and transfer integrals,[121] with variances sampled over molecular

dynamics trajectories,[122] or else back-computed from relaxation energies.[120,123] Often it is only practical to compute couplings for just a few modes. Up to constants, however, the exciton/phonon couplings $g_{AA\theta}$ and $g_{AB\theta}$ in Eq. (5.50) are simply derivatives of H_{AA} and H_{AB} with respect to q_θ. Herein, we will compute these couplings for the unit cell of tetracene, for all of the vibrational modes q_θ.

To do this, we must first transform the non-orthogonal AIFDEM Hamiltonian derivatives $H_{AB}^{[x]} \rightarrow D_{AB}^{[x]}$ to an orthogonal basis, including the derivative of the orthogonalization transformation. For the latter, we use the symmetric orthogonalization derivative derived in Eq. (5.41), with $\mathbf{S}^i$ replaced by the AIFDEM overlap matrix $\mathbf{S}$ from Eq. (5.5). Following this, only a simple coordinate transformation is required:

$$g_{AB\theta} = (2\mu_\theta\omega_\theta)^{-1/2} \sum_x D_{AB}^{[x]} L_{x\theta} \; . \tag{5.51}$$

The matrix $\mathbf{L}$ is the transformation whose column θ contains the normalized Cartesian displacements corresponding to q_θ. This mode has frequency ω_θ and effective mass μ_θ, whose inverse is defined by[124]

$$\mu_\theta^{-1} = \sum_x L_{x\theta}^2 \; . \tag{5.52}$$

In some literature the factor of $2^{-1/2}$ in Eq. (5.51) is folded into the coordinate transformation $\mathbf{L}$; we follow the convention used in Ref. 125. Exciton/phonon couplings in this work have dimensions of energy.

5.2.10 Implementation and computational scaling

AIFDEM derivatives were implemented in a locally-modifed version of Q-Chem,[34] and will be available in the v. 5.0 release. The entire AIFDEM framework, including

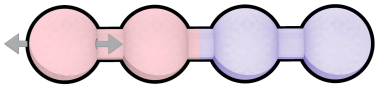

Figure 5.1: Nuclear displacement of He_4 that is considered for the comparisons against finite-difference results in Table 5.2. The two colors indicate how the system is divided up into a pair of He_2 fragments.

the derivatives, is implemented following an object-oriented strategy that simplifies addition of new types of basis states, *e.g.*, the charge-transfer states that were included in the singlet fission calculations in Ref. 3. As shown in Table 5.2 for a particular displacement of He_4 (treated as a pair of He_2 fragments, as shown in Fig. 5.1), analytic derivative results for $H_{AB}^{[x]}$ agree with finite-difference results to within $\sim 10^{-6}$ a.u. in each individual matrix element. Note that because the basis-state orbitals are arbitrary up to phase, the sign of the matrix elements is not guaranteed to be consistent for all displacement steps when numerical differentiation is employed. This necessitates cumbersome sign-matching schemes. A benefit of analytic derivatives is that the relative signs of the matrix element derivatives remain consistent and meaningful.

Computation of $H_{AB}^{[x]}$ in Eq. (5.28) has three potentially expensive steps. Recognizing that contractions of the form $\mathbf{F}^{ij} = \mathbf{\Pi} \cdot \mathbf{G}^{ij}$ are the primary bottleneck in energy calculations using the original AIFDEM,[1] we expect the analogous contractions $\mathbf{F}^{ij[x]} = \mathbf{\Pi}^{[x]} \cdot \mathbf{G}^{ij}$ to be a second potential bottleneck. Formation of $\mathbf{G}^{ij[x]}$ [Eq. (5.31)] is also a potential bottleneck; the cost of this step is dominated by the cost of evaluating the SVD derivative.

The total time for an AIFDEM derivative calculation and the contributions from

$H^{[x]}_{MN}$ Absolute Finite Difference			
	$\|\Psi_A\Psi_B\rangle$	$\|\Psi^*_A\Psi_B\rangle$	$\|\Psi_A\Psi^*_B\rangle$
$\|\Psi_A\Psi_B\rangle$	0.027254	0.024589	0.015125
$\|\Psi^*_A\Psi_B\rangle$	0.024589	0.048970	0.004776
$\|\Psi_A\Psi^*_B\rangle$	0.015125	0.004776	0.026642

$H^{[x]}_{MN}$ Analytic Derivative			
	$\|\Psi_A\Psi_B\rangle$	$\|\Psi^*_A\Psi_B\rangle$	$\|\Psi_A\Psi^*_B\rangle$
$\|\Psi_A\Psi_B\rangle$	0.027254	−0.024589	−0.015125
$\|\Psi^*_A\Psi_B\rangle$	−0.024589	−0.048970	−0.004776
$\|\Psi_A\Psi^*_B\rangle$	−0.015125	−0.004776	0.026642

$S^{[x]}_{MN}$ Absolute Finite Difference			
	$\|\Psi_A\Psi_B\rangle$	$\|\Psi^*_A\Psi_B\rangle$	$\|\Psi_A\Psi^*_B\rangle$
$\|\Psi_A\Psi_B\rangle$	0.000000	0.002105	0.001213
$\|\Psi^*_A\Psi_B\rangle$	−0.002105	0.000047	0.000489
$\|\Psi_A\Psi^*_B\rangle$	−0.001213	0.000489	0.000062

$S^{[x]}_{MN}$ Analytic Derivative			
	$\|\Psi_A\Psi_B\rangle$	$\|\Psi^*_A\Psi_B\rangle$	$\|\Psi_A\Psi^*_B\rangle$
$\|\Psi_A\Psi_B\rangle$	0.000000	0.0021054	0.001213
$\|\Psi^*_A\Psi_B\rangle$	0.002105	−0.000046	0.000489
$\|\Psi_A\Psi^*_B\rangle$	0.001213	0.000489	−0.000062

Table 5.2: Derivatives $H^{[x]}_{MN}$ of the Hamiltonian matrix elements and derivatives $S^{[x]}_{MN}$ of the overlap matrix elements, for three different basis states M and N for $(He_2)_2$, using the aug-cc-pVTZ basis set. All NTOs were retained in these calculations, and the SCF and CIS convergence thresholds were both set to 10^{-10} a.u. while the integral screening threshold was 10^{-14} a.u. The finite-difference calculations used a five-point stencil central difference with displacements of 10^{-4} Å. (The particular displacement x is shown in Fig. 5.1.)

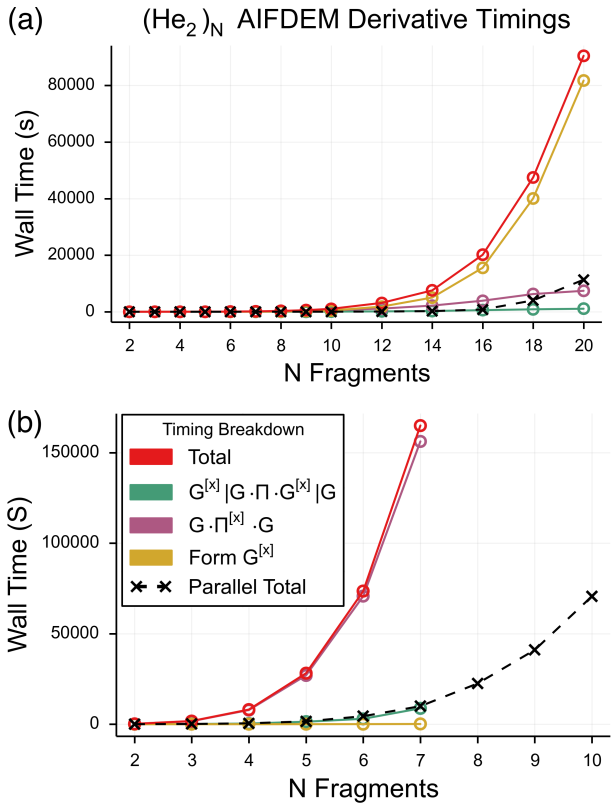

Figure 5.2: Timing breakdown for derivative coupling calculations in linear helium chains in the (a) 6-311G and (b) aug-cc-pVTZ basis sets, retaining all NTOs in each case. All timings are measured on dual-socket Xeon E5-2680 v4 nodes with 128 Gb of memory. Timing breakdowns are run in serial while parallel calculations use 28 cores.

these components for linear chains of He_2 fragments is shown in Fig. 5.2, for two different AO basis sets. Unlike an AIFDEM energy calculation, for calculating derivatives the cost to construct $\mathbf{F}^{ij}$ is a negligible fraction of the total cost, as our algorithm reuses these intermediates so that they do not need to be computed for each coordinate x. The bottleneck step is different in the two basis sets, switching from formation of $\mathbf{G}^{ij[x]}$ (6-311G) to the contraction to form $\mathbf{F}^{ij[x]}$ (aug-cc-pVTZ). This is in line with expectations as the former step formally scales as $\mathcal{O}(N_{\text{occ}}^4)$ and the latter (in the absence of integral screening) as $\mathcal{O}(N_{\text{basis}}^4)$, so that the contraction to form $\mathbf{F}^{ij[x]}$ will dominate when $N_{\text{basis}} \gg N_{\text{occ}}$. For a more realistic system, namely, tetracene dimer in a 6-31+G* basis, about 14% of the cost comes from forming $\mathbf{G}^{ij[x]}$ and about 86% from forming $\mathbf{F}^{ij[x]}$.

In a standard AIFDEM derivative calculation, the derivative of each matrix element H_{AB} must be evaluated for each atomic coordinate x, which is approximately $3N_{\text{atom}}N_{\text{frag}}^2$ matrix elements. Each of these calculations is entirely independent, however, and can therefore be parallelized trivially and with unit efficiency. Our algorithm parallelizes matrix elements such that derivatives for the three Cartesian coordinates on a single nucleus are computed in a single batch assigned to one core. Including a greater number of $H_{AB}^{[x]}$ in a batch could potentially increase the efficiency of integral derivative evaluation at the expense of reduced parallelism; this is a potential means of optimization to be explored in the future. Parallelization is accomplished with MPI, with dynamic load balancing, and parallel performance on a 28-core node is demonstrated for helium chains in Fig. 5.2. Parallel speedup is nearly ideal and

this excellent performance allows us to treat moderately-sized systems easily, with adequate basis sets.

5.3 Computational Details

5.3.1 Tetracene crystal structure and phonon modes

Plane-wave DFT calculations to obtain the phonon spectrum of tetracene were performed using the Quantum Espresso package.[126] Variable unit cell optimization was performed, starting from the experimental crystal structure,[127,128] under 1 atm of pressure. As in our previous work on tetracene,[3] calculations were performed using the local density approximation (LDA) and norm-conserving pseudopotentials, with an SCF convergence threshold of 10^{-9} a.u., mixing parameter $\beta = 0.7$, and kinetic energy cutoff of 60 Rydberg (= 120 Hartree) for the plane-wave (PW) basis. The Brillouin zone was sampled using a $2 \times 2 \times 1$ k-point mesh, and phonon modes were then computed for this optimized structure at the Γ point.

As noted by Abdulla *et al.*,[129] lack of support for dispersion-corrected functionals for phonon calculations presents a major obstacle for studies of conjugated organic systems. A workaround is to forgo the use of a generalized gradient approximation in favor of LDA, as the latter has a tendency to overestimate binding energies, thereby compensating for the absence of attractive dispersion interactions. This is the approach that we take, and our computed phonon modes are in good agreement with those reported in Ref. 129

5.3.2 Exciton model and derivatives

AIFDEM calculations were performed on an asymmetric tetracene dimer extracted from the DFT-optimized crystal structure, which constitutes the unit cell for crystalline tetracene. Exciton-site basis states, Eqs. (5.7) and (5.9), were constructed from fragment wave functions computed at the Hartree-Fock and CIS levels. AIFDEM calculations for the excited states and AFIDEM derivative calculations used a threshold of 50% of the norm of the transition vector in the NTO basis to eliminate terms, *e.g.*, from Eq. (5.9). Triplet basis states were constructed using the appropriate CSFs, as described in our previous work.[3]

Derivatives $H_{AB}^{[x]}$ were used to compute the couplings $g_{AA\theta}$ and $g_{AB\theta}$ for all phonon modes q_θ. To make contact with existing literature, we define the contributions to the relaxation energy due to the Holstein couplings, sometimes called the polaron binding energy, as

$$\epsilon_{AA\theta} = g_{AA\theta}^2/\omega_\theta \; . \tag{5.53}$$

The off-diagonal contribution to the relaxation energy, which is sometimes called the lattice distortion energy, is defined as

$$\epsilon_{AB\theta} = g_{AB\theta}^2/2\omega_\theta \; . \tag{5.54}$$

Although slightly different definitions can be found in the literature,[86] we adopt those used in Ref. 125, as we will make contact with that work in what follows. Furthermore, in the following discussion we use the terms "relaxation energies" and "couplings" interchangeably, as the two are directly related via Eqs. (5.53) and (5.54).

5.4 Numerical Results

Plots of the reorganization energies with the associated phonon mode frequency, as computed for the unit cell of of crystalline tetracene from the PW-LDA calculations are presented in Fig. 5.3. Exciton/phonon couplings for triplet exciton mobility in tetracene have not been reported previously, to the best of our knowledge, but have been reported for crystalline anthracene.[125] As these structures differ only by a single conjugated ring we would expect some similarity with tetracene, despite the very different computational methodology that is used in Ref. 125.

For the Holstein couplings in tetracene, we find a large number of significant couplings for phonon frequencies ω_θ $\sim$1200–1600 cm^{-1}, with additional significant couplings between 500–1000 cm^{-1}. There are essentially no Peierls couplings above $\sim$250 cm $^{-1}$, and these are strongly dominated by a single coupling at the lowest-frequency mode, 53.67 cm^{-1}. Each of these observations is in excellent agreement with results for anthracene in Ref. 125. It is worth noting that the efficiency of our method allows us to compute the couplings across the whole range of phonon frequencies, and that this analysis has revealed a cluster of Holstein couplings above above 3000 cm^{-1}, which is a frequency range that has not typically been investigated by others.

Where our results differ from those computed with other methods is in Holstein couplings in the lower frequency range. The presence of couplings in this region is consistent with previous work on anthracene,[125] although in the present case the couplings are significantly more prevalent and their intensity is at least several orders

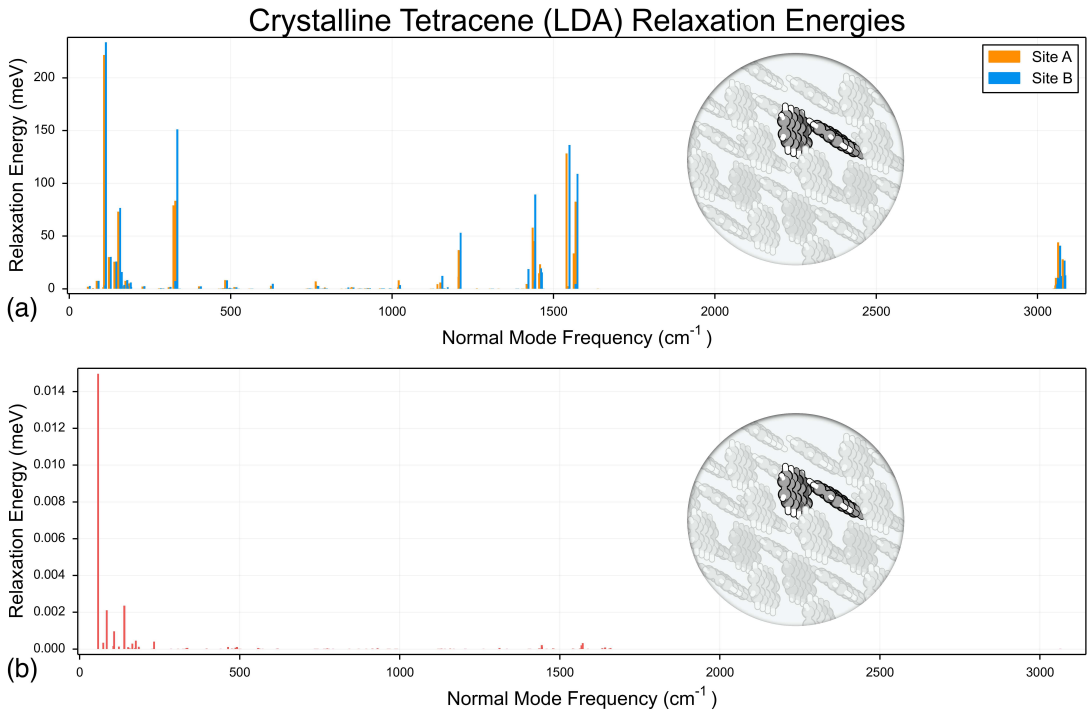

Figure 5.3: Relaxation energies due to (a) local (Holstein) and (b) non-local (Peierls) couplings for crystalline tetracene, computed for the PW-LDA optimized unit cell of the "herringbone" crystal structure of tetracene. Note the significantly different vertical energy scales in the two panels.

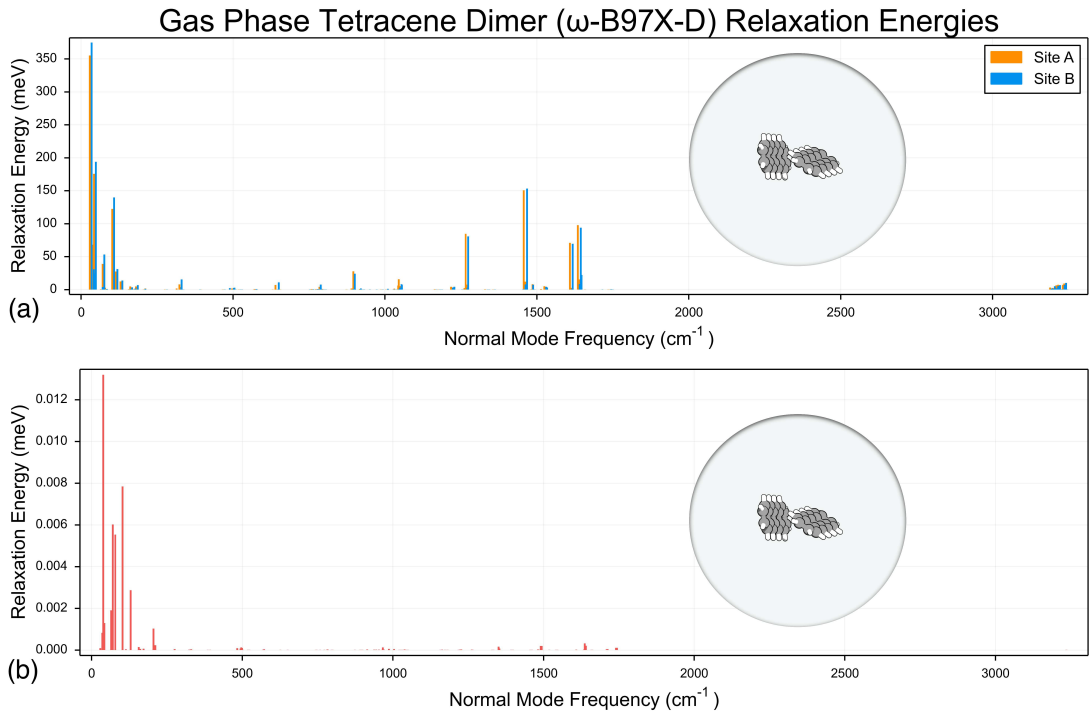

Figure 5.4: Relaxation energies due to (a) local (Holstein) and (b) non-local (Peierls) couplings for gas-phase tetracene dimer, computed in the herringbone configuration at the ω-B97X-D/6-31+G*level.

of magnitude larger. A potential explanation for this discrepancy is that this is an artifact of the somewhat crude proxy for dispersion effects in the phonon mode calculations (substituting LDA in place of a dispersion correction), as these low frequencies are primarily of intermolecular character. Grisanti *et al.*[125] computed the intermolecular phonons using force fields instead.[125] To examine this possible artifact, we have performed a gas-phase optimization and frequency calculation using the dispersion-corrected ω-B97X-D functional.[130] The ωB97X-D optimized dimer exhibits a local minimum in a herringbone-type configuration that is similar to the structure of the

crystalline unit cell, and we use this structure and its vibrational frequencies to compute exciton/phonon couplings, which are plotted in Fig. 5.4. Overall, there is good agreement with couplings computed from the crystalline unit cell, although the couplings for the ωB97X-D structure are slightly blue-shifted in the higher-frequency region and slightly red-shifted at lower frequencies. It is also notable that the gas-phase Holstein couplings $g_{AA\theta}$ and $g_{BB\theta}$ for the dimer pair AB are nearly degenerate for the ωB97X-D geometry, for which the monomers have more flexibility to relax into similar geometries. The two Holstein couplings in each AB pair also have similar magnitudes, again suggesting that the unexpectedly large couplings in the low-frequency regime is not an artifact of the frequencies.

Grisanti *et al.* compute the Holstein couplings for anthracene using a "triplet-in-a-cluster" scheme, in which a central molecule in a cluster (taken from the crystal structure) is optimized to the triplet equilibrium geometry of the monomer, in order to enforce localization of the triplet onto the central monomer.[125] (This represents a diabatization, of sorts.) Reorganization energies are then computed for the entire cluster via distortions along the phonon coordinates. With this in mind, it is not surprising that the result is couplings that are small for low-frequency phonons, as the triplet is not only in a relaxed geometry but is free to respond to polarization induced by the vibrations. (A complete SCF calculation is performed at the perturbed geometries.) Although this scheme is certainly physically justifiable, as the intramolecular reorganization and polarization occur on much faster timescales than the intermolecular vibrations, our approach is arguably a more rigorous realization

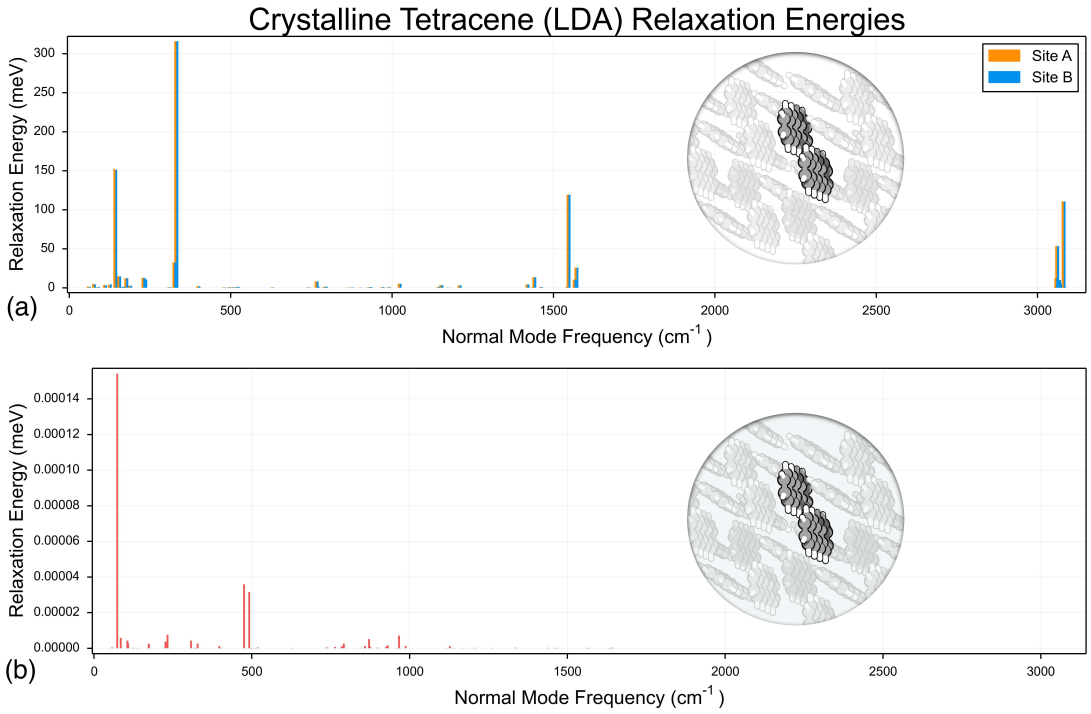

Figure 5.5: Relaxation energies due to (a) local (Holstein) and (b) non-local (Peierls) couplings for crystalline tetracene computed for the parallel-stacked dimer.

of Eq. (5.50) insofar as our perturbations along the phonon modes are infinitesimal. A comprehensive assessment of the relative merits of either approach is outside the scope of this work.

Thanks to the relatively low cost of our method, we can compute couplings for additional dimer configurations in order to compare pathways of mobility through the crystal. To that end we have extracted two more dimer configurations from the crystal structure which were then also used for exciton/phonon coupling calculations. The first is a parallel-stacked configuration and the second is a parallel but offset along the

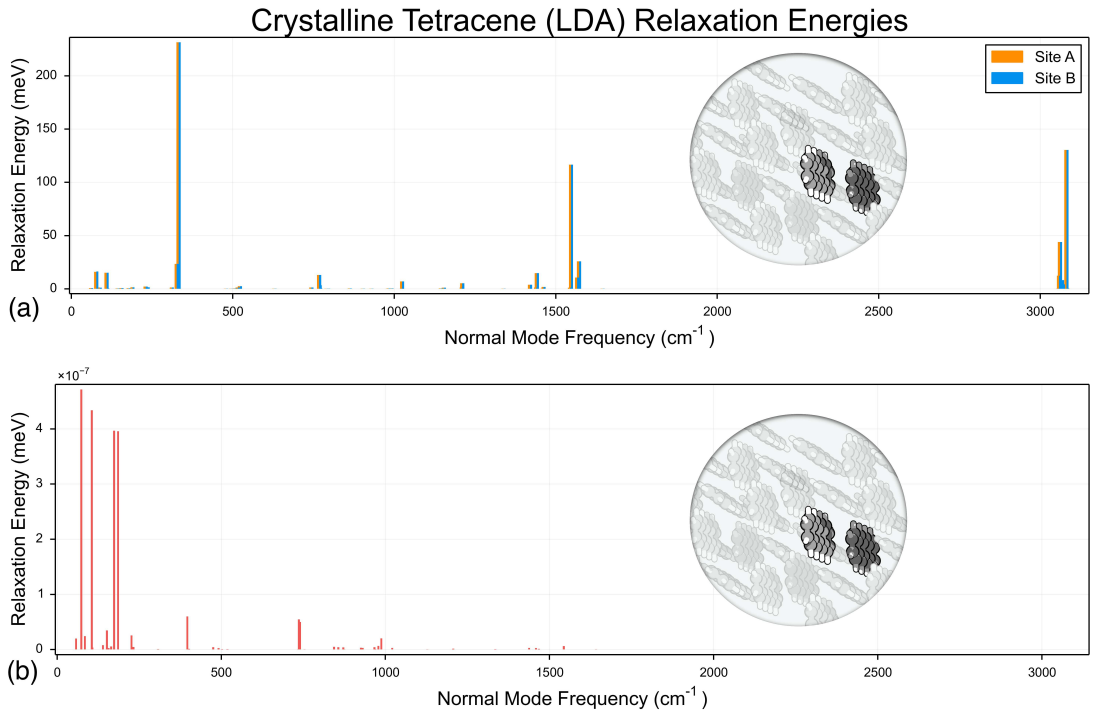

Figure 5.6: Relaxation energies due to (a) local (Holstein) and (b) non-local (Peierls) couplings for crystalline tetracene, computed for the parallel-offset dimer.

long molecular axis; these will further be referred to as the stacked and offset configurations, respectively. Couplings for the stacked geometry are presented in Fig. 5.5 and for the offset geometry in Fig. 5.6. In general, the couplings for both of these configurations are quite similar, which is perhaps unsurprising as the geometries differ only by translation along a single coordinate. There is still qualitative agreement with the "herringbone stacked" (unit cell) configuration, although both of the new configurations involve symmetric dimers so the variation in and frequencies and magnitudes is reduced relative to the unit cell configuration. In both cases, the strongest Holstein couplings lie around ~ 325 cm^{-1} while the remaining lower-frequency couplings are significantly diminished as compared to the unit cell configuration and, in the case of the offset configuration, essentially vanish entirely. Interestingly, the couplings in the frequency range greater than 3000 cm^{-1} significantly increase in magnitude, relative to the unit cell configuration. On the other hand, the Peierls couplings decrease by two orders of magnitude for the parallel configuration and essentially vanish for offset, suggesting that these couplings play a minimal role in exciton transport outside of herringbone stacked pairs.

Recently, there has been significant interest in the nonadiabatic effects that potentially play a role in the singlet exciton fission process[88,110,131,132]. Specifically of interest are phonon modes that might modulate the crucial transition from a localized singlet exciton state to the triplet-pair intermediate. Several recent experiments[133,134] have implicated high-frequency phonon modes, in the range of $\sim$1200–1600 cm^{-1}, as being key to the fission mechanism. It is therefore notable that we have found the

Mode	ω_θ (cm^{-1})	$\epsilon_{AA\theta}$ (meV)	$\epsilon_{BB\theta}$ (meV)
127	1432.19	57.84	8.02
128	1434.08	45.10	89.32
137	1536.86	128.17	0.41
138	1539.89	2.44	136.30

Table 5.3: Relaxation energies (in the tetracene unit cell geometry) for the four phonon modes identified in Ref.3 (in the context of singlet fission) as having significant $S_1/^1(TT)$ coupling in crystalline tetracene.

exciton/phonon couplings for the triplet to be significant in this frequency range. Very recently, by utilizing AIFDEM nonadiabatic coupling calculations, we identified four high-frequency phonon modes that appear to drive the singlet fission transition in crystalline tetracene.[3] Remarkably, we have found these four modes to be significant to triplet exciton transport as well, with the corresponding Holstein couplings possessing substantial magnitude for all three crystal configurations. Reorganization energies for these modes are provided in Table 5.3. As these modes are predominantly localized on individual monomers,[3] these couplings serve primarily to modulate the individual site energies. This correspondence suggests that the same phonon modes that induce the singlet exciton to triplet-pair transition [$S_1 \rightarrow {}^1(TT)$] also play a significant role in the subsequent transport of the free triplet excitons.

5.5 Conclusions

In this work, we have derived expressions for nonadiabatic derivative couplings within the theoretical framework of our novel AIFDEM excited-state method. This formalism also affords the Holstein and Peierls exciton/phonon coupling constants that are important in the description of carrier transport in solid-state semiconductors. The central task in computing of these quantities is the calculation of the derivatives of the AIFDEM Hamiltonian matrix elements H_{AB} between monomers A and B, a procedure for which we have derived and implemented. As an ancillary result, we have derived expressions for derivatives of the NTO transformation and for Löwdin's symmetric orthogonalization transformation, formulas for which have not previously been reported. Our implementation agrees with finite-difference results and exhibits excellent parallel scalability when matrix element derivatives are distributed across multiple cores.

We have used this new approach to compute the exciton/phonon couplings that modulate triplet exciton mobility in crystalline tetracene, comparing our results to calculations of the couplings for crystalline anthracene, performed with an entirely different computational method.[125] Mostly the agreement is quite good, with the exception of the low-frequency intermolecular Holstein couplings for which our approach predicts significantly larger couplings as compared to Ref. 125. We conclude that the discrepancies are most likely due to methodological differences; our method computes $\partial H_{AB}/\partial x$ using analytic differentiation of rigorously-defined diabatic states and is therefore free of the polarization contamination that arises in finite-displacement

procedures.

Our calculations on tetracene indicate that triplet mobility is influenced by strong local couplings to intramolecular modes in the range of 1400–1600 cm^{-1}, and to intermolecular modes from 50–300 cm^{-1}. We have also identified a cluster of local couplings > 3000 cm^{-1}. The distribution of all of these local couplings remains qualitatively similar for various dimers selected from the tetracene crystal structure. The non-local couplings, on the other hand, are due entirely to low-frequency intermolecular modes < 200 cm^{-1}, which vanish for any dimer configuration other than the unit cell. Four high-frequency modes that have been previously identified as "driving modes" for singlet exciton fission[3] exhibit significant couplings within this model, suggesting that the same modes that drive singlet fission may also modulate the subsequent triplet exciton transport.

5.6 Future Work

The AIFDEM *ansatz* is flexible in that various types of basis states may be included. An obvious extension is to include charge-transfer states of the form $|\Psi_A^+\Psi_B^-\rangle$, which were included in the AIFDEM study of singlet fission in Ref. 3 but for which analytic derivatives have not yet been implemented. Such an implementation would allow us to treat couplings related charge-carrier mobility [^{1}(TT) $\rightarrow$ T + T]. In addition, we have previously implemented a charge-embedding scheme for the AFIDEM that significantly reduces its cost,[89] but derivatives of the charge-embedded AIFDEM have not yet been implemented. Finally, analytic derivative couplings provide analytic

gradients as a special case, so that *ab initio* molecular dynamics is a possibility if the aforementioned improvements can reduce the cost sufficiently.

CHAPTER 6

Evidence for Singlet Fission Driven by Vibronic Coherence in Crystalline Tetracene

Singlet fission proceeds rapidly and with high quantum efficiency in both crystalline tetracene and pentacene, which poses a conundrum given that the process in tetracene is disfavored by the electronic energetics. Here, we use an *ab initio* exciton model to compute nonadiabatic couplings in the unit cell of tetracene in order to identify the modes that promote this process. Four intramolecular modes in the range 1400–1600 cm^{-1}, which are nearly resonant with the single-exciton/multi-exciton energy gap, appear to play a key role. *Ab initio* calculations of the electron/phonon coupling constants for these modes reveal that they are almost entirely of "Holstein" type, modulating the site energies rather than the inter-site couplings. The constants are used to parameterize a vibronic Hamiltonian, simulations with which suggest a vibronically-coherent singlet fission mechanism that proceeds spontaneously despite unfavorable electronic energetics. In the absence of vibronic coupling there is no significant fission, according to our model.

6.1 Introduction

Singlet fission[59,135] (SF) offers the potential for enhanced solar energy conversion by overcoming the Shockley-Queisser efficiency limit of 30% for single-junction solar cells,[136] by means of harvesting states excited by high-energy photons that would otherwise vibrationally cool before electron transfer could occur. The SF process has been observed in acene derivatives, carotenoids, and other conjugated systems, often on an ultrafast time scale and with unit quantum yield for generation of the "multi-exciton" state, $|^1(T_1T_1)\rangle$. Pentacene-based devices with external quantum efficiencies (ratio of charge carriers to incident photons) of 129% have been reported.[137]

The generally-accepted mechanism for SF is[135]

$$|S_0S_0\rangle \xrightarrow{h\nu} |S_0S_1\rangle \rightarrow |^1(T_1T_1)\rangle \rightarrow |T_1\rangle + |T_1\rangle \tag{6.1}$$

In crystals of pentacene and its derivatives, $2E(T_1) < E(S_1)$ so that SF is energetically favorable, and the process is observed to occur on a time scale of 80–100 fs.[133,138] Theoretical studies, however, indicate that direct electronic coupling between $|S_0S_1\rangle$ and $|^1(T_1T_1)\rangle$ is too weak to be consistent with such a fast time scale.[88,132] Moreover, SF occurs spontaneously in crystalline tetracene as well,[139–141] with high quantum efficiency and (at certain excitation energies) on a sub-picosecond timescale,[139,140] despite the fact that $2E(T_1)$ lies approximately 0.2 eV above $E(S_1)$ in tetracene.[88,142,143] Several mechanisms have been proposed to explain this, including thermally-activated SF from a vibrationally-hot S_1 state, fission from higher-lying S_n states,[88] or an

entropically-driven mechanism.[144] However, these hypotheses are difficult to reconcile with observations that the SF rate is independent of temperature in tetracene[140] (or perhaps nearly so, with an activation energy of ∼0.06 eV in tetracene[145]), and also insensitive to excitation energy.[141] Here, we propose a mechanism to explain SF in tetracene based on a Holstein-Peierls vibronic Hamiltonian,[86,146] with parameters derived from *ab initio* calculations.

Recently, Zhu and co-workers reported direct observation of the $|^1(T_1T_1)\rangle$ state using time-resolved two-photon photoemission.[74] These authors report a ∼20 fs rise time in the triplet population in both tetracene and pentacene, which they attribute to formation of the multi-exciton state. Although others have attributed this signal to free triplet excitons,[147] Zhu *et al.* propose a quantum-coherent mechanism in which the initial photo-excited state is a superposition with singlet as well as multi-exciton character,[74,144] and a phenomenological density matrix simulation reproduced the ultrafast rise time in the $|^1(T_1T_1)\rangle$ population when charge transfer (CT) states were included to mediate the process.[74] However, the phenomenological calculations in support of this mechanism[74,144] have been criticized as requiring interactions with a bath, the demand for which cannot explain the temperature-independence of the SF rate.[148] Finally, the precise role of CT states in SF has been debated,[135,149] with some consensus emerging that these states lie too high in energy to be directly accessed but that the presence of CT character in the single- and multi-exciton states serves as a virtual intermediate, where the CT character contributes to the coupling of the adiabatic states.[61,74,110,132,149,150]

The role of the nuclear degrees of freedom has only recently garnered attention, with two theoretical studies identifying a crossing point on the Born-Oppenheimer potential energy surfaces for the single- and multi-exciton states in pentacene,[88,110] leading to a proposed mechanism involving a conical intersection along an intermolecular "herringbone" coordinate. Indeed, Musser *et al.*[133] report direct experimental evidence for SF through a conical intersection in pentacene, driven by high-frequency vibrational modes, but no such evidence has been reported for tetracene. The study in Ref. 88 failed to find any such intersection along the corresponding herringbone coordinate in tetracene.

A crucial quantity to describe nonadiabatic transitions through conical intersections is the derivative coupling vector

$$\mathbf{d}^{JK} = \langle \Psi_J | \hat{\boldsymbol{\nabla}} | \Psi_K \rangle \tag{6.2}$$

where $\hat{\boldsymbol{\nabla}}$ represents derivatives with respect to nuclear coordinates. This can be related to the nonadiabatic coupling vector

$$\begin{aligned} \mathbf{h}^{JK} &= \langle \Psi_J | (\partial \hat{H} / \partial \mathbf{x}) | \Psi_K \rangle \\ &= (E_J - E_K)\, \mathbf{d}^{JK} \end{aligned} \tag{6.3}$$

These quantities describe the topography and topology around conical intersections and can be said to "drive" nonadiabatic processes.

Derivation and implementation of $\mathbf{h}^{JK}$ vectors is technically involved for any electronic structure model, and the difficulty is compounded in the context of SF by the doubly-excited character of the $|^1(\mathrm{T_1T_1})\rangle$ state. Popular low-cost methods such as time-dependent density functional theory do not capture double excitations,[151] and

are therefore blind to the $|^1(\mathrm{T}_1\mathrm{T}_1)\rangle$ intermediate. Using methods that *do* incorporate double excitations, but using the norm of a single-particle transition density matrix as a proxy for $\mathbf{h}^{JK}$ since the latter is unavailable, Krylov and co-workers have suggested that the nuclear modes that serve to increase electronic coupling do not always increase the nonadiabatic couplings.[110,152,153]

We have recently introduced a novel approach for computing excited-state properties of extended aggregates, based on an *ab initio* Frenkel-Davydov exciton model (AIFDEM).[1,89,90]

6.2 Theory

The Frenkel-Davydov *ansatz* writes the wave function $|\Xi_I\rangle$ for a collective excitation as a linear combination of direct products of monomer states,

$$|\Xi_I\rangle = \sum_{A}^{\text{states}} K_{IA} |\Psi_A^* \Psi_B \Psi_C \cdots\rangle \tag{6.4}$$

where $|\Psi_M\rangle$ and $|\Psi_M^*\rangle$ are ground- and excited-state wave functions for the Mth monomer. This set of direct-products is known as the "exciton-site" basis. Both these states, and the coupling matrix elements between them, can be computed in a trivially parallelizable way. Unlike traditional Frenkel-Davydov models, the AIFDEM need not invoke dipole-coupling, nearest-neighbor, neglect-of-exchange, frontier orbital, or other approximations to the electronic Hamiltonian that couples the basis states.[1]

6.2.1 Multi-Exciton AIFDEM

As in our previous work on the AIFDEM,[1,89] we will describe the monomer wave functions using only single excitations, but for SF we also need to include multi-exciton configurations by coupling two triplet monomer wave functions to an overall singlet. (A somewhat similar approach was recently used to parameterize a lattice model for SF.[154]) Starting from a direct product that includes two fragments in triplet configurations, the additional exciton-site basis states that we need are

$$\begin{aligned}\left|{}^1(\Psi_A^{\mathrm{T}}\Psi_B^{\mathrm{T}})\Psi_C\cdots\right\rangle = \frac{1}{\sqrt{3}}\left|\Psi_A^{\mathrm{T}_{+1}}\Psi_B^{\mathrm{T}_{-1}}\Psi_C\cdots\right\rangle \\ + \frac{1}{\sqrt{3}}\left|\Psi_A^{\mathrm{T}_{-1}}\Psi_B^{\mathrm{T}_{+1}}\Psi_C\cdots\right\rangle - \frac{1}{\sqrt{3}}\left|\Psi_A^{\mathrm{T}_0}\Psi_B^{\mathrm{T}_0}\Psi_C\cdots\right\rangle\end{aligned} \tag{6.5}$$

where $\Psi_M^{\mathrm{T}_m}$ is a triplet wave function on monomer M, with magnetic quantum number m:

$$\left|\Psi_M^{\mathrm{T}_{+1}}\right\rangle = \sum_{ia} t^{ia}\left|\Phi_M^{\bar{i}a}\right\rangle \tag{6.6a}$$

$$\left|\Psi_M^{\mathrm{T}_{-1}}\right\rangle = \sum_{ia} t^{ia}\left|\Phi_M^{i\bar{a}}\right\rangle \tag{6.6b}$$

$$\left|\Psi_M^{\mathrm{T}_0}\right\rangle = \frac{1}{\sqrt{2}}\sum_{ia} t^{ia}\left(\left|\Phi_M^{ia}\right\rangle - \left|\Phi_M^{\bar{i}\bar{a}}\right\rangle\right) \ . \tag{6.6c}$$

Hamiltonian and overlap matrix elements between exciton-site basis functions are computed as described in our previous work,[1,89] and we then solve a generalized the eigenvalue problem

$$\mathbf{HK}_I = \epsilon_I \mathbf{SK}_I \tag{6.7}$$

that affords coefficients $\mathbf{K}_I$ and energies ϵ_I for the Ith eigenstate of the exciton Hamiltonian. Very recently, we have derived and implemented analytic nuclear gradients

and nonadiabatic couplings for this model,[155] such that derivatives $H_{JK}^{[x]} \equiv \partial H_{JK}/\partial x$ can be readily computed and used to investigate which vibrational modes strongly modulate the couplings between eigenstates J and K.

6.3 Results and Discussion

Eigenvectors for a dimer of tetracene extracted from a DFT-optimized crystal structure (see the Supporting Information for details) are presented in Table 6.1. In the following, we have corrected the site energies of the basis states to match the experimental values of 2.3 eV for the $S_0 \rightarrow S_1$ excitation energy and 2.5 eV for twice the S_0/T_1 gap. We find that the singly-excited bright states $|\Xi_{S_1}\rangle$ and $|\Xi_{S_2}\rangle$ are primarily composed of a single basis state and that the optically-dark multi-exciton state, $|\Xi_{TT}\rangle$, is dominated by the triplet-pair basis state with only minor contributions from the singlet states. This is in agreement with other work,[110] and demonstrates that both the single- and multi-exciton states can be characterized by a dominant electron configuration. Relatively weak electronic coupling between the singlet and triplet-pair basis states also suggests that purely electronically coherent oscillations are unlikely to play a significant role in the SF mechanism.

Although the states in question are predominantly single-configuration (up to spin adaptation), mixing with charge-transfer (CT) configurations is thought to be important, as electronic couplings between CT configurations and both single- and multi-exciton configurations are about an order of magnitude larger than the direct coupling between $|S_0S_1\rangle$ and $|^1(TT)\rangle$.[110,131] CT basis states $|\Phi_A^+\Phi_B^-\Phi_C\cdots\rangle$ and

Table 6.1: Eigenvectors for tetracene dimer in the non-orthogonal exciton-site basis.[a]

Eigenstate	$\|\Xi_{S_0}\rangle$	$\|\Xi_{S_1}\rangle$	$\|\Xi_{S_2}\rangle$	$\|\Xi_{TT}\rangle$
Exc. Energy (eV)		2.30	2.36	2.50
Osc. Strength		0.114	0.208	0.000
Basis State	Coefficient			
$\|\Psi_A\Psi_B\rangle$	0.998	0.048	0.035	0.002
$\|\Psi_A^*\Psi_B\rangle$	0.038	-0.994	0.227	-0.009
$\|\Psi_A\Psi_B^*\rangle$	0.047	-0.225	-0.994	-0.011
$\|^1(\mathrm{TT})\rangle$	-0.001	-0.012	-0.010	1.114

[a]50% truncation threshold for the NTOs.

$|\Phi_A^-\Phi_B^+\Phi_C\cdots\rangle$ can easily be added to the exciton-site basis, with the resulting eigenvectors listed in Table 6.2. Our model predicts non-negligible couplings between the excitonic and CT configurations ,with both the single and multi-exciton eigenvectors gaining appreciable CT character. The presence of the CT configurations also leads indirectly to increased mixing of the single- and multi-exciton states, acting as virtual intermediates, as predicted by in several previous studies.[61,74,110,132,149] The CT-dominated eigenstates, however, lie too high in energy to be accessed directly. Despite the slight increase mixing, the character of the eigenstates remains predominantly single-configuration, suggesting that the presence of CT states is not sufficient to induce meaningful electronic coherence.

Nonadiabatic coupling vectors between $|\Xi_{S_1}\rangle$ and $|\Xi_{TT}\rangle$ are provided in the Supporting Information, using both 25% and 50% thresholds for truncating the natural transition orbitals (NTOs). This change in threshold results in a significant change in the norm of $\mathbf{H}_{JK}^{[x]}$, which more than doubles (from 5 to 10 a.u.) when the tighter

Table 6.2: Eigenvectors for tetracene dimer in the non-orthogonal exciton-site basis, including charge-transfer basis states.[a]

Eigenstate	$\|\Xi_{S_0}\rangle$	$\|\Xi_{S_1}\rangle$	$\|\Xi_{S_2}\rangle$	$\|\Xi_{TT}\rangle$	$\|\Xi_{-+}\rangle$	$\|\Xi_{+-}\rangle$
Exc. Energy (eV)		2.30	2.39	2.50	2.69	3.16
Osc. Strength		0.185	0.114	0.011	0.025	0.010
Basis State	Coefficient					
$\|\Psi_A\Psi_B\rangle$	0.996	0.000	0.045	0.041	-0.051	-0.049
$\|\Psi_A^*\Psi_B\rangle$	-0.035	-0.875	0.224	0.308	-0.354	0.070
$\|\Psi_A\Psi_B^*\rangle$	-0.045	0.164	0.972	0.000	0.177	-0.193
$\|\Psi_A^+\Psi_B^-\rangle$	0.040	-0.448	-0.063	-0.346	0.821	-0.004
$\|\Psi_A^-\Psi_B^+\rangle$	-0.025	-0.062	-0.163	0.145	0.011	-0.974
$\|^1(\mathrm{TT})\rangle$	0.002	-0.134	0.080	-0.970	-0.496	-0.170

[a] 50% truncation threshold for the natural transition orbitals.

threshold is used. Tighter thresholds tend to stabilize exciton-site energies and increase coupling magnitudes but the differences affect our results qualitatively (see Tables S2 and S3 in the Supporting Information), at least in this system. As the resulting eigenstates are only slightly more mixed, this significant change in the norm of the derivative coupling reflects the sizable magnitudes of the quantities $\mathbf{H}_{JK}^{[x]}$. Inspection of the individual matrix elements, which contribute directly to the Hellman-Feynman part of $\mathbf{h}^{JK}$, can be quite significant in magnitude, $\sim$100 a.u.

For *intra*molecular SF in 2-methyl-1,5-hexadiene, nonadiabatic couplings computed at the CASSCF(4,4) level are found to be as large as $||\mathbf{h}|| = 172$ a.u. at a particular intersection of the single- and multi-exciton potential surfaces, yet only 0.182 a.u. at the ground-state geometry.[131] The situation is different in tetracene,

however, given that the two potential surfaces do not appear to cross in this system.[60,110] It is therefore notable that we find $||\mathbf{h}|| \sim 10$ a.u. even at the ground-state geometry. This fact, along with the sizable geometry dependance of the elements of $\mathbf{H}^{[x]}_{JK}$, suggests significant nuclear/electronic coupling.

Projection of $\mathbf{H}^{[x]}_{JK}$ onto phonon modes can shed light on the nature of the vibrations that promote SF. Four high-frequency modes depicted in Fig. 6.1(a)–(d) together constitute about 80% of the total projection, which seems sufficiently high to conclude that these are the primary modes that are driving the SF transition, and there is a certain symmetry amongst these modes, consisting of two pairs of intramolecular vibrations localized on each of the two monomers. In pentacene, a conical intersection along a low frequency, intermolecular "herringbone" vibration has been identified,[88,110] which would also modulate the electronic coupling, but we find no such intermolecular contribution in tetracene. The lowest frequency vibration with any significant projection onto the nonadiabatic coupling vector is $\nu_{70} = 855$ cm^{-1} [Fig. 6.1(e)], but although delocalized across the dimer, this mode is primarily a degeneracy-induced linear combination of intramolecular vibrations.

Electron/phonon coupling constants discussed in the context of charge transport in organic photovoltaics are, at their heart, derivatives of the matrix elements of an exciton Hamiltonian.[120] In this context, derivatives $H^{[x]}_{AA}$ are known as "Holstein" couplings and quantify the modulation of site energies due to nuclear motion, while off-diagonal derivatives $H^{[x]}_{A,B\neq A}$ ("Peierls" couplings) quantify how the electronic couplings (sometimes called "transfer integrals"[86]) change due to nuclear

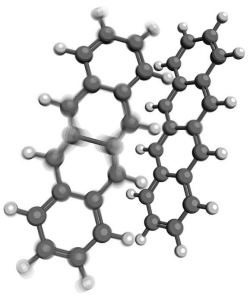

(a)
$\nu_{127} = 1432.19$ cm^{-1}
38.31%

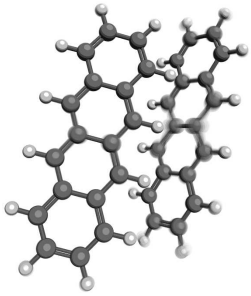

(b)
$\nu_{127} = 1434.08$ cm^{-1}
18.86%

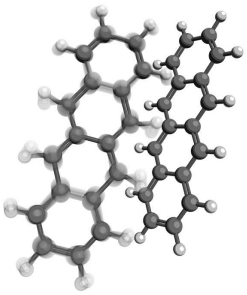

(c)
$\nu_{137} = 1536.86$ cm^{-1}
16.33%

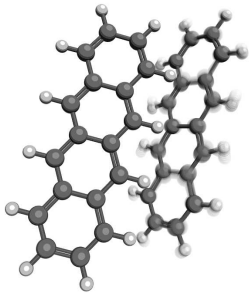

(d)
$\nu_{138} = 1539.89$ cm^{-1}
15.71%

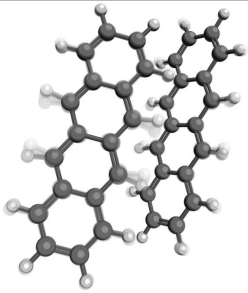

(e)
$\nu_{70} = 855.49$ cm^{-1}
0.60%

Figure 6.1: (a)–(d) Normal modes that strongly couple the S_1 and ^{1}(TT) states in tetracene dimer, which together account for 80% of the norm of $\mathbf{H}^{[x]}_{JK}$. (e) Lowest-frequency vibration having any significant projection onto the nonadiabatic coupling vector.

motion.[117,119,120,156] Both types of couplings can be computed from the AIFDEM, by transforming $H_{AB}^{[x]}$ from nuclear Cartesian displacements to dimensionless spectroscopic coordinates for the respective normal modes.[155] Results for the five normal modes in Fig. 6.1 are presented in Table 6.3.

It is immediately apparent that the dominant electron/phonon couplings for SF in tetracene are of the Holstein type, with the Peierls couplings being 10^3–10^4 times smaller. (Note that Holstein couplings are often called "local" couplings, but for the $|\Xi_{\mathrm{TT}}\rangle$ state the wave function, and therefore the site energy, is a function of both monomers of the dimer.) Values of the Holstein coupling constants ($\approx$ 50–180 meV) are only somewhat smaller than the $\approx$200 meV energy gap between the single- and multi-exciton eigenstates, and this is true even for ν_{70}, the lowest-frequency mode considered here.

In the context of charge transport, it is recognized that the non-local (Peierls) electronic couplings are coupled strongly to low-frequency intermolecular vibrations, and can exhibit fluctuations of the same order of magnitude as the couplings themselves.[122] In contrast, for SF in tetracene these non-local couplings are insignificant and so too are their fluctuations. Instead, trends in electron/phonon couplings predicted by our model suggest that any vibronic character in the eigenstates involved in the SF transition is due to fluctuations in the site energies, with negligible modulation of the couplings.

The most striking result of the vibrational analysis is not apparent in the displacements shown in Fig. 6.1 but rather in the frequencies of the modes in question,

Table 6.3: Electron/phonon coupling constants (in meV) for tetracene dimer.

Basis State	$\|\Psi_A\Psi_B\rangle$	$\|\Psi_A^*\Psi_B\rangle$	$\|\Psi_A\Psi_B^*\rangle$	$\|^1(\mathrm{TT})\rangle$
	$\nu_{70} = 855.49$ cm^{-1}			
$\|\Psi_A\Psi_B\rangle$	-30.726	-0.384	0.431	0.021
$\|\Psi_A^*\Psi_B\rangle$	-0.384	-34.603	-0.038	-0.041
$\|\Psi_A\Psi_B^*\rangle$	0.431	-0.038	-42.187	-0.010
$\|^1(\mathrm{TT})\rangle$	0.021	-0.041	-0.010	10.570
	$\nu_{127} = 1432.19$ cm^{-1}			
$\|\Psi_A\Psi_B\rangle$	-117.40 0	-3.9663	0.813	0.042
$\|\Psi_A^*\Psi_B\rangle$	-3.966	65.772	-0.704	-0.084
$\|\Psi_A\Psi_B^*\rangle$	0.813	-0.7043	-76.367	0.014
$\|^1(\mathrm{TT})\rangle$	0.042	-0.084	0.014	182.907
	$\nu_{128} = 1434.08$ cm^{-1}			
$\|\Psi_A\Psi_B\rangle$	76.788	-1.143	-4.858	-0.006
$\|\Psi_A^*\Psi_B\rangle$	-1.144	101.989	0.824	0.035
$\|\Psi_A\Psi_B^*\rangle$	-4.858	0.824	-96.317	0.017
$\|^1(\mathrm{TT})\rangle$	-0.006	0.035	0.017	-98.108
	$\nu_{137} = 1536.86$ cm^{-1}			
$\|\Psi_A\Psi_B\rangle$	7.124	4.509	-1.008	-0.042
$\|\Psi_A^*\Psi_B\rangle$	4.509	-47.105	-0.620	0.094
$\|\Psi_A\Psi_B^*\rangle$	-1.008	-0.620	-4.092	0.063
$\|^1(\mathrm{TT})\rangle$	-0.042	0.094	0.063	-170.112
	$\nu_{138} = 1539.90$ cm^{-1}			
$\|\Psi_A\Psi_B\rangle$	-16.454	-0.295	3.052	0.062
$\|\Psi_A^*\Psi_B\rangle$	-0.295	-17.219	-0.723	-0.006
$\|\Psi_A\Psi_B^*\rangle$	3.052	-0.7223	54.502	-0.029
$\|^1(\mathrm{TT})\rangle$	0.062	-0.006	-0.029	139.292

corresponding to excitation energies of 170–190 meV for the vibrational fundamentals. This makes vibrational excitation nearly resonant with the energy gap between the single- and multi-exciton eigenstates. Indeed, of all of the vibrational modes, the five discussed here are the best match to the energy gap. Other studies have noted the importance of resonant bath modes in quantum dynamics simulations of SF in pentacene,[132,157] although the vibrational frequencies in those simulations were resonant with the singlet to CT transition rather than the singlet to multi-exciton transition. Recent experiments on pentacene support the participation of high-frequency vibrations to SF.[133,134] Whereas Musser *et al.*[133] propose a conical intersection along these driving modes—a pathway that existing calculations disfavor for tetracene—Bakulin *et al.*[134] propose that these modes couple the single- and multi-exciton states to form a set of vibronic states of mixed electronic character. The suggested mechanism is then a quantum-coherent one, as suggested also by Chan *et al.*,[74] but one induced through vibronic resonance rather than pure electronic coupling.

To examine the possibility of a vibronic mechanism for SF, we use a model Hamiltonian of the Holstein-Peierls form,[86,146] parameterized using our *ab initio* electronic and electron/phonon couplings, and phonon frequencies. Exciton site energies are once again shifted so that excitation energies match experiment. We include a single vibrational degree of freedom (ν_{127}), as this mode has the largest projection along the nonadiabatic coupling vector. The basis used to diagonalize this model Hamiltonian consists of direct products of the AIFDEM electronic states with harmonic oscillators $|\chi_0\rangle$ and $|\chi_1\rangle$ having either 0 or 1 quanta in ν_{127}. The lowest vibronic eigenstates $|\Omega_n\rangle$

Table 6.4: Vibronic eigenstates of a Holstein-Peierls Hamiltonian parameterized using AIFDEM calculations.[a]

Eigenstate	$\|\Omega_0\rangle$	$\|\Omega_1\rangle$	$\|\Omega_2\rangle$	$\|\Omega_3\rangle$	$\|\Omega_4\rangle$	$\|\Omega_5\rangle$	$\|\Omega_6\rangle$
Excitation energy (eV)		2.301	2.306	2.350	2.500	2.560	2.620
Oscillator strength		0.0876	0.0727	0.0645	0.0184	0.0009	0.0013
Basis State	Coefficient						
$\|\Psi_A\Psi_B\rangle\|\chi_0\rangle$	-0.998	0.038	-0.025	-0.035	-0.004	0.012	-0.001
$\|\Psi_A^*\Psi_B\rangle\|\chi_0\rangle$	-0.037	-0.810	0.531	-0.194	0.250	-0.038	0.005
$\|\Psi_A^*\Psi_B\rangle\|\chi_1\rangle$	0.001	0.199	-0.128	0.096	0.955	-0.251	0.012
$\|\Psi_A\Psi_B^*\rangle\|\chi_0\rangle$	-0.046	-0.186	0.098	0.955	-0.114	-0.265	-0.000
$\|\Psi_A\Psi_B^*\rangle\|\chi_1\rangle$	-0.001	-0.029	0.018	0.284	0.230	0.952	0.016
$\|^1(\mathrm{TT})\rangle\|\chi_0\rangle$	0.001	-0.538	-0.826	-0.016	0.012	0.010	-0.519
$\|^1(\mathrm{TT})\rangle\|\chi_1\rangle$	-0.000	0.281	0.436	0.014	0.013	0.009	-0.986

[a] 50% truncation threshold for the natural transition orbitals.

are listed in Table 6.4.

According to these calculations, the multi-exciton-dominated dark state, $|\Omega_6\rangle$, falls higher in energy than in the purely electronic case due primarily to excited vibrational character. Its energy is approximately $2[E(\mathrm{T}_1) - E(\mathrm{S}_0)] + h\nu_{127}$. The two lowest excited states, on the other hand, each possess appreciable oscillator strength and are essentially degenerate with the experimental S_1 state, yet are of decidedly mixed single- and multi-exciton character, as well as mixed $|\chi_0\rangle$ versus $|\chi_1\rangle$ character, suggesting vibronic coherence.

We next use Redfield dissipative dynamics[67–70] to investigate vibronic effects at a qualitative level. The Redfield approach has been used previously to study SF,[74,132,134]

and we have performed such simulations using three different Hamiltonians: purely excitonic, exciton + CT, and vibronic. In order to make a direct comparison between these models we set the exciton-site energies in all three cases equal to those computed in the vibronic case (Table 6.4). The goal is not to reproduce experimental results for the two purely electronic cases but to treat the three cases on an equal footing and thereby identify the role of vibronic coupling. All simulations use a common Ohmic spectral density to describe the vibrational modes (save for the one that is treated explicitly in the vibronic model), by means of a temperature bath with a reorganization energy of 0.3 eV and characteristic frequency of 1450 cm^{-1}. We initially populate the the $|\Psi_A^* \Psi_B\rangle|\chi_0\rangle$ configuration and then propagate the wave packet and plot its projection onto each basis state, in Fig. 6.2.

It is immediately clear that the vibronic model is the only case where the wave packet spontaneously acquires multi-exciton character, despite the electronic energy barrier. The exciton + CT model exhibits a small amount of initial multi-exciton population, but this decays to zero almost immediately. Unsurprisingly, the purely excitonic model does not populate the multi-exciton state at all. The vibronic model, in contrast, populates the multi-exciton state on time scale of $\sim$0.5 ps, which is consistent with an ultrafast transition to an intermediate state with significant multi-exciton character, as suggested by Tayebjee *et al.*[148] and also observed experimentally;[74,144] independent triplets are then accessed through variety of pathways.[139–141] We note that this is a simple model that does not describe all possible SF pathways but these results suggest that vibronic coupling can provide sufficient impetus to overcome the

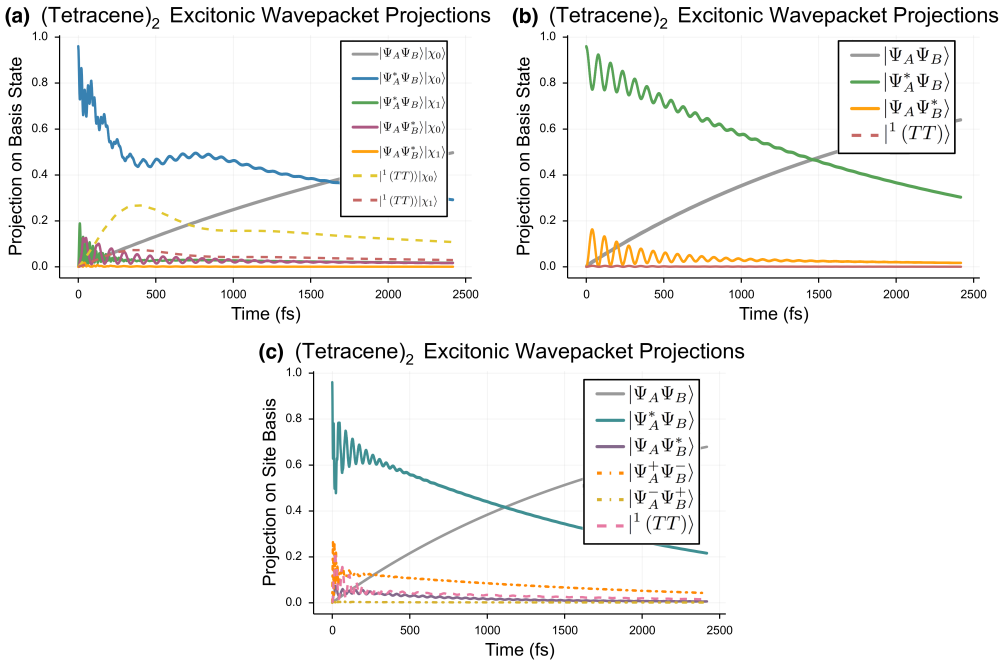

Figure 6.2: Redfield density matrix simulations using different model Hamiltonians: (a) vibronic, (b) purely excitonic, and (c) an excitonic model including CT states.

unfavorable electronic energetics and motivate spontaneous, ultrafast SF in tetracene.

6.4 Conclusions

In summary, we have computed nonadiabatic couplings for crystalline tetracene, for the first time at an *ab initio* level of theory, finding that the coupling pertinent to the $|S_0S_1\rangle \rightarrow |^1(TT)\rangle$ SF transition is significant even at the ground state geometry. Upon projecting the coupling vector onto phonon modes, we identify several *intra*molecular vibrational coordinates that strongly couple the single- and multi-exciton states, and whose vibrational fundamentals lie in near resonance with the single- to multi-exciton energy gap. *Ab initio* electron/phonon coupling constants computed for these modes are primarily of the Holstein type, serving to modulate the site energies rather than the inter-site couplings. Dissipative dynamics simulations using a vibronic Hamiltonian parameterized from these *ab initio* calculations demonstrate that vibronic coupling among these intramolecular modes is sufficient to drive a spontaneous, ultrafast transition to the multi-exciton state from which SF can proceed , despite an electronic energy gap. Although CT states do contribute as virtual intermediates, spontaneous SF is insignificant in the absence of vibronic coupling.

CHAPTER 7

Conclusions and future work

In this work we have derived a new method for excited states, the *ab-inito* Frenkel Davydov Exciton Model (AIFDEM). The goal of the method was an excited state approach that was well suited to scaling with parallel modern architectures, while avoiding the ambiguity and empiricism that comes with many other low cost approaches. The new method was ultimately able to scale merely quadratically with the number of molecular fragments and treat systems with tens of thousands of basis functions while reproducing excitation energies of traditional methods within a few tenths of an eV. Furthermore, the physically based description of the model is able to offer insights into excitation energy dynamics and treat complicated electronic structure. As a representative example, we simulated the dynamics of the excited state of a napthalene-diimide nanotube and found that the signatures of electronic coherence in the transfer mechanism were only present in a model system that was too large to be practical for traditional approaches but could be treated by the AIFDEM with modest hardware. We have also derived and implemented fully analytic derivatives of the AIFDEM in order to compute non-adiabatic couplings and electron-phonon coupling constants. We have computed these quantities for the singlet fission process

in crystalline tetracene in order to investigate the nature of the fission mechanism. We have identified four primary vibrational modes that induce vibronic coherence, driving the fission transition, despite unfavorable electronic energetics.

Despite the efficacy that we have established and the valuable results obtained thus far, the AIFDEM is still quite a young method with a large degree of unexplored potential. The most glaring deficiency stems from the fact that, while the AIFDEM Hamiltonian is exact, the wavefunctions are based off of configuration interaction singles states computed for the fragments. Therefore, the excited states lack the preponderance of dynamical correlation effects, making excitation energies inadequate. A future update would add the missing correlation, perhaps in a perturbative way, starting from configuration interaction singles with perturbative doubles corrections on the fragments and properly coupling these states. A density functional based approach to dynamical correlation is also possible. This extension would lead to more accurate site energies and a more realistic description of excitation dynamics.

The aspirational goal for many of electronic structure methods is to provide a driver for all-atom *ab-initio* molecular dynamics simulations. The ingredients for this are present in the AIFDEM, energies, as well as forces from the derivatives, however their evaluation is too computationally costly to perform realistic dynamics where repeated calculations are required. While the integral digestion required for energy calculations was accelerated using GPUs in Chapter 4, the derivative-integral digestions required for the gradients are still quite expensive and this cost would need to be reduced in order to perform dynamics. A potential avenue is to extend

the derivatives to the charge embedding scheme via derivatives of the atomic point charges which would also reduce the cost of the AIFDEM derivatives.

Bibliography

[1] A. F. Morrison, Z.-Q. You, and J. M. Herbert, J. Chem. Theory Comput. **10**, 5366 (2014).

[2] B. Temelso, K. A. Archer, and G. C. Shields, J. Phys. Chem. A **115**, 12034 (2011).

[3] A. F. Morrison and J. M. Herbert, J. Phys. Chem. Lett. **8**, 1442 (2017).

[4] S. Zheng, H. Phillips, E. Geva, and B. D. Dunietz, J. Am. Chem. Soc. **134**, 6944 (2012).

[5] T. L. Bahers et al., J. Phys. Chem. Lett. **4**, 1044 (2013).

[6] I. Oprea, P. Panait, F. Cimpoesu, M. Ferbinteanu, and M. A. Girtu, Materials **6**, 2372 (2013).

[7] H. Shao et al., Angew. Chem. Int. Ed. Engl. **49**, 7688 (2010).

[8] M. Gao et al., J. Phys. Chem. C **119**, 13948 (2015).

[9] J. B. Foresman, M. Head-Gordon, J. A. Pople, and M. J. Frisch, J. Phys. Chem. **96**, 135 (1992).

[10] Y. Mochizuki et al., Chem. Phys. Lett. **406**, 283 (2005).

[11] H. Nakatsuji, T. Miyahara, and R. Fukuda, J. Chem. Phys. **126**, 084104:1 (2007).

[12] P. Elliott, F. Furche, and K. Burke, Excited states from time-dependent density functional theory, in *Reviews in Computational Chemistry*, volume 26, chapter 3, pages 91–165, Wiley-VCH, 2009.

[13] L. Bernasconi, M. Sprik, and J. Hutter, J. Chem. Phys. **119**, 12417 (2003).

[14] A. Dreuw and M. Head-Gordon, J. Am. Chem. Soc. **126**, 4007 (2004).

[15] J. Neugebauer, M. J. Louwerse, E. J. Baerends, and T. A. Wesołowski, J. Chem. Phys. **122**, 094115:1 (2005).

[16] R. J. Magyar and S. Tretiak, J. Chem. Theory Comput. **3**, 976 (2007).

[17] A. Lange and J. M. Herbert, J. Chem. Theory Comput. **3**, 1680 (2007).

[18] A. W. Lange and J. M. Herbert, J. Am. Chem. Soc. **131**, 3913 (2009).

[19] R. M. Richard and J. M. Herbert, J. Chem. Theory Comput. **7**, 1296 (2011).

[20] J. Frenkel, Phys. Rev. **37**, 17 (1931).

[21] A. S. Davydov, Soviet Physics Uspekhi **7**, 145 (1964).

[22] D. E. LaLonde, J. D. Petke, and G. M. Maggiora, J. Phys. Chem. **92**, 4746 (1988).

[23] D. Lee, L. Greenman, M. Sarovar, and K. B. Whaley, J. Phys. Chem. A **117**, 11072 (2013).

[24] B. P. Krueger, G. D. Scholes, and G. R. Fleming, J. Phys. Chem. B **102**, 5378 (1998).

[25] S. Tretiak, W. M. Zhang, V. Chernyak, and S. Mukamel, Proc. Natl. Acad. Sci. USA **96**, 13003 (1999).

[26] H. Zhang, J.-P. Malrieu, H. Ma, and J. Ma, J. Comput. Chem. **33**, 34 (2012).

[27] Y. Ma, Y. Liu, and H. Ma, J. Chem. Phys. **136**, 024113:1 (2012).

[28] A. V. Luzanov, A. A. Sukhorukov, and V. E. Umanskii, Theor. Exp. Chem. **10**, 354 (1974).

[29] R. L. Martin, J. Chem. Phys. **118**, 4775 (2003).

[30] I. Mayer, Chem. Phys. Lett. **437**, 284 (2007).

[31] S. Hirata and M. Head-Gordon, Chem. Phys. Lett. **314**, 291 (1999).

[32] A. T. Amos and G. G. Hall, Proc. R. Soc. Lond. **A263**, 483 (1961).

[33] H. F. King, R. E. Stanton, H. Kim, R. E. Wyatt, and R. G. Parr, J. Chem. Phys. **47**, 1936 (1967).

[34] Y. Shao et al., Mol. Phys. **113**, 184 (2015).

[35] A. I. Krylov and P. M. W. Gill, WIREs Comput. Mol. Sci. **3**, 317 (2013).

[36] C. G. Elles, I. A. Shkrob, R. A. Crowell, and S. E. Bradforth, J. Chem. Phys. **126**, 164503:1 (2007).

[37] E. J. Baerends, O. V. Gritsenko, and R. van Meer, Phys. Chem. Chem. Phys. **15**, 16408 (2013).

[38] W. Xie, L. Song, D. G. Truhlar, and J. Gao, J. Chem. Phys. **128**, 234108:1 (2008).

[39] J. M. Herbert, L. D. Jacobson, K. U. Lao, and M. A. Rohrdanz, Phys. Chem. Chem. Phys. **14**, 7679 (2012).

[40] Z. C. Holden, R. M. Richard, and J. M. Herbert, J. Chem. Phys. **139**, 244108:1 (2013), Erratum: *J. Chem. Phys.* **142**, 059901:1–2 (2015).

[41] T. Zeng, R. Hoffmann, and N. Ananth, J. Am. Chem. Soc. **136**, 5755 (2014).

[42] T. Siegrist et al., Adv. Mater. **19**, 2079 (2007).

[43] R. M. Richard, K. U. Lao, and J. M. Herbert, Acc. Chem. Res. **47**, 2828 (2014).

[44] E. J. Sundstrom and M. Head-Gordon, J. Chem. Phys. **140**, 114103:1 (2014).

[45] S. Hirata, Theor. Chem. Acc. **129**, 727 (2011).

[46] D. Maurice and M. Head-Gordon, Mol. Phys. **96**, 1533 (1999).

[47] R. Sedlak et al., J. Chem. Theory Comput. **9**, 3364 (2013).

[48] M. Valiev et al., Comput. Phys. Comm. **181**, 1477 (2010).

[49] M. Head-Gordon, R. J. Rico, M. Oumi, and T. J. Lee, Chem. Phys. Lett. **219**, 21 (1994).

[50] G. S. Engel et al., Nature **446**, 782 (2007).

[51] G. D. Scholes, G. R. Fleming, A. Olaya-Castro, and R. van Grondelle, Nat. Chem. **3**, 763 (2011).

[52] A. Chenu and G. D. Scholes, Annu. Rev. Phys. Chem. **66**, 69 (2015).

[53] C. Olbrich et al., J. Phys. Chem. B **115**, 8609 (2011).

[54] S. Jurinovich, C. Curutchet, and B. Mennucci, ChemPhysChem **15**, 3194 (2014).

[55] S. Shim, P. Rebentrost, S. Valleau, and A. Aspuru-Guzik, Biophys. J. **102**, 649 (2012).

[56] J. Huh et al., J. Am. Chem. Soc. **136**, 2048 (2014).

[57] A. Czader and E. R. Bittner, J. Chem. Phys. **128**, 035101:1 (2008).

[58] P. R. Surján, Chem. Phys. Lett. **439**, 393 (2007).

[59] M. B. Smith and J. Michl, Chem. Rev. **110**, 6891 (2010).

[60] P. M. Zimmerman, C. B. Musgrave, and M. Head-Gordon, Acc. Chem. Res. **46**, 1339 (2013).

[61] D. Casanova, J. Chem. Theory Comput. **10**, 324 (2014).

[62] B. Bouvier, T. Gustavsson, D. Markovitsi, and P. Millié, Chem. Phys. **275**, 75 (2002).

[63] B. Bouvier et al., J. Phys. Chem. B **107**, 13512 (2003).

[64] E. R. Bittner, J. Chem. Phys. **125**, 094909:1 (2006).

[65] E. R. Bittner, J. Photochem. Photobio. A **190**, 328 (2007).

[66] H. B. Schlegel and M. J. Frisch, Computational bottlenecks in molecular orbital calculations, in *Theoretical and Computational Models for Organic Chemistry*, edited by S. J. Formosinho, I. G. Csizmadia, and L. G. Arnaut, pages 5–33, Kluwer, 1991.

[67] A. G. Redfield, The theory of relaxation processes, in *Advances in Magnetic Resonance*, edited by J. S. Waugh, volume 1 of *Advances in Magnetic and Optical Resonance*, pages 1–32, Academic Press, 1965.

[68] H.-P. Breuer and F. Petruccione, *The Theory of Open Quantum Systems*, Oxford University Press, 2002.

[69] M. Schröter, *Dissipative Exciton Dynamics in Light Harvesting Complexes*, BestMasters, Springer Spektrum, 1 edition, 2015.

[70] L. Valkunas, D. Abramavicius, and T. Mančal, *Molecular Excitation Dynamics and Relaxation*, Wiley-VCH Verlag GmbH and Co. KGaA, Weinheim, Germany, 2013.

[71] C. Olbrich, J. Strümpfer, K. Schulten, and U. Kleinekathöfer, J. Phys. Chem. Lett. **2**, 1771 (2011).

[72] A. Ishizaki and G. R. Fleming, J. Chem. Phys. **130**, 234110:1 (2009).

[73] A. Kühl and W. Domcke, Chem. Phys. **259**, 227 (2000).

[74] W.-L. Chan et al., Acc. Chem. Res. **46**, 1321 (2013).

[75] P. Rebentrost, M. Mohseni, and A. Aspuru-Guzik, J. Phys. Chem. B **113**, 9942 (2009).

[76] J. R. Johansson, P. D. Nation, and F. Nori, Comput. Phys. Commun. **184**, 1234 (2013).

[77] S. R. Yost, T. Kowalczyk, and T. Van Voorhis, J. Chem. Phys. **139**, 174104:1 (2013).

[78] F. Bernardi, M. Olivucci, and M. A. Robb, Chem. Soc. Rev. **25**, 321 (1996).

[79] A. L. Sobolewski, W. Domcke, C. Dedonder-Lardeux, and C. Jouvet, Phys. Chem. Chem. Phys. **4**, 1093 (2002).

[80] B. G. Levine and T. J. Martínez, Annu. Rev. Phys. Chem. **58**, 613 (2007).

[81] W. Domcke and D. R. Yarkony, Annu. Rev. Phys. Chem. **63**, 325 (2012).

[82] S. Matsika and P. Krause, Annu. Rev. Phys. Chem. **62**, 621 (2011).

[83] J. Yang, L. Zhang, L. Wang, and D. Zhong, J. Am. Chem. Soc. **134**, 16460 (2012).

[84] G. A. Worth and L. S. Cederbaum, Annu. Rev. Phys. Chem. **55**, 127 (2004).

[85] B. E. Applegate, T. A. Barcholtz, and T. A. Miller, Chem. Soc. Rev. **32**, 38 (2003).

[86] V. Coropceanu et al., Chem. Rev. **107**, 926 (2007).

[87] Y. Shu, B. S. Fales, and B. G. Levine, Nano Lett. **15**, 6247 (2015).

[88] P. M. Zimmerman, F. Bell, D. Casanova, and M. Head-Gordon, J. Am. Chem. Soc. **133**, 19944 (2011).

[89] A. F. Morrison and J. M. Herbert, J. Phys. Chem. Lett. **6**, 4390 (2015).

[90] J. M. Herbert, X. Zhang, A. F. Morrison, and J. Liu, Acc. Chem. Res. **49**, 931 (2016).

[91] A. Sisto, D. R. Glowacki, and T. J. Martinez, Acc. Chem. Res. **47**, 2857 (2014).

[92] M. J. Bearpark, M. A. Robb, and H. B. Schlegel, Chem. Phys. Lett. **223**, 269 (1994).

[93] F. Sicilia, L. Blancafort, M. J. Bearpark, and M. A. Robb, J. Chem. Theory Comput. **4**, 257 (2008).

[94] X. Zhang and J. M. Herbert, J. Chem. Phys. **141**, 064104:1 (2014).

[95] J. A. Kammeraad and P. M. Zimmerman, J. Phys. Chem. Lett. **7**, 5074 (2016).

[96] P. Saxe, B. H. Lengsfield III, and D. R. Yarkony, Chem. Phys. Lett. **113**, 159 (1985).

[97] B. H. Lengsfield III and D. R. Yarkony, J. Chem. Phys. **84**, 348 (1986).

[98] B. H. Lengsfield III, P. Saxe, and D. R. Yarkony, J. Chem. Phys. **81**, 4549 (1984).

[99] H. Lischka, M. Dallos, P. G. Szalay, D. R. Yarkony, and R. Shepard, J. Chem. Phys. **120**, 7322 (2004).

[100] I. F. Galván, M. G. Delcey, T. B. Pedersen, F. Aquilante, and R. Lindh, J. Chem. Theory Comput. **12**, 3636 (2016).

[101] O. Christiansen, J. Chem. Phys. **110**, 711 (1999).

[102] A. Tajti and P. G. Szalay, J. Chem. Phys. **131**, 124104:1 (2009).

[103] S. Fatehi, E. Alguire, Y. Shao, and J. E. Subotnik, J. Chem. Phys. **135**, 234105:1 (2011).

[104] S. Fatehi and J. E. Subotnik, J. Phys. Chem. Lett. **3**, 2039 (2012).

[105] X. Zhang and J. M. Herbert, J. Chem. Phys. **142**, 064109:1 (2015).

[106] R. Send and F. Furche, J. Chem. Phys. **132**, 044107:1 (2010).

[107] Z. Li, B. Suo, and W. Liu, J. Chem. Phys. **141**, 244105:1 (2014).

[108] Q. Ou, G. D. Bellchambers, F. Furche, and J. E. Subotnik, J. Chem. Phys. **142**, 064114:1 (2015).

[109] F. Liu et al., Mol. Phys. **108**, 2791 (2010).

[110] X. Feng, A. V. Luzanov, and A. I. Krylov, J. Phys. Chem. Lett. **4**, 3845 (2013).

[111] A. V. Luzanov, A. A. Sukhorukov, and V. E. Umanskii, Theor. Exp. Chem. **10**, 354 (1974).

[112] A. J. W. Thom and M. Head-Gordon, J. Chem. Phys. **131**, 124113:1 (2009).

[113] K. Wright, Numer. Math. **63**, 283 (1992).

[114] T. Papadopoulo and M. I. A. Lourakis, Estimating the Jacobian of the singular value decomposition: Theory and applications, in *Proceedings of the 6th European Conference on Computer Vision—Part I*, edited by D. Vernon, ECCV '00, pages 554–570, Springer-Verlag, London, UK, 2000.

[115] J. A. Pople, R. Krishnan, H. B. Schlegel, and J. S. Binkley, Int. J. Quantum Chem. Symp. **13**, 225 (1979).

[116] N. C. Handy and H. F. Schaefer III, J. Chem. Phys. **81**, 5031 (1984).

[117] K. Hannewald and P. A. Bobbert, Appl. Phys. Lett. **85**, 1535 (2004).

[118] A. Troisi and G. Orlandi, Phys. Rev. Lett. **96**, 086601:1 (2006).

[119] A. Troisi, Adv. Mater. **19**, 2000 (2007).

[120] A. Girlando et al., Phys. Rev. B **82**, 035208:1 (2010).

[121] T. Kato and T. Yamabe, J. Chem. Phys. **115**, 8592 (2001).

[122] A. Troisi and G. Orlandi, J. Phys. Chem. A **110**, 4065 (2006).

[123] A. Painelli and A. Girlando, J. Chem. Phys. **84**, 5655 (1986).

[124] E. B. Wilson, J. C. Decius, and P. C. Cross, *Molecular Vibrations: The Theory of Infrared and Raman Vibrational Spectra*, McGraw-Hill, 1955.

[125] L. Grisanti et al., Phys. Rev. B **88**, 035450:1 (2013).

[126] P. Giannozzi et al., J. Phys: Condens. Matt. **21**, 395502:1 (2009).

[127] D. Holmes, S. Kumaraswamy, A. J. Matzger, and K. P. C. Vollhardt, Chem. Eur. J. **5**, 3399 (1999).

[128] D. Holmes, S. Kumaraswamy, A. J. Matzger, and K. P. C. Vollhardt, CCDC 114446: Experimental Crystal Structure Determination (1999), Deposited on: 8/2/1999.

[129] M. Abdulla, K. Refson, R. H. Friend, and P. D. Haynes, J. Phys.: Condens. Matt. **27**, 375402:1 (2015).

[130] J.-D. Chai and M. Head-Gordon, Phys. Chem. Chem. Phys. **10**, 6615 (2008).

[131] R. W. A. Havenith, H. D. de Gier, and R. Broer, Mol. Phys. **110**, 2445 (2012).

[132] T. C. Berkelbach, M. S. Hybertsen, and D. R. Reichman, J. Chem. Phys. **138**, 114103:1 (2013).

[133] A. J. Musser et al., Nat. Phys. **11**, 352 (2015).

[134] A. A. Bakulin et al., Nat. Chem. **8**, 16 (2016).

[135] M. B. Smith and J. Michl, Annu. Rev. Phys. Chem. **64**, 361 (2013).

[136] M. J. Y. Tayebjee, D. R. McCamey, and T. W. Schmidt, J. Phys. Chem. Lett. **6**, 2367 (2015).

[137] D. N. Congreve et al., Science **340**, 334 (2013).

[138] C. Jundt et al., Chem. Phys. Lett. **241**, 84 (1995).

[139] J. J. Burdett, A. M. Müller, D. Gosztola, and C. J. Bardeen, J. Chem. Phys. **133**, 144506:1 (2010).

[140] M. W. B. Wilson et al., J. Am. Chem. Soc. **135**, 16680 (2013).

[141] Z. Birech, M. Schoerer, T. Schmeiler, J. Pflaum, and H. Schwoerer, J. Chem. Phys. **140**, 114501:1 (2014).

[142] G. Vaubel and H. Baessler, Mol. Cryst. Liq. Cryst. **15**, 15 (1971).

[143] V. K. Thorsmølle et al., Phys. Rev. Lett. **102**, 017401:1 (2009).

[144] W.-L. Chan, M. Ligges, and X.-Y. Zhu, Nat. Chem. **4**, 840 (2012).

[145] G. B. Piland and C. J. Bardeen, J. Phys. Chem. Lett. **6**, 1841 (2015).

[146] A. Zhugayevych and S. Tretiak, Annu. Rev. Phys. Chem. **66**, 305 (2015).

[147] R. D. Pensack et al., J. Phys. Chem. Lett. **7**, 2370 (2016).

[148] M. J. Y. Tayebjee, R. G. C. R. Clady, and T. W. Schmidt, Phys. Chem. Chem. Phys. **15**, 14797 (2013).

[149] F. Mirjani, N. Renaud, N. Gorczak, and F. C. Grozema, J. Phys. Chem. C **118**, 14192 (2014).

[150] T. C. Berkelbach, M. S. Hybertsen, and D. R. Reichman, J. Chem. Phys. **141**, 074705:1 (2014).

[151] P. Elliott, S. Goldson, C. Canahui, and N. T. Maitra, Chem. Phys. **391**, 110 (2011).

[152] S. Matsika, X. Feng, A. V. Luzanov, and A. I. Krylov, J. Phys. Chem. A **118**, 11943 (2014).

[153] X. Feng and A. I. Krylov, Phys. Chem. Chem. Phys. **18**, 7751 (2016).

[154] N. J. Mayhall, J. Chem. Theory Comput. **12**, 4263 (2016).

[155] A. F. Morrison and J. M. Herbert, The Journal of Chemical Physics **146**, 224110 (2017).

[156] K. Hannewald et al., Phys. Rev. B **69**, 075211:1 (2004).

[157] H. Tamura, M. Huix-Rotllant, I. Burghardt, Y. Olivier, and D. Beljonne, Coherent vs. thermally activated singlet exciton fission in acene derivatives from

first principles quantum dynamics simulations: Molecular packing makes the difference, (arXiv:1504.05088), 2015.

APPENDIX A

Derivative of a singular value decomposition

This appendix provides the algorithm for taking the derivative of a SVD, adapted from Refs. 113 and 114. [A minor typographical error in Eq. (8) of Ref. 114 is also corrected here.] We use a superscript $[\gamma]$ to denote differentiation with respect to γ, but for simplicity other indices (*e.g.*, for monomer labels) are omitted here.

Consider a matrix function $\mathbf{A}(\gamma)$ with m rows and n columns, where m need not be equal to n. The SVD of this matrix is

$$\mathbf{A}(\gamma) = \mathbf{U}(\gamma)\,\mathbf{a}(\gamma)\,\mathbf{V}^{\dagger}(\gamma)\;, \tag{A.1}$$

where $\mathbf{a}(\gamma)$ is the $m \times n$ diagonal matrix of singular values, $\mathbf{U}(\gamma)$ is the $m \times m$ unitary matrix of left singular vectors, and $\mathbf{V}(\gamma)$ is the $n \times n$ unitary matrix of right singular vectors. We seek to compute derivatives of all three quantities with respect to the perturbation γ. In what follows, we suppress the explicit dependence on γ.

Differentiating Eq. (A.1) affords

$$\mathbf{A}^{[\gamma]} = \mathbf{U}^{[\gamma]}\mathbf{a}\mathbf{V}^{\dagger} + \mathbf{U}\mathbf{a}^{[\gamma]}\mathbf{V}^{\dagger} + \mathbf{U}\mathbf{a}\mathbf{V}^{[\gamma]\dagger}\;. \tag{A.2}$$

An essential detail of this algorithm is that $\mathbf{a}^{[\gamma]}$ must be diagonal, as the the matrix of singular values should remain diagonal for an infinitesimal perturbation. Differentiating the unitarity condition $\mathbf{1} = \mathbf{U}^\dagger\mathbf{U}$ affords

$$0 = \mathbf{U}^{[\gamma]\dagger}\mathbf{U} + \mathbf{U}^\dagger\mathbf{U}^{[\gamma]} = \mathbf{Z}^\dagger + \mathbf{Z} \tag{A.3}$$

where $\mathbf{Z} = \mathbf{U}^\dagger\mathbf{U}^{[\gamma]}$. Similarly, differentiation of the condition $\mathbf{1} = \mathbf{V}^\dagger\mathbf{V}$ affords

$$0 = \mathbf{V}^{[\gamma]\dagger}\mathbf{V} + \mathbf{V}^\dagger\mathbf{V}^{[\gamma]} = \mathbf{W}^\dagger + \mathbf{W} \tag{A.4}$$

where $\mathbf{W} = \mathbf{V}^\dagger\mathbf{V}^{[\gamma]}$. Multiplying Eq. (A.2) from the left by $\mathbf{U}^\dagger$ and from the right by $\mathbf{V}$ and rearranging affords

$$\begin{aligned} \mathbf{a}^{[\gamma]} &= \mathbf{U}^\dagger\mathbf{A}^{[\gamma]}\mathbf{V} - \mathbf{a}\mathbf{W}^\dagger - \mathbf{Z}\mathbf{a} \\ &= \mathbf{Q} - \mathbf{a}\mathbf{W}^\dagger - \mathbf{Z}\mathbf{a}, \end{aligned} \tag{A.5}$$

where $\mathbf{Q} = \mathbf{U}^\dagger\mathbf{A}^{[\gamma]}\mathbf{V}$. Note that both $\mathbf{Z}$ and $\mathbf{W}$ are skew-symmetric, hence the products $\mathbf{a}\mathbf{W}^\dagger$ and $\mathbf{Z}\mathbf{a}$ are zero along the diagonal and thus these two terms make no contribution to the singular value derivatives $\mathbf{a}^{[\gamma]}$, which are simply $a_{ii}^{[\gamma]} = Q_{ii}$.

To compute the derivatives of the singular vectors we must solve for the elements of $\mathbf{W}$ and $\mathbf{Z}$ that force $\mathbf{a}^{[\gamma]}$ to be diagonal as specified in Eq. (A.5), while enforcing skew-symmetry as specified in Eqs. (A.3) and (A.4). To that end, we solve $\binom{p}{2}$ systems of 2×2 equations, where $p = \min(m, n)$, each of which has the form

$$\begin{aligned} a_{kk}Z_{jk} + a_{jj}W_{kj} &= Q_{jk} \\ a_{jj}Z_{jk} + a_{kk}W_{kj} &= -Q_{kj} \ . \end{aligned} \tag{A.6}$$

Because $\mathbf{W}$ and $\mathbf{Z}$ are skew-symmetric, we need only solve for either the upper or the lower triangle of each, so in Eq. (A.6) we assume that $1 \leq j \leq \min(m, n)$ and

$j < k < \min(m, n)$. Singularities may arise in solving the linear systems in Eq. (A.6) when there are degeneracies amongst the singular values. The strategy in this case, as proposed in Ref. 114, is to gather sets of all 2×2 systems where $a_{jj} = a_{kk}$ and solve the systems of each set simultaneously using a least-squares approach. We use a degeneracy threshold $|a_{jj} - a_{kk}| \leq 10^{-10}$.

In the case that $m \neq n$ so that $\mathbf{A}$ is rectangular, there is an additional set of equations for elements of the larger matrix,

$$\begin{array}{ll} a_{kk} Z_{jk} = Q_{jk} & \text{if } m > n \\ a_{kk} W_{kj} = -Q_{kj} & \text{if } n > m \ . \end{array} \tag{A.7}$$

Here $1 \leq k \leq \min(m, n)$ and $\min(m, n) \leq j \leq \max(m, n)$. Equation (A.7) introduces another source of potential singularities when some a_{kk} approach zero. In our implementation , if $|a_{kk}| \leq 10^{-10}$ we simply set the corresponding elements of $\mathbf{W}$ or $\mathbf{Z}$ to zero. Although not technically correct, note that we only require SVD derivatives of a rectangular matrix when computing the derivative of the NTO transformation, in which case terms associated with small singular values are neglected anyway, so this is not an issue for our use of the SVD derivative. This may not be true in general, however. In the rectangular case, if $m > n$ (or conversely $n > m$), then the triangle of Z_{jk} (or W_{kj}), where $\min(m, n) + 1 \leq j \leq \max(m, n)$ and $\min(m, n) + 1 \leq k \leq j - 1$, remains undefined, but we are free to set these elements equal to zero.[113]

Since we solve Eqs. (A.6) and (A.7) only for the upper triangle of $\mathbf{Z}$ and the lower triangle of $\mathbf{W}$, the final forms of $\mathbf{W}$ and $\mathbf{Z}$ are obtained from the solutions of these equations by subtracting the transpose of the solution, resulting in skew-symmetric

matrices. Finally, derivatives of the singular vectors are given by

$$\begin{aligned} \mathbf{V}^{[\gamma]} &= \mathbf{V}\mathbf{W} \\ \mathbf{U}^{[\gamma]} &= \mathbf{U}\mathbf{Z} \, . \end{aligned} \tag{A.8}$$

APPENDIX B

Supplementary Material for "Evidence for Singlet Fission Driven by Vibronic Coherence in Crystalline Tetracene"

B.1 Plane-Wave DFT Calculations

The unit cell for crystalline tetracene[127,128] was retrieved from the Cambridge Crystallographic Database and used as a starting point for geometry optimization via plane-wave DFT. As noted by Abdulla *et al.*,[129] lack of support for dispersion-corrected functionals for phonon calculations presents a major obstacle for studies of conjugated organic systems where these interactions play a key role. A crude yet serviceable workaround is to forgo the use of a generalized gradient approximation in favor of the local density approximation (LDA), as the latter has a tendency to overestimate binding energies, thus compensating for the absence of attractive dispersion interactions. All plane-wave DFT calculations were performed using the LDA functional and norm-conserving pseudopotentials.

Plane-wave DFT calculations were performed using the Quantum Espresso package.[126] Variable unit cell optimization was performed on the initial crystal structure under 1 atm of pressure with the SCF converged to a threshold of 10^{-9} a.u., mixing parameter $\beta = 0.7$, and kinetic energy cutoff of 60 Rydberg for the plane-wave

basis. The Brillouin zone was sampled using a $2 \times 2 \times 1$ k-point mesh, and phonon modes were then computed for this optimized structure at the Γ point. The resulting phonon modes are in good agreement with previous work.[129] The asymmetric dimer in Fig. B.1 constitutes the unit cell, and clearly shows the herringbone structure. Coordinates for this dimer are provided in Table B.1 and phonon mode frequencies are listed in Tables B.2-B.4.

B.2 Exciton Model Calculations

AIFDEM calculations were performed on the dimer in Fig. B.1, using a locally-modified version of Q-Chem.[34] The exciton-site basis was constructed from monomer wave functions computed at the Hartree-Fock and configuration-interaction singles (CIS) levels, using the 6-31+G* basis set. In determinantal form, the triplet-pair basis states in Eq. (5) take the form

$$\begin{aligned}\left|{}^1\left(\Psi_A^{\mathrm{T}}\Psi_B^{\mathrm{T}}\right)\Psi_C\cdots\right\rangle = \sum_{i,a\in A}\sum_{j,b\in B} t^{ia}t^{jb}\Bigg(&\frac{1}{\sqrt{3}}|\Phi_A^{\bar{i}a}\Phi_B^{j\bar{b}}\Phi_C\cdots\rangle + \frac{1}{\sqrt{3}}|\Phi_A^{i\bar{a}}\Phi_B^{\bar{j}b}\Phi_C\cdots\rangle \\ &- \frac{1}{\sqrt{6}}|\Phi_A^{ia}\Phi_B^{jb}\Phi_C\cdots\rangle + \frac{1}{\sqrt{6}}|\Phi_A^{ia}\Phi_B^{\bar{j}\bar{b}}\Phi_C\cdots\rangle + \frac{1}{\sqrt{6}}|\Phi_A^{\bar{i}\bar{a}}\Phi_B^{jb}\Phi_C\cdots\rangle \\ &- \frac{1}{\sqrt{6}}|\Phi_A^{\bar{i}\bar{a}}\Phi_B^{\bar{j}\bar{b}}\Phi_C\cdots\rangle\Bigg)\end{aligned} \tag{B.1}$$

where overbars denote orbitals with β spin, and the singly-excited monomer amplitudes t^{ia} from Eq. (6) are spin-restricted. Matrix elements between non-orthgonal determinants such as $|\Phi_A^{\bar{i}a}\Phi_B^{j\bar{b}}\Phi_C\cdots\rangle$ are computed as in our previous work.[1]

AIFDEM calculations were performed using both a 25% and a 50% truncation threshold for the transformation between canonical molecular orbitals and natural

transition orbitals (NTOs), or in other words insisting that we recover either 25% or 50% of the norm of the total transition vector, in the NTO basis. Eigenstates of the exciton Hamiltonian using either threshold are provided in Table B.5 and are qualitatively similar when comparing the two thresholds. Non-adiabatic couplings $H^{[x]}_{JK}$, where J is the S_1 state, K is the multi-exciton state, and x is a nuclear Cartesian coordinate, are listed in Table B.6 for a 25% NTO truncation threshold, and in Table B.7 for a 50% truncation threshold. Projecting the plane-wave DFT phonon modes onto these couplings reveals which mode significantly modulate the derivative couplings, and this information is provided in Tables B.2-B.4 for both values of the NTO truncation threshold. Specifically, we list what percentage of the norm of the total nonadiabatic coupling vector is recovered by each phonon mode. This analysis clearly demonstrates that only a few modes are responsible for the overwhelming majority of the coupling.

B.3 Vibronic model Hamiltonian

For our vibronic simulations we utilize the well known Holstien-Peierls model.[86,117–120,146] The Hamiltonian is

$$\begin{aligned}\hat{\mathcal{H}} = \sum_A |A\rangle \left[E_A + \sum_\alpha \omega_\alpha \left(\hat{a}^\dagger_\alpha \hat{a}_\alpha + \frac{1}{2} \right) + \frac{g_{AA\alpha}}{\sqrt{2}} \left(\hat{a}^\dagger_\alpha + \hat{a}_\alpha \right) \right] \langle A| \\ + \sum_A \sum_{B \neq A} |A\rangle \left(V_{AB} + \sum_\alpha \frac{g_{AB\alpha}}{\sqrt{2}} \left(\hat{a}^\dagger_\alpha + \hat{a}_\alpha \right) \right) \langle B|\end{aligned} \tag{B.2}$$

in atomic units. Indices A and B refer to diabatic electronic states that in our model correspond to the exciton-site basis states of the AIFDEM. We include the states $|\Psi_A \Psi_B\rangle$, $|\Psi^*_A \Psi_B\rangle$, $|\Psi_A \Psi^*_B\rangle$, and $|^1(\mathrm{TT})\rangle$, and the electronic AIFDEM Hamiltonian

is initially subjected to symmetric (Löwdin) orthogonalization. The operators $\hat{a}_\alpha$ and $\hat{a}_\alpha^\dagger$ are harmonic oscillator raising and lowering operators for phonon mode α, whose frequency is ω_α. Our simulations, however, are limited to a single mode with $\omega = 1432.19$ cm^{-1}, as computed via plane-wave DFT, and only the $|0\rangle$ and $|1\rangle$ states of the oscillator are included in the basis.

Diagonal entries E_A represent the exciton-site energies. The AIFDEM lacks intramolecular dynamical electron correlation and therefore does not reproduce the known singlet/triplet gap in tetracene, so for the purpose of the Redfield dynamics simulations the computed site energies were corrected to match experimental values of the $S_0 \rightarrow S_1$ excitation energy and the S_0/T_1 gap. (Similar corrections have been used in RAS-2SF calculations,[60,110] for the same reason: these calculations are capable of describing the coupled triplet pair but also lack dynamical electron correlation. This amounts to shifting E_A downwards by 12,251.6 cm^{-1} for single-exciton eigenstates and downward by 11,533.7 cm^{-1} for the multi-exciton eigenstate. The electronic coupling elements V_{AB} in Eq. (B.2) were taken directly from the orthogonalized AIFDEM Hamiltonian.

The quantities $g_{AA\alpha}$ and $g_{AB\alpha}$ are electron-phonon coupling constants of the local (Holstein) and non-local (Peierls) type, respectively. To compute these couplings we first symmetrically orthogonalize the AIFDEM derivatives couplings, including the derivative of the orthogonalization transformation. (Details of how to take the derivative of Löwdin's symmetric orthogonalization transformation can be found in Ref. 155.) The orthogonalized derivatives are then transformed from atomic Cartesian

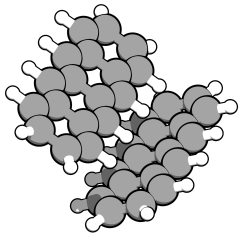

Figure B.1: Tetracene dimer extracted from the optimized crystal structure and used for subsequent AIFDEM calculations.

coordinates, in which they are initially computed, to the dimensionless spectroscopic coordinates corresponding to normal modes:

$$g_{AB\alpha} = \frac{1}{\sqrt{\mu_\alpha \omega_\alpha}} \sum_x H_{AB}^{[x]} D_{x\alpha} \ . \tag{B.3}$$

Here, the αth column of the matrix $\mathbf{D}$ contains the normalized Cartesian displacements corresponding to normal mode α, and μ_α is its effective mass. Following this transformation, the electron/phonon couplings, which are in practice matrix elements of the vibronic Hamiltonian, have appropriate dimensions of energy.

Redfield dynamics simulations for the model Hamiltonian in the indicated basis were performed using the QuTip program.[76]

Table B.1: Optimized geometry of the crystalline tetracene unit cell (dimer).

atom	x	y	z	atom	x	y	z
C	1.10179	4.81008	-4.73772	C	-2.32282	1.63662	-4.50776
C	0.15871	4.26741	-3.92745	C	-3.21899	1.65149	-3.49145
C	0.37922	4.14461	-2.53904	C	-2.93377	1.00115	-2.27384
C	-0.55307	3.57764	-1.69601	C	-3.83808	0.97847	-1.23419
C	-0.32233	3.46244	-0.32808	C	-3.56010	0.31552	-0.04378
C	-1.25933	2.89562	0.53050	C	-4.47188	0.27949	1.00699
C	-1.02206	2.78519	1.88432	C	-4.18288	-0.36890	2.18822
C	-1.96559	2.20709	2.75809	C	-5.08664	-0.38053	3.27138
C	-1.71759	2.11526	4.08758	C	-4.76639	-1.00289	4.43120
C	-0.50647	2.59193	4.62443	C	-3.53195	-1.66582	4.56887
C	0.43661	3.13460	3.81416	C	-2.63577	-1.68069	3.55255
C	0.21610	3.25740	2.42575	C	-2.92100	-1.03035	2.33495
C	1.14839	3.82437	1.58271	C	-2.01669	-1.00768	1.29529
C	0.91765	3.93957	0.21479	C	-2.29467	-0.34473	0.10488
C	1.85465	4.50639	-0.64380	C	-1.38288	-0.30870	-0.94588
C	1.61738	4.61682	-1.99761	C	-1.67189	0.33969	-2.12711
C	2.56091	5.19492	-2.87139	C	-0.76813	0.35133	-3.21028
C	2.31290	5.28675	-4.20088	C	-1.08837	0.97368	-4.37010
H	0.91521	4.88574	-5.81056	H	-2.56426	2.13780	-5.44540
H	-0.79274	3.91225	-4.32767	H	-4.17920	2.15937	-3.60059
H	-1.49473	3.20942	-2.10806	H	-4.79819	1.48656	-1.34815
H	-2.20424	2.53117	0.12120	H	-5.43284	0.78721	0.89474
H	-2.90117	1.83838	2.33679	H	-6.04433	0.13001	3.15570
H	-2.46090	1.66217	4.74486	H	-5.46728	-0.98841	5.26790
H	-0.31989	2.51626	5.69727	H	-3.29051	-2.16700	5.50650
H	1.38805	3.48975	4.21437	H	-1.67557	-2.18857	3.66169
H	2.09005	4.19259	1.99477	H	-1.05658	-1.51576	1.40925
H	2.79955	4.87083	-0.23449	H	-0.42193	-0.81641	-0.83364
H	3.49649	5.56363	-2.45008	H	0.18956	-0.15922	-3.09460
H	3.05622	5.73984	-4.85815	H	-0.38749	0.95921	-5.20680

Table B.2: Normal mode frequencies (in cm^{-1}) and percentage of the nonadiabatic coupling projection (1/3).

Mode	Freq.	% of coupling		Mode	Freq.	% of coupling	
		25% NTO[a]	50% NTO[b]			25% NTO[a]	50% NTO[b]
1	53.67	0.04	0.03	30	471.72	0.00	0.00
2	69.86	0.18	0.19	31	479.01	0.00	0.00
3	80.96	0.00	0.00	32	483.96	0.02	0.00
4	101.51	0.00	0.00	33	487.53	0.00	0.00
5	103.99	0.11	0.04	34	493.45	0.02	0.00
6	119.02	0.01	0.00	35	497.16	0.03	0.10
7	136.31	0.03	0.00	36	499.11	0.00	0.00
8	147.96	0.01	0.00	37	508.13	0.00	0.00
9	152.79	0.02	0.01	38	515.38	0.00	0.00
10	161.08	0.00	0.01	39	554.09	0.05	0.02
11	169.92	0.01	0.00	40	557.80	0.02	0.01
12	172.20	0.00	0.00	41	568.27	0.00	0.00
13	180.74	0.01	0.02	42	573.03	0.00	0.00
14	182.36	0.01	0.01	43	611.93	0.01	0.09
15	223.31	0.00	0.00	44	614.57	0.01	0.05
16	228.64	0.00	0.00	45	621.34	0.07	0.10
17	274.45	0.00	0.00	46	622.36	0.03	0.02
18	282.42	0.00	0.00	47	628.21	0.02	0.03
19	303.44	0.22	0.08	48	628.29	0.05	0.04
20	304.28	0.01	0.00	49	730.59	0.00	0.00
21	318.67	0.02	0.05	50	731.17	0.00	0.00
22	325.17	0.00	0.01	51	732.66	0.00	0.00
23	329.97	0.00	0.00	52	735.60	0.00	0.00
24	332.51	0.01	0.00	53	739.80	0.01	0.00
25	392.72	0.00	0.00	54	750.26	0.02	0.00
26	397.54	0.00	0.00	55	759.94	0.34	0.30
27	436.65	0.12	0.05	56	760.86	0.05	0.01
28	438.20	0.09	0.03	57	762.27	0.24	0.03
29	460.44	0.01	0.00	58	762.56	0.47	0.10

[a]Retaining 25% of the total norm of the NTOs
[a]Retaining 50% of the total norm of the NTOs

Table B.3: Normal mode frequencies (in cm^{-1}) and percentage of the nonadiabatic coupling projection (2/3).

Mode	Freq.	% of coupling		Mode	Freq.	% of coupling	
		25% NTO[a]	50% NTO[b]			25% NTO[a]	50% NTO[b]
59	770.25	0.00	0.00	88	981.78	0.00	0.00
60	774.71	0.05	0.03	89	983.88	0.01	0.00
61	780.99	0.00	0.02	90	988.49	0.00	0.00
62	782.65	0.01	0.01	91	1013.49	0.11	0.07
63	782.82	0.01	0.01	92	1014.92	0.99	0.97
64	788.38	0.00	0.00	93	1016.20	0.00	0.00
65	835.06	0.00	0.00	94	1016.73	0.62	0.70
66	839.11	0.01	0.00	95	1116.40	0.01	0.01
67	840.38	0.00	0.00	96	1117.82	0.04	0.05
68	852.78	0.23	0.24	97	1121.46	0.02	0.00
69	854.71	0.01	0.00	98	1123.62	0.00	0.00
70	855.49	2.11	1.97	99	1127.33	0.11	0.00
71	868.41	0.38	0.42	100	1136.49	0.02	0.00
72	871.27	0.01	0.00	101	1137.04	0.22	0.14
73	891.62	0.00	0.00	102	1146.23	0.11	0.17
74	891.90	0.00	0.00	103	1152.19	0.44	0.01
75	895.25	0.00	0.01	104	1153.55	0.06	0.01
76	896.24	0.02	0.07	105	1163.50	0.23	0.01
77	910.60	0.02	0.00	106	1165.26	0.01	0.01
78	913.30	0.01	0.00	107	1198.39	0.27	0.28
79	921.93	0.00	0.00	108	1200.36	0.04	0.04
80	926.82	0.00	0.00	109	1201.83	7.03	6.78
81	928.55	0.00	0.00	110	1202.83	0.24	0.55
82	929.30	0.24	0.11	111	1255.88	0.13	0.10
83	959.49	0.00	0.00	112	1257.09	0.00	0.00
84	962.49	0.00	0.00	113	1257.94	0.00	0.00
85	962.91	0.01	0.00	114	1258.62	0.03	0.02
86	964.97	0.00	0.01	115	1299.38	0.10	0.14
87	975.04	0.01	0.00	116	1303.03	0.01	0.00

[a]Retaining 25% of the total norm of the NTOs
[a]Retaining 50% of the total norm of the NTOs

Table B.4: Normal mode frequencies (in cm^{-1}) and percentage of the nonadiabatic coupling projection (3/3).

Mode	Freq.	% of coupling		Mode	Freq.	% of coupling	
		25% NTO[a]	50% NTO[b]			25% NTO[a]	50% NTO[b]
117	1306.73	0.35	0.71	146	1633.73	0.20	0.01
118	1307.81	0.05	0.01	147	1634.41	3.17	0.15
119	1326.01	0.24	0.28	148	1638.34	0.03	0.00
120	1331.41	0.00	0.00	149	1651.22	0.58	0.67
121	1376.44	0.00	0.00	150	1654.52	0.00	0.02
122	1381.08	0.02	0.01	151	3045.06	0.00	0.00
123	1399.32	1.74	0.04	152	3048.49	0.00	0.00
124	1404.17	0.32	0.00	153	3048.91	0.00	0.00
125	1412.63	0.01	0.00	154	3049.05	0.00	0.00
126	1413.25	0.47	0.76	155	3049.36	0.00	0.00
127	1432.19	26.90	27.26	156	3049.65	0.00	0.00
128	1434.08	11.55	14.12	157	3051.26	0.00	0.00
129	1439.99	0.37	0.09	158	3052.40	0.00	0.00
130	1440.63	0.14	0.00	159	3053.13	0.04	0.05
131	1451.91	0.07	0.02	160	3054.34	0.07	0.11
132	1454.72	0.50	0.36	161	3056.79	0.00	0.00
133	1459.51	0.62	0.47	162	3057.27	0.02	0.01
134	1463.87	0.03	0.02	163	3057.65	0.05	0.06
135	1475.26	0.37	0.24	164	3057.90	0.01	0.00
136	1477.13	0.00	0.00	165	3059.50	0.00	0.01
137	1536.86	19.36	19.05	166	3060.04	0.01	0.01
138	1539.89	13.17	18.13	167	3062.67	0.00	0.00
139	1559.22	1.50	0.53	168	3063.27	0.07	0.10
140	1564.22	0.00	0.33	169	3064.60	0.03	0.04
141	1564.94	0.11	0.58	170	3064.67	0.00	0.00
142	1567.89	0.16	0.01	171	3074.15	0.09	0.12
143	1580.55	0.20	0.26	172	3075.62	0.04	0.01
144	1583.70	0.00	0.00	173	3075.74	0.19	0.17
145	1628.80	0.00	0.00	174	3075.99	0.04	0.06

[a]Retaining 25% of the total norm of the NTOs
[a]Retaining 50% of the total norm of the NTOs

Table B.5: Eigenvectors for tetracene dimer in the non-orthogonal exciton-site basis.

25 % NTO Threshold

Eigenstate	$\|\Xi_{S_0}\rangle$	$\|\Xi_{S_1}\rangle$	$\|\Xi_{S_2}\rangle$	$\|\Xi_{TT}\rangle$
Excitation Energy (eV)		2.30	2.37	2.53
Oscillator Strength		0.1932	0.3776	0.0
Basis State	Eigenvector Coefficient			
$\|\Psi_A\Psi_B\rangle$	0.9967	-0.0642	0.0502	-0.0010
$\|\Psi_A^*\Psi_B\rangle$	-0.0502	-1.0173	-0.2605	-0.0031
$\|\Psi_A\Psi_B^*\rangle$	0.0686	0.2574	-1.0174	0.0054
$\|^1(\mathrm{TT})\rangle$	-0.0005	0.0050	-0.0052	-1.2193

50 % NTO Threshold

Eigenstate	$\|\Xi_{S_0}\rangle$	$\|\Xi_{S_1}\rangle$	$\|\Xi_{S_2}\rangle$	$\|\Xi_{TT}\rangle$
Excitation Energy (eV)		2.30	2.36	2.50
Oscillator Strength		0.1142	0.2078	0.0
Basis State	Eigenvector Coefficient			
$\|\Psi_A\Psi_B\rangle$	0.9982	0.0476	0.0353	0.0020
$\|\Psi_A^*\Psi_B\rangle$	0.0375	-0.9942	0.2271	-0.0087
$\|\Psi_A\Psi_B^*\rangle$	0.0466	-0.2254	-0.9942	-0.0111
$\|^1(\mathrm{TT})\rangle$	-0.0010	-0.0118	-0.0097	1.1139

Table B.6: Nonadiabatic coupling vector (in a.u.) using a 25% NTO truncation threshold.

atom	x	y	z	atom	x	y	z
C	0.02100	-0.02757	0.16775	C	0.10358	-0.12173	0.16509
C	0.19179	0.02927	0.25526	C	0.21218	-0.18228	0.21657
C	0.63195	0.43264	-0.58823	C	0.70768	-0.00708	-0.80211
C	-0.30519	-0.28779	0.63657	C	-0.31353	-0.17184	0.76639
C	-0.65980	-0.19976	-0.33843	C	-0.69541	0.32954	-0.05098
C	0.10671	0.07588	-0.81563	C	0.12703	0.33594	-0.90593
C	0.07336	-0.19846	0.95791	C	0.19196	-0.55775	1.06989
C	0.29797	0.13192	-0.09437	C	0.35392	-0.00980	-0.34702
C	0.04476	0.04864	-0.02294	C	0.28100	-0.16420	0.00457
C	0.02224	0.04370	-0.24636	C	-0.31568	0.16945	-0.01639
C	-0.20167	-0.07872	-0.11337	C	-0.07993	0.27753	-0.39313
C	-0.43380	-0.28906	0.40450	C	-0.74163	-0.05135	0.88778
C	0.28024	0.14057	-0.35481	C	0.35884	0.20459	-0.77654
C	0.76584	0.41155	-0.01680	C	0.69785	-0.32606	0.02170
C	-0.22952	-0.27373	0.98433	C	-0.12755	-0.27780	0.94861
C	-0.41658	0.21476	-2.59315	C	-0.20841	0.55950	-1.02480
C	-0.75712	-0.31287	0.37801	C	-0.33608	0.07240	0.25286
C	-0.53065	-0.33027	0.11229	C	-0.16893	0.05827	0.05588
H	-0.00419	0.01253	-0.00350	H	-0.00112	-0.00055	-0.00299
H	-0.01074	0.01374	-0.00637	H	-0.00535	0.00321	-0.00188
H	-0.00188	0.01332	0.01203	H	0.00756	-0.00619	0.00852
H	0.00298	0.02763	0.00027	H	0.01159	-0.00289	-0.00879
H	-0.01020	0.00554	-0.00067	H	-0.00655	0.00294	-0.00004
H	-0.00087	-0.00167	0.00080	H	0.00003	-0.00368	0.00242
H	0.00105	0.00030	0.00224	H	-0.00076	0.00091	0.00166
H	0.00289	0.00326	0.00126	H	0.00173	-0.01043	-0.00082
H	-0.01098	-0.00072	-0.00952	H	-0.00729	0.00652	-0.01022
H	-0.01066	-0.01148	0.00676	H	-0.01268	0.00138	0.00704
H	0.00595	0.00183	0.00002	H	0.00457	-0.00490	-0.00071
H	-0.00056	0.00427	-0.00009	H	-0.00086	-0.00265	-0.00374

Table B.7: Nonadiabatic coupling vector (in a.u.) using a 50% NTO truncation threshold.

atom	x	y	z	atom	x	y	z
C	-0.05021	-0.04935	0.33738	C	0.38397	-0.28726	0.22479
C	0.39801	0.07917	0.44352	C	0.38960	-0.48138	0.68293
C	1.05287	0.62966	-1.19994	C	1.65765	0.04404	-1.96014
C	-0.69303	-0.48531	1.21856	C	-0.79431	-0.38381	1.77480
C	-1.54914	-0.67702	-0.47284	C	-1.50209	0.73688	-0.04662
C	0.28439	0.46513	-1.48900	C	0.27696	0.75338	-2.05299
C	0.25500	-0.10719	1.73058	C	0.57992	-1.26406	2.33771
C	0.55708	0.25833	0.14393	C	0.74531	-0.11258	-0.56860
C	0.12765	0.09940	-0.53122	C	0.45491	-0.16054	-0.13805
C	0.19279	0.11848	-0.32741	C	-0.29004	0.26746	-0.28325
C	-0.48896	-0.12220	-0.44789	C	-0.47029	0.44558	-0.65419
C	-1.27871	-0.78895	1.32314	C	-1.76092	-0.06212	2.01749
C	0.68319	0.61150	-1.60061	C	0.80328	0.40872	-1.90918
C	1.38079	0.41090	1.01228	C	1.44112	-0.78644	0.23178
C	-0.09172	-0.23086	1.22630	C	-0.21110	-0.73296	1.89340
C	-0.56903	0.44765	-4.36804	C	-0.50720	1.23894	-2.26993
C	-0.98815	-0.52283	-0.07502	C	-0.73674	0.09488	0.54980
C	-0.91672	-0.42402	0.44792	C	-0.46780	0.18458	0.09895
H	-0.00404	-0.00220	-0.01628	H	0.00195	0.00284	-0.00595
H	-0.00672	-0.00870	-0.00631	H	-0.01340	0.00697	-0.00344
H	0.01320	0.01089	0.02804	H	0.01681	-0.01434	0.02143
H	0.01950	0.02166	-0.00622	H	0.02416	-0.00671	-0.01913
H	-0.01282	0.00045	0.00405	H	-0.01446	0.00776	0.00120
H	-0.00829	-0.00305	-0.00040	H	-0.00425	-0.00449	0.00439
H	0.00557	0.00375	0.00518	H	-0.00211	-0.00262	0.00739
H	0.00769	0.00663	0.01416	H	0.01866	-0.00038	0.00899
H	-0.00894	-0.00133	-0.02564	H	-0.01301	0.01626	-0.01989
H	-0.02486	-0.00636	0.00495	H	-0.02313	0.00751	0.01769
H	0.01148	0.00618	0.00012	H	0.01507	-0.00829	-0.00145
H	0.00831	-0.00174	-0.00114	H	0.00260	0.00239	-0.00511